Computational Methods for Coupled Fast and Thermal Spectrum Reactor Core Analysis

by

Puran Deng

A dissertation submitted in partial fulfillment
of the requirements for the degree of
Doctor of Philosophy
(Nuclear Engineering and Radiological Sciences)
in The University of Michigan
2022

Doctoral Committee:

Professor Won Sik Yang, Chair
Professor Thomas J. Downar
Dr. Taek K. Kim, Argonne National Laboratory
Professor Lumin Wang

Puran Deng

puran@umich.edu

ORCID iD: 0000-0003-3625-1541

© Puran Deng 2022

To all the days I lived
that make me who I am today and prepare for whom I will become

Acknowledgements

I would like to express my sincere gratitude to Prof. Won Sik Yang for his kindness, patience, encourage, and wise mentoring and helpful advice he has provided throughout my graduate study. Prof. Yang has been a respectful advisor who really enjoys teaching and shows the correct way of thinking. I would also like to thank Prof. Thomas Downar, Prof. Lumin Wang, and Dr. Taek K. Kim for serving on my thesis committee.

I would like to extend my gratitude to my colleague and friends, Dr. Tian Jing, Dr. Ching-Sheng Lin, Mr. Albert Hsieh, Mr. Gang Yang, Dr. Mustafa Jaradat, Dr. Byoung-kyu Jeon, and Dr. Hansol Park, for the insightful discussions, code sharing, inspiring questions and suggestions happened between us through these years, and their kind help in my daily life. Especially Tian and Ching-Sheng, they are like my elder sister and brother keeping me away from isolation and depression when I was struggling with study and research in the first a few years of this journey.

Finally, special thanks go to my wife Nana, my daughter Luna, and my parents for their endless love and support during my oversea study. I would not be able to succeed without their continuous encourage and trust in me.

Table of Contents

List of Figures

List of Tables

List of Appendices

Abstract

Most nuclear reactors are designed to be operated under either thermal or fast neutron spectrum, depending on the energy range of dominant neutrons that sustain the fission chain reaction. Almost all the commercial power reactors are thermal reactors while many Generation-IV reactor designs are fast spectrum based. In addition to fast and thermal spectrum reactors, coupled fast-thermal spectrum reactor (CFTR) concepts, which have both fast and thermal spectrum regions, have been adopted in several research reactors, including the initial design of the Versatile Test Reactor (VTR). For the analysis and assessment of reactor core designs, numerous computational methods have been developed and implemented into legacy codes. These legacy methods and codes adopted different simplifications and approximations in nuclear data representation, multigroup cross section (XS) generation, and whole core transport and fuel cycle analyses, tailored for specific reactor types. Hence, their applicability to other reactor types is limited. Except for Monte Carlo (MC) methods, there is no existing core analysis method directly applicable to CFTRs. This dissertation work is intended to develop an efficient two-step method in replacement of full-core MC simulations for CFTR core design and analysis.

Since a CFTR would exhibit combined neutronic characteristics of both fast and thermal reactors, among the legacy two-step methods, the fast reactor core calculation method is preferred in that the whole-core depletion calculation capability with transport flux solution is readily available. To be applied to CFTRs, several improvements were made in the current fast reactor analysis methods based on the MC^2-3, VARIANT, and REBUS-3 codes of Argonne National Laboratory. A new computational procedure was developed by combining MC simulation and

MC^2-3 for multigroup XS generation, incorporating partial current discontinuity factor (PCDF) into VARIANT for nodal transport analysis, and enabling the use of burnup dependent XSs and PCDFs in REBUS-3 depletion calculation.

The new XS generation scheme was developed primarily based on MC simulations in assembly supercell models while MC^2-3 is used to produce consistently weighted anisotropic scattering cross sections. Supercell models are used because of the significant spectral interference in CFTR environments. The long-range environmental effects are considered by imposing approximate source boundary conditions or including background source zones in the supercell model. Thorough verification tests were performed using two CFTR problems.

To reduce assembly homogenization errors in VARIANT nodal transport calculations, PCDF was derived in a consistent formulation for arbitrary angular approximation orders and is fully compatible with the efficient red-black iteration scheme of VARIANT. Practical approaches were developed to generate PCDFs using the reference nodal average flux and surface averaged partial currents obtained from MC simulation. For practical applications, fixed source calculation and imbedded PCDF correction strategies were developed to treat long-range environmental effects on the PCDFs generated from supercell models.

Enhancements of REBUS-3 were made in the depletion chain construction and utilization of burnup dependent XSs and energy dependent fission yields in a general manner. The modified REBUS-3 with these improvements and the improved VARIANT nodal transport method was verified using a 2D CFTR whole-core depletion problem. Compared to the original REBUS-3 depletion with constant isotopic XSs and VARIANT transport calculation without PCDFs, the new two-step method reduced the k-effective error by ~1000 pcm. It also predicted fuel assembly powers accurately within a 1% deviation from the reference MC depletion results.

Chapter 1

Introduction

Most nuclear reactors are designed to be operated under either thermal or fast neutron spectrum, depending on the energy range of dominant neutrons that sustain the fission chain reaction. Almost all the commercial power reactors are thermal reactors while many Generation-IV reactor designs, e.g., Gas-cooled Fast Reactor, Lead-cooled Fast Reactor, Sodium-cooled Fast Reactor, are fast spectrum based. In addition to fast and thermal spectrum reactors, the coupled fast-thermal spectrum reactor (CFTR) concept, which has both fast and thermal spectrum regions in the reactor core, has been adopted in several research reactors. For the analysis and assessment of reactor core designs, numerous computational modeling and simulation methods have been developed and implemented into legacy computer codes. These legacy methods and codes usually adopt different simplifications and approximations in nuclear data representation, multigroup cross section generation, whole core transport and fuel cycle analyses, tailored for specific reactor types. Hence, their applicability to other reactor types is limited. There is no existing core analysis method dedicated to coupled fast-thermal spectrum reactors. This dissertation work is intended to develop an efficient computational method in replacement of full-core Monte Carlo simulations for coupled-spectrum reactor core design and analysis.

1.1 Background

The idea of coupling a fast reactor with a locally moderated thermal zone was first proposed by Robert Avery [1] to obtain a combined system having the breeding ratio characteristic of a fast

system and at the same time exhibiting a prompt neutron lifetime characteristic of a thermal system. The theory to describe a coupled fast-thermal reactor was given by Avery [2] and the principle was experimentally demonstrated in the zero-power, coupled fast-thermal critical facility ZPR-V [3]. The coupled-spectrum core design was later adopted in many experimental facilities [4-7] to produce a targeted fast spectrum in a reduced central zone while achieving criticality through a thermal-spectrum booster zone. The coupled core configuration allows a significant reduction of fissile materials and a higher flexibility due to the thermal-spectrum kinetics parameters.

In recent years, coupled fast-thermal spectrum core designs emerged in some applications. Subcritical blanket system for accelerator-driven systems and hybrid fusion-fission reactors were proposed [8]. In France, within the framework for ZEPHYR (Zero power Experimental PHYsics Reactor) project, coupled fast-thermal cores are considered [9] for future experimental programs dedicated to improving nuclear data to cope with awaited target uncertainties for Generation-IV fast reactors [10]. In the United States, for the Versatile Test Reactor (VTR) program to develop a fast spectrum test reactor to support advanced nuclear reactor research and development, a versatile coupled test reactor (VCTR) concept was seriously considered [11], although a full fast core was finally selected. In a fast reactor design with locally moderated target assemblies for minor actinide transmutation [12], the local thermal spectrum helps increase the capture reaction rates of minor actinides such that they are easily transmuted into fissile nuclides and eventually burned through fission. Recently, Niowave, Inc. proposed a HYbrid spectrum Subcritical Testbed (HYST) for neutron irradiation test of novel fuel and cladding materials [13], and has built and operated a small-scale zero-power demonstration facility HYST-1 [14]. Despite the active role of coupled-spectrum reactors in various applications, the CFTR concept is not as widely adopted as

thermal or fast spectrum reactors in nuclear industry. Consequently, an accurate and efficient numerical modeling and simulation capability for CFTR core design and analysis is still in absence.

A complete reactor core design usually starts with assessing the core performance with fuel depletion in steady and transient states. Legacy core calculation methods and computer codes for conventional fast or thermal reactors were developed based on different approximations tailored for specific reactor types. For coupled-spectrum systems, only theoretical methods have been extensively studied, mainly focused on multipoint kinetics methods [2, 15-17]. The multipoint methods require pre-determined coupling coefficients and kinetic parameters [2]. Determination of these integral parameters requires the knowledge of the spatial and energy distribution of neutron flux, which is the pursued solution in core calculations. Previously, full-core Monte Carlo simulations were used to evaluate these coupling coefficients for transient analyses with multipoint kinetics model [8,18,19]. Given this situation, an efficient method (other than Monte Carlo) is in need to perform routine core calculations for coupled-spectrum reactors.

1.2 Research Scope

A nuclear fission reactor is a complex system that involves multiple coupled physical phenomena, including particle transport, nuclear depletion and activation, temperature field evolution, and structural change due to irradiation and thermal feedback. Each of the physical aspects extends over wide ranges in the time, space, and energy domains. A direct multiphysics simulation considering all the aspects of physics remains an extremely daunting task. The primary goal of neutronics simulation of nuclear fission reactors is to determine the reactivity level, neutron flux and reaction (mainly fission) rate distributions in the reactor core, and their evolution with time. In this thesis, we only consider neutron transport coupled with fuel depletion in normal

operating conditions. The long-term temporal evolution of neutron transport is handled in a quasi-static way. Specifically, the flux fluctuations arising from short-time phenomena such as reactivity perturbation and rapid transients in accidental scenarios are not considered. Prompt and delayed neutrons are combined, and the time derivative of flux is neglected. The reactor is assumed to undergo fuel depletion under slowly varying neutron fluxes obtained from a sequence of steady-state neutron transport calculations. The thermal feedback due to changed temperature field with fuel depletion is not addressed in this dissertation.

The steady-state neutron flux field conforms to the time independent Boltzmann transport equation given as [20]:

$$\hat{\Omega}\cdot\nabla\psi(\vec{r},\hat{\Omega},E)+\Sigma_t(\vec{r},E)\psi(\vec{r},\hat{\Omega},E)=\int_0^\infty dE'\int_{4\pi}d\hat{\Omega}'\Sigma_s(\vec{r},E'\to E,\hat{\Omega}'\cdot\hat{\Omega})\psi(\vec{r},E',\hat{\Omega}') +Q(\vec{r},E,\hat{\Omega}), \tag{1.1}$$

where $\psi(\vec{r},E,\hat{\Omega})$ is the neutron angular flux in a six-dimensional phase space: three in position $\vec{r}$, two in angle $\hat{\Omega}$, and energy E. Σ_t and Σ_s are space and neutron energy dependent total and scattering cross sections, respectively. The steady state is maintained by an external source $Q(\vec{r},E,\hat{\Omega})$ or by the fission source in a nuclear reactor:

$$Q(\vec{r},E,\hat{\Omega})=\frac{1}{4\pi k}\chi(\vec{r},E)\int_0^\infty dE'\nu\Sigma_f(\vec{r},E')\int_{4\pi}d\hat{\Omega}'\,\psi(\vec{r},E',\hat{\Omega}'), \tag{1.2}$$

where Σ_f is fission cross section, ν is number of neutrons emitted per fission, χ is fission emission spectrum assumed independent of incident neutron energy, and k is effective multiplication factor acting as the eigenvalue to the resultant homogeneous problem with fission source only. Here the fission source is assumed to have isotropic angular distribution.

The nuclide transmutation is described by the Bateman equation (1.3), where N_i is number density of nuclide i, γ_{jx}^{i} is the yield fraction of nuclide i from type x reaction of nuclide j, R_{jx} is

the coefficient characterizing type x reaction rate of nuclide j, R_{ia} is the loss rate coefficient of nuclide i due to neutron absorption, λ_i is decay constant of nuclide i, N_{i0} denotes initial number density of nuclide i, and I is the total number of active nuclides undergoing nuclear transmutation.

$$\frac{d}{dt}N_i(\vec{r},t) = \sum_{j\neq i}\left[\sum_x \gamma_{jx}^i R_{jx}(\vec{r},t)\right]N_j(\vec{r},t) - [R_{ia}(\vec{r},t)+\lambda_i]N_i(\vec{r},t),$$
$$N_i(\vec{r},0) = N_{i0}, \qquad i = 1,2,\dots I, \tag{1.3}$$

Under quasi-static approximation, the coupling between neutron flux and nuclide density fields is through the macroscopic cross sections $\Sigma_x(\vec{r},E)$ in Eq. (1.1) and reaction rate coefficient $R_{jx}(\vec{r},t)$ in Eq. (1.3):

$$\Sigma_x(\vec{r},E) = \sigma_{ix}(E)N_i(\vec{r}), \tag{1.4}$$

$$R_{jx}(\vec{r},t) = \begin{cases} \int_0^\infty \sigma_{jx}(E)\phi(\vec{r},t)dE\,, & \text{for neutron reactions} \\ \lambda_j, & \text{for radioactive decay} \end{cases}, \tag{1.5}$$

where σ_{ix} and σ_{jx} are microscopic cross sections. Eq. (1.4) is evaluated at discrete time points for steady-state neutron transport calculations. Using the fluxes of a series of steady-state transport solutions, the reaction rates in Eq. (1.5) are evaluated and interpolated or extrapolated to determine the average or smoothly varying reaction rates within each discretized time interval for solving Eq. (1.3).

Three major topics are covered in this dissertation: methods to prepare multigroup cross section data, methods for whole-core transport calculations, and methods for fuel depletion calculations. Although each of them can be expanded into a broad research area, the focus here is to utilize whatever existing research outcomes and improve or adapt them to develop an integral computational procedure that is applicable to coupled-spectrum reactor analyses. Dedicated studies in lattice calculation methods for cross section generation or development of new transport

solvers are not pursued. The multigroup cross section generation will heavily rely on Monte Carlo simulations. Nevertheless, uncertainties in the deterministic transport solution due to the statistical nature of the multigroup cross section data generated by Monte Carlo techniques are out of the research scope. Instead, Monte Carlo calculations were performed with sufficiently large number of particle histories to ensure that statistically meaningful results were produced. The criterion for the selection of the results to be included and compared in this thesis is that those values are significantly different in a statistical sense. When necessary, further clarifications will be made in cases where the results are comparable within their statistical uncertainties. On the neutron transport and fuel depletion calculations, the focus is developing efficient low-order transport models and dealing with the environmental effects on the effective multigroup cross sections and equivalence parameters for nodal calculations. Multiple strategies were investigated for generating cross sections without employing heterogeneous full-core models.

1.3 Thesis Outline

The objective of this thesis work is to develop a new two-step method for efficient whole-core neutronic analysis of CFTRs, by improving the existing fast reactor analysis approach based on multigroup nodal transport method and whole-core isotopic depletion calculation. The dissertation is organized as follows.

In Chapter 2, the readily available core calculation methods are reviewed with an emphasis on the challenges caused by the multigroup approximation of deterministic methods. The review is focused on the legacy two-step methods and the main differences between two tiers of methods dedicatedly developed for thermal and fast reactors are highlighted. It is also explained why a two-step method is proposed for coupled-spectrum reactor analysis. After the methodology review, it is decided to develop the new method based on the existing fast reactor analysis tools. In Chapter

3, preliminary tests of these tools for coupled reactor analysis are performed using a simplified one-dimensional problem. Limitations in the existing tools for cross section generation, nodal core calculation, and depletion analysis are clarified, and potential improvements are proposed.

The proposed two-step methods for coupled reactor analysis are detailed in Chapter 4. The three aspects of neutronics core calculation, i.e., multigroup cross section preparation, full-core transport calculation, and fuel depletion calculation, are discussed in separate sections. For each of them, case studies and examples are provided to develop the rationale of each choice made in the proposed method. At the end of Chapter 4, the overall computational procedure is summarized. The developed methods are then tested for steady-state nodal transport analysis and whole-core depletion calculation in Chapter 5 and Chapter 6, respectively. Chapter 7 summarizes the whole work and provides suggestions for future studies.

Chapter 2

Overview of Current Methodologies

There are two fundamentally different computational approaches, namely Monte Carlo (MC) and deterministic methods, for neutron transport analyses. MC methods are based on probabilistic simulation of the transport process and estimate physical quantities such as flux and reaction rates through the collective behavior of a large number of simulated particles with random and independent histories. Deterministic methods instead solve a system of algebraic equations obtained by discretizing the Boltzmann transport equation in each of its independent variables. Since the dawn of nuclear energy engineering, both MC and deterministic methods have been actively developed and implemented in many computer codes. Most recently, hybrid MC and deterministic methods are being proposed to enhance the strengths and overcome the limitations of individual approaches.

In this chapter, preexisting methods commonly used for full-core calculations are briefly reviewed with a focus on the legacy two-step methods. For each of them, the main drawbacks when applied to coupled-spectrum reactors are highlighted. In short, MC methods are directly applicable but are limited by computational efficiency. Both one-step and two-step deterministic methods have major deficiencies regarding preparation of effective multigroup cross sections. The requirement of huge computational resources of one-step deterministic transport methods is a substantial impediment to routine design calculations. It appears that the hybrid MC and deterministic approach is a promising direction to follow.

2.1 Monte Carlo Methods

Monte Carlo methods for particle transport have been driving computational developments since the beginning of modern computers [21,22]. The transport process is modeled by applying known interaction laws to simulate the random histories of radiation particles and averaging the results over the histories. Specifically for neutron transport simulation, a history starts with a neutron produced from fission or external source, undergoes various interactions with materials, and terminates until the neutron gets absorbed or leaks out of the problem domain. In a specific neutron history, when, where, and how the neutron interacts with matter is randomly sampled from specified probability distributions and hence is stochastic in nature. Nevertheless, physical quantities of interest such as neutron flux and reaction rates in the reactor are determined by the collective behavior of neutrons. According to the law of large numbers, when many independent neutron histories following the same probability distributions are simulated, the average result of certain estimation made in each history approaches the expected value in the system.

2.1.1 Advantages of Monte Carlo Methods

Reactor physics is one of the most suitable and successful application areas of MC methods while the extremely complex energy dependence of neutron interaction cross section poses a substantial challenge to deterministic methods. Since there is no discretization of space, angle, and energy phases in MC simulation, the exact (continuous energy) physics of neutron transport process is modeled, and the representation of complex geometries is explicit and usually of high-fidelity. With known geometry and cross sections, MC simulation results would contain only statistical errors. MC methods are widely applied because the fundamental theory is straightforward, and the implementation is reactor agnostic. In other words, a MC code can be used to analyze different types of reactors without major modification (mostly because of

unsupported geometry or missing particle reaction laws). People often turn to MC codes for initial analyses and feasibility studies of new reactor concepts.

2.1.2 Challenges in Monte Carlo Methods

According to the central limit theorem, the statistical error in the estimated quantity with Monte Carlo is, with probability 0.68, bounded by [23]:

$$\hat{\sigma} \leq \frac{\sigma}{\sqrt{N_{MC}}}, \tag{2.1}$$

where $\hat{\sigma}$ is the standard deviation of sample average, i.e., MC estimation, σ is the true standard deviation of the quantity of interest, and N_{MC} is the number of independent histories in MC simulation. That is, increasing the number of simulated particles will decrease the statistical error with high probability. However, the inverse square root proportionality indicates a slow convergence rate of reducing statistical errors by increasing the number of samples. It also implies a challenge to MC when trying to tally rare events in a system like the response in a detector far from the source. This is a fundamental difficulty of MC methods. To overcome this difficulty, numerous variance reduction techniques have been developed to conduct biased sampling in MC codes [24-27]. However, these techniques require user expertise to provide problem dependent biasing parameters, which is another laborious task.

Nowadays with advancements in numerical algorithms, computer infrastructures, and modern programming implementations, many MC transport codes have been used in reactor core design and benchmark calculations [28-32]. MC is suitable for calculating integral parameters such as eigenvalue and average power in fuel assemblies but is inefficient to estimate detailed local quantities such as pin power/flux accurately. The computational efficiency issue hinders routine applications of MC methods in multiphysics simulations. For example, fuel depletion calculations

require to determine reaction rates in individual fuel pins. In coupled neutronics and thermal-hydraulic calculations, even sub-pin heat source distributions need to be evaluated to predict the peaking temperature accurately to validate the designed safety margin. While steady-state criticality calculations for specific core configurations can be carried out on workstations in a reasonable wall clock time. A full-core pin-by-pin depletion calculation can easily take thousands of CPU hours. Coupled MC transport and thermal-fluidic calculations [33-35] are also beyond the scope of routine simulations as the required computational resources for a mini-core problem can only be provided with supercomputer clusters.

2.2 Deterministic Methods

Deterministic methods are characterized by the way to discretize the neutron transport equation (NTE) and to form a system of algebraic equations. Because of the distinct dependencies of NET on the energy, space, and angle variables, different methods are developed for their discretization. Common spatial discretization methods include the finite difference, nodal, finite element, characteristic, and collision probability methods. The former two methods are favored with regular mesh grids while the latter three are preferred for unstructured meshes. The spatial dependence of cross sections is typically treated with spatial discretization, assuming constant cross section within each spatial cell. The discretization of the angle (travel direction of neutron) variable is generally through either discrete-ordinates (S_N) or spherical harmonics (P_N) method. Alternatively, the angular dependency can be eliminated under the diffusion approximation. Of all the independent variables, energy is probably the most problematic one because of the complex energy dependence of cross sections. However, the multigroup approximation is almost universally applied to discretize the energy variable. While major advances have been made in the spatial and angular discretization methods, the multigroup approximation leads to the fundamental

difficulty of obtaining problem-dependent multigroup cross sections accurately and efficiently. These multigroup cross sections are defined as effective average parameters to represent the neutron reaction rates when multiplied with integrated fluxes in each discretized energy interval.

2.2.1 Multigroup Approximation

In the multigroup approach, the time independent neutron transport equation (**Error! R eference source not found.**) can be rewritten as [23]:

$$\hat{\Omega}\cdot\nabla\psi_g(\vec{r},\hat{\Omega})+\Sigma_{t,g}(\vec{r},\hat{\Omega})\psi_g(\vec{r},\hat{\Omega})=\sum_{g'}^{G}\int_{4\pi}d\hat{\Omega}'\Sigma_{s,g'\to g}(\vec{r},\hat{\Omega}',\hat{\Omega})\psi_{g'}(\vec{r},\hat{\Omega}') +Q_g(\vec{r},\hat{\Omega}),\qquad \vec{r}\in V,\ \hat{\Omega}\in 4\pi,\ 1\le g\le G. \tag{2.2}$$

The angular flux $\psi_g(\vec{r},\hat{\Omega})$ for group g is defined as:

$$\psi_g(\vec{r},\hat{\Omega})=\int_{E_g}^{E_{g-1}}\psi(\vec{r},E,\hat{\Omega})dE\,. \tag{2.3}$$

where E_g and E_{g-1} are the energy boundaries of group g. Ignoring the external source and the incident energy dependency of fission spectrum, the integral source $Q_g(\vec{r},\hat{\Omega})$ in group g is:

$$Q_g(\vec{r},\hat{\Omega})=\frac{\chi_g(\vec{r})}{4\pi k}\sum_{g'=1}^{G}\nu\Sigma_{fg'}(\vec{r})\phi_{g'}(\vec{r})\,, \tag{2.4}$$

where

$$\chi_g(\vec{r})=\int_{E_g}^{E_{g-1}}\chi(\vec{r},E)dE\,,\qquad \phi_{g'}(\vec{r})=\int_{4\pi}\psi_{g'}(\vec{r},\hat{\Omega}')d\hat{\Omega}'\,. \tag{2.5}$$

The rigorous multigroup cross sections are defined as:

$$\Sigma_{t,g}(\vec{r},\hat{\Omega})=\frac{\int_{E_g}^{E_{g-1}}\Sigma_t(\vec{r},E)\psi(\vec{r},E,\hat{\Omega})dE}{\int_{E_g}^{E_{g-1}}\psi(\vec{r},E,\hat{\Omega})dE}, \tag{2.6}$$

$$\Sigma_{s,g'\to g}(\vec{r},\hat{\Omega}',\hat{\Omega})=\frac{\int_{E_g}^{E_{g-1}}\int_{E_{g'}}^{E_{g'-1}}\Sigma_s(\vec{r},E'\to E,\hat{\Omega}'\cdot\hat{\Omega})\psi(\vec{r},E',\hat{\Omega}')dE'dE}{\int_{E_{g'}}^{E_{g'-1}}\psi(\vec{r},E',\hat{\Omega}')dE'},\tag{2.7}$$

$$\nu\Sigma_{fg'}(\vec{r})=\frac{\int_{E_g}^{E_{g-1}}\nu\Sigma_f(\vec{r},E')\left[\int_{4\pi}\psi(\vec{r},E',\hat{\Omega}')d\hat{\Omega}'\right]dE'}{\int_{E_g}^{E_{g-1}}\left[\int_{4\pi}\psi(\vec{r},E',\hat{\Omega}')d\hat{\Omega}'\right]dE'}.\tag{2.8}$$

The rigorous total and scattering cross sections are angle dependent and are not convenient to be incorporated in conventional deterministic code implementations [36]. In common practice, the angular dependence of scattering cross section is expressed as Legendre polynomial expansion:

$$\Sigma_s(E'\to E,\hat{\Omega}'\cdot\hat{\Omega})=\sum_{l=0}^{L}\frac{2l+1}{4\pi}\Sigma_{sl}(E'\to E)P_l(\mu),\qquad \mu=\hat{\Omega}'\cdot\hat{\Omega}\in[-1,1],\tag{2.9}$$

where $P_l(\mu)$ is Legendre polynomial of order l. According to the addition theorem of spherical harmonics,

$$P_l(\hat{\Omega}'\cdot\hat{\Omega})=\frac{4\pi}{2l+1}\sum_{k=-l}^{l}\bar{Y}_{lk}(\hat{\Omega}')Y_{lk}(\hat{\Omega}),\tag{2.10}$$

where $\bar{Y}_{lk}(\hat{\Omega}')$ and $Y_{lk}(\hat{\Omega})$ are spherical harmonics. Accordingly, the scattering source term in Eq. (2.2) can be rewritten as:

$$\begin{aligned}S_g(\vec{r},\hat{\Omega})&=\sum_{g'}^{G}\int_{E_g}^{E_{g-1}}dE\int_{E_{g'}}^{E_{g'-1}}dE'\int_{4\pi}d\hat{\Omega}'\Sigma_s(\vec{r},E'\to E,\hat{\Omega}'\cdot\hat{\Omega})\psi(\vec{r},E',\hat{\Omega})\\&=\sum_{g'}^{G}\sum_{l=0}^{L}\sum_{k=-l}^{l}Y_{lk}(\hat{\Omega})\Sigma_{sl,g'\to g}(\vec{r})\int_{E_g}^{E_{g-1}}dE\int_{E_{g'}}^{E_{g'-1}}dE'\int_{4\pi}d\hat{\Omega}'\bar{Y}_{lk}(\hat{\Omega}')\psi(\vec{r},E',\hat{\Omega}).\end{aligned}\tag{2.11}$$

Correspondingly, the multigroup scattering cross sections are defined as:

$$\Sigma_{slk,g'\to g}(\vec{r})=\frac{\int_{E_g}^{E_{g-1}}dE\int_{E_{g'}}^{E_{g'-1}}dE'\Sigma_{sl}(\vec{r},E'\to E)\psi_{lk}(\vec{r},E')}{\int_{E_{g'}}^{E_{g'-1}}\psi_{lk}(\vec{r},E')dE'},\tag{2.12}$$

where $\psi_{lk}(\vec{r},E')$ is angular flux moment:

$$\psi_{lk}(\vec{r},E') = \int_{4\pi} d\hat{\Omega}' \bar{Y}_{lk}(\hat{\Omega}')\psi(\vec{r},E',\hat{\Omega})\,. \tag{2.13}$$

To eliminate the angular dependence of the total cross section, the total reaction rate term is expanded with spherical harmonics and Eq. (2.2) can be rearranged as:

$$\hat{\Omega}\cdot\nabla\psi_g(\vec{r},\hat{\Omega}) + \tilde{\Sigma}_{t,g}(\vec{r})\psi_g(\vec{r},\hat{\Omega}) = \sum_{g'}^{G}\sum_{l=0}^{L}\sum_{k=-l}^{l} Y_{lk}(\hat{\Omega})\,\tilde{\Sigma}_{slk,g'\to g}(\vec{r})\psi_{lk,g'}(\vec{r}) + \frac{\chi_g(\vec{r})}{4\pi k}\sum_{g'=1}^{G}\nu\Sigma_{fg'}(\vec{r})\phi_{g'}(\vec{r})\,. \tag{2.14}$$

In Eq. (2.14), $\tilde{\Sigma}_{t,g}(\vec{r})$ is an arbitrarily selected total cross section that is independent of angle and the modified scattering cross section is:

$$\tilde{\Sigma}_{slk,g'\to g}(\vec{r}) = \Sigma_{slk,g'\to g}(\vec{r}) + \left[\tilde{\Sigma}_{t,g}(\vec{r}) - \Sigma_{tlk,g}(\vec{r})\right]\delta_{gg'}, \tag{2.15}$$

where $\delta_{gg'}$ is Kronecker delta function and $\Sigma_{tlk,g}(\vec{r})$ is the flux moment weighted total cross section:

$$\Sigma_{tlk,g}(\vec{r}) = \frac{\int_{E_g}^{E_{g-1}}\Sigma_t(\vec{r},E)\psi_{lk}(\vec{r},E)dE}{\int_{E_g}^{E_{g-1}}\psi_{lk}(\vec{r},E)dE}. \tag{2.16}$$

In the widely adopted consistent P_N and extended transport approximation [36], $\tilde{\Sigma}_{t,g}(\vec{r})$ is chosen to be the scalar flux (zeroth flux moment) weighted total cross section. This approximation requires to determine the weighting spectra from angularly dependent spectrum calculations.

Other than the truncation of scattering order, the fundamental dilemma in Eq. (2.14) is that the exact angular flux required to define multigroup cross sections is unknown before the continuous energy transport equation (1.1) is solved. Therefore, numerical calculations must work with multigroup cross sections obtained with approximate weighting spectrum. If the number of energy groups is sufficiently large, multigroup cross sections are insensitive to the weighting spectrum. With that, the number of unknowns and the size of the system of algebraic equations

would be tremendous and huge memory storage would be required, which significantly deteriorate the computational efficiency of deterministic methods. In full-core calculations, the discretized energy grids should be limited to at most a few tens because the spatial discretization usually requires a higher resolution. With a coarse energy model, multigroup cross sections should be condensed with a flux (moment) spectrum close to the desired flux solution.

Depending on the model to obtain multigroup cross sections, two groups of deterministic methodologies are recognized: 1) legacy two-step methods consisting of high-order transport calculations for assembly lattices and full-core low-order transport or diffusion calculations, and 2) direct (or one-step) full-core transport methods. Because of the distinct spectrum characteristics of different types of reactors as shown in Figure 2.1, different approximations tailored for specific reactor types are adopted in these developed methods.

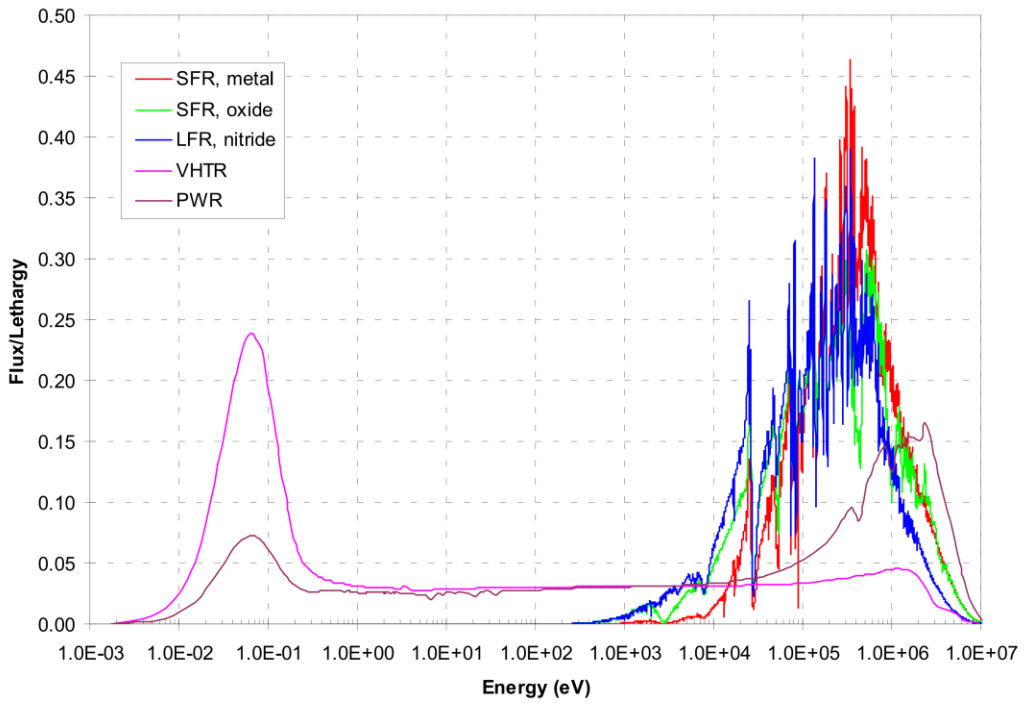

Figure 2.1 Characteristic Neutron Energy Spectra in Different Types of Reactor Cores (Adapted from the lecture notes of NERS 561 class given by Prof. Won Sik Yang at UM)

It is seen that the thermal reactors (PWR and VHTR) spectra show obvious thermal flux peaks and a much smoother flux variation than the fast reactors. In the heavy nuclide resonance region (eV to keV range), the 1/E spectrum of thermal reactors is used as a basis for resonance self-shielding calculations [37]. In fast reactors, the small slowing-down power produces a flux spectrum centered in the keV to MeV energy range. The strongly jagged structure of fast reactor spectra is mainly due to the scattering resonance of intermediate mass nuclides in coolant and structure. The lack of dominant heavy nuclides causing resonance and 1/E asymptotic spectrum in fast reactors necessitate the use of a detailed energy model for slowing-down calculations. The harder spectrum also incurs non-negligible threshold reactions like (n,2n), (n,p), and inelastic scattering, and pronounced scattering anisotropy and unresolved resonance self-shielding effects in fast reactors. [38] Another important difference is that the long neutron mean free path (MFP) causes global spectrum transition across the fast reactor core. These distinctions in nuclear characteristics gave rise to separately developed cross section generation and full-core calculation methods dedicated to fast or thermal spectrum reactor analysis.

2.2.2 Legacy Two-Step Methods

Legacy two-step methods used a divide-and-conquer strategy to solve whole-core neutron transport problems in multiple steps: (0) preparation of base cross section library for lattice codes, (1) lattice physics calculations to prepare coarse-group (two to dozens of groups depending on reactor type) cross sections, (2) full-core calculation with homogenized coarse-group cross sections from step (1). Step (0) processes cross sections in the finest energy resolution without spatial or angular dependence, but it is not frequently performed and hence not counted in “two-step”. Step (1) treats resonance self-shielding with intermediate energy resolution and local spatial heterogeneity in high resolution. Step (2) solution has the lowest energy resolution but covers the

full problem domain in coarser spatial resolution than lattice calculations. A finer full-core solution can be obtained by combining Step (1) and Step (2) information. Although subtle differences exist among various legacy codes at each of the steps, the following discussions will be focused on the comparison between the methods respectively applied to fast and thermal reactors.

2.2.2.1 Lattice Physics Calculation

Without going through the full list of common lattice codes [39-42], thermal reactor lattice calculations are mostly performed for unique pin cell or two-dimensional (2D) assembly lattice models with heterogeneous geometry representation and fine-group (~100 groups) cross sections. These cross sections are pre-generated in Step 0) and are functionalized with temperature and background cross sections in the resonance energy region such that they can be applied to a wide range of problems (typically limited to the same type of reactor). In thermal lattice codes, the resonance self-shielding calculation is prevalently based on equivalency theory or subgroup method [37]. Detailed flux distribution in a lattice is calculated to consider the strong local heterogeneity effects on spatial and energy self-shielding. However, thermal lattice calculations are generally performed with transport approximation and do not produce high order anisotropic scattering cross sections that are important in fast energy range. Because of the short neutron MFP and the relatively uniform core configuration of commercial thermal reactors, the inter-assembly neutron transport is not significant and reflective boundary conditions are imposed with critical buckling search for leakage correction. Assembly color set (supercell) model are also supported for better modeling of the spectral interference between different types of fuel assemblies or between fuel and reflector [40]. Because of the strong dependence of thermal cross sections on fuel burnup state, fuel depletion calculation is usually incorporated in thermal lattice codes to generate burnup dependent cross sections.

For fast reactor cross section generation, a different series of cross section generation codes [43-47] were developed. The Bondarenko self-shielding factor method was used in early practices for self-shielding treatment. Later, the ultrafine group (UFG) method is primarily adopted for detailed spectrum calculations. In the state-of-the-art MC^2-3 code [47], resonance overlapping is resolved in UFG spectrum calculations for homogeneous or heterogeneous configurations. The self-shielded UFG (~2000 groups) cross sections are prepared either by numerical integration of reconstructed and Doppler broadened pointwise cross sections in the resolved resonance range based on the narrow resonance approximation, or by hyperfine-group (HFG) fixed source calculations for wide resonances. The pointwise cross sections are directly used in the HFG (~400,000 groups) calculations. Unresolved resonances are self-shielded using the analytic resonance integral method. The consistent P_1 multigroup transport equation is solved for one-dimensional (1D) unit cell problems in UFG or HFG level. Recently, to represent the local heterogeneity effects more accurately, the method of characteristics (MOC) was implemented to solve two- (2D) and three-dimensional (3D) assembly problems [48]. Like thermal lattice codes, the resulting UFG cross sections can be homogenized and condensed into broad-group cross sections with fundamental mode spectrum. To consider the global spectral transition effects in fast reactors, the UFG calculation is typically performed for 2D region homogenized full-core problems to generate region-dependent broad-group cross sections.

Thermal and fast lattice codes are characterized by their self-shielding calculation methods. The use of UFG method in fast lattices code eliminates the need of pre-generated fine-group libraries and in principle they can be applied to a wider range of problems. In fact, MC^2-3 has been extended to generate multigroup cross sections in the thermal energy range as well as in the fast energy range [49]. However, the computational inefficiency of the UFG method limits its

application to large-sized problems. From the core calculation point of view, different cross section data are produced from thermal and fast lattice codes. Since the fuel depletion is already incorporated in thermal lattice calculations, macroscopic few-group (usually less than ten) cross sections are prepared and functionalized with state condition parameters including burnup. Comparatively, whole-core depletion calculations are performed for fast reactors because of the global spectral transition effects. For this purpose, isotopic multigroup cross sections are generated from lattice calculations. As region dependent spectra are incorporated in the group condensation and a multigroup structure finer than that used for thermal core calculations is used in fast core calculations, the isotopic multigroup cross sections are assumed constant during fuel depletion.

2.2.2.2 Homogenization Process

Legacy methods for full-core calculations require homogenized multigroup cross sections from lattice codes. This process includes spatial homogenization as well as group condensation, mostly with flux-volume weighting:

$$\bar{\Sigma}_{\alpha,g} = \frac{\int_V d\vec{r} \int_{E_g}^{E_{g-1}} dE \Sigma_\alpha(\vec{r},E)\phi_h(\vec{r},E)}{\int_V d\vec{r} \int_{E_g}^{E_{g-1}} dE \phi_m(\vec{r},E)}, \tag{2.17}$$

where $\bar{\Sigma}_{\alpha,g}$ is the homogenized cross section for reaction type α in a spatial region V (called node), and ϕ_h and ϕ_m are the flux in the heterogeneous and homogenized region, respectively. This definition intends to preserve the average reaction rates of the reference heterogeneous problem in the homogenized calculation. However, it is well known that the cross sections homogenized by the flux-volume weighting generally do not preserve the reference surface leakages simultaneously because of the lack of degree of freedom in the homogenization process [50-53].

Conventionally, the additional degree of freedom is introduced by certain equivalency parameters, including flux discontinuity factor (DF) [51], super-homogenization (SPH) factor

[52], and black box homogenization (BBH) method [53]. DF is widely adopted in nodal diffusion calculations to allow flux discontinuity on nodal surfaces. Discontinuity factors are typically generated for the radial boundaries of homogenized assembly in 2D lattice calculations simply as the ratios of surface-averaged to node-averaged fluxes. Axial discontinuity factors derived in 3D transport calculations were also introduced for some BWR problems to capture the strong axial heterogeneity [54]. SPH factor is transport-solver-agnostic and can be absorbed into multigroup cross sections without extra memory cost, and hence are mostly used in pin-by-pin calculations to reproduce pin-level reaction rates. But the determination of SPH factors is a nonlinear iteration procedure. As an extension to SPH and DF methods, the BBH method intends to reproduce reference reaction rates and net leakage by preserving partial currents on nodal surfaces. At each surface, two discontinuity factors are used.

While discontinuity factors have been routinely and successfully used in diffusion theory core calculations, they are not broadly adopted in transport calculations although several efforts have been dedicated. Transport equivalence methods have been introduced in terms of SPH factors [52], even parity discontinuity factors [55,56], cross section correction [57], and angular flux discontinuity factors [58,59]. These equivalence models are mainly developed for integro-differential transport equation to improve full-core pin-resolved transport calculations.

2.2.2.3 Full Core Calculation

Legacy full-core calculations are predominantly based on advanced nodal methods developed since early 1980s to replace the expensive fine-mesh finite difference methods [60]. These nodal methods are essentially not associated with specific spectrum systems. With reliable multigroup cross sections, they can be applied to fast, thermal, or coupled fast-thermal spectrum

reactors. Among these nodal methods, the nodal expansion methods and analytical nodal methods based on the transverse integration procedure are mostly widely used in production analysis [38]. Because of the strong local heterogeneity effects, discontinuity factors were incorporated in most nodal codes for thermal reactor core calculations [61-63].

Specifically for fast reactor analysis, the DIF3D-Nodal code [65] was initially developed for full-core diffusion calculations using the transverse integrated nodal expansion method. Later in order to treat the pronounced scattering anisotropy and transport effects in fast reactors, the DIF3D-VARIANT code [66,67], or briefly referred to as VARIANT, was developed based on variational nodal transport method [68]. It solves the second order even-parity transport equation in a variational approach. In VARIANT, flux and source are expanded using hierarchical complete polynomial trial functions in space and spherical harmonics or simplified spherical harmonics in angle and the coupling between nodes is through continuity of even- and odd-parity flux moments rather than transvers integration of leakage. Spatial and angular approximation orders in VARIANT can be consistently refined to achieve higher solution accuracy. Compared to the transverse integration nodal methods, VARIANT diffusion (P_1 expansion) solution provides systematic flux/power reconstruction with 3D basis functions [69]. Since the assembly homogenization error is relatively small in typical fast reactors, initially no discontinuity factor was incorporated in DIF3D-Nodal and VARIANT. Subsequently, a nodal equivalence theory based on scalar flux DFs was implemented in VARIANT for prismatic Very High Temperature Reactor (VHTR) analysis [70], but it was limited to the P_1 approximation. Recently, a scalar flux DF approach was also applied to a diffusion theory variational nodal method [71].

Regarding depletion and fuel cycle analysis, thermal reactor codes do not perform depletion calculations explicitly but use burnup dependent macroscopic cross sections as look-up

tables in whole-core calculations. Even though the micro-depletion calculation capability was introduced in recent updates of several thermal nodal codes [63,64], the focus was to correct the error in the interpolated macroscopic cross sections due to deviated depletion history in core calculations. On the other hand, fast reactor fuel cycle analysis is carried out at the core calculation stage. The REBUS-3 code [72,73] is a classic fast reactor fuel cycle analysis code used for both explicit cycle-by-cycle calculation under a specified fuel management scheme and for determining the equilibrium state under a fixed and periodic fuel management scheme. REBUS-3 utilizes DIF3D [74], DIF3D-Nodal, VARIANT, or TWODANT [75] as the flux solver. While constant isotopic cross sections are routinely used for fast reactor fuel cycle analyses, a limited capability is available to use burnup dependent capture and fission cross sections. [73]

2.2.3 Direct Full-Core Transport Methods

Direct full-core transport methods are often referred to as "one-step" deterministic methods as the lattice calculation and full-core calculation are integrated into one step. The one-step deterministic codes like nTRACER [76] and MPACT [77] developed for thermal reactor analysis still require functionalized cross section libraries for online resonance self-shielding treatment. The PROTEUS code [78,79] developed under the Nuclear Engineering Advanced Modeling and Simulation (NEAMS) program can also use the subgroup method or resonance table method for self-shielding calculation on the fly. However, to be applied to a wide range of problems, an ultrafine-group base library should be prepared [80]. Therefore, practical high-fidelity transport calculations for fast reactors using PROTEUS are usually performed with broad-group cross sections generated externally. One-step methods target high-order transport calculations for explicit (pin-resolved) full-core models. Rather less approximations in spatial and angular discretization are made compared to legacy two-step methods. Multiphysics phenomena like fuel

depletion and thermal feedback are modeled by embedded burnup and coupled thermal-hydraulic calculations. Correspondingly, the size of the equation solved by one-step methods increases significantly and extraordinarily large computational resources are required for core calculations. Thus, one-step transport methods are not suitable for routine design calculations.

2.3 Hybrid Monte Carlo-Deterministic Methods

The concept of "hybrid" method was originally attached to improved MC methods using deterministic methods to determine biasing parameters [81-83], or those using deterministic calculation to accelerate fission source convergence in reactor modeling [84,85]. Another tier of hybrid methods are essentially deterministic methods but use nonlinear functionals [86], response matrices [87], or more commonly multigroup cross sections [88-91] generated from MC simulations. Among these hybrid methods, those based on deterministic solvers and multigroup cross sections generated with MC received the most attentions because of their compatibility with the legacy code implementation. Using MC simulation for cross section generation, the difficulties in resonance self-shielding treatment and complex geometry modeling with conventional lattice codes are eliminated to a large extent. The only major drawback with MC is the generation of anisotropic scattering cross sections and transport corrected total cross section (or transport cross section).

As shown in Eq. (2.12), the scattering cross sections should be flux moment weighted. However, it is not feasible to tally flux moments in standard MC simulations as the tallied results of near-zero flux moments would bear significant uncertainties. Consequently, anisotropic scattering cross sections are typically weighted with scalar flux spectrum in MC codes [88]. It is noted that using scalar flux weighted anisotropic scattering matrices in deterministic transport calculations would introduce non-negligible errors [92]. Ref. [91] developed a hybrid method for

fast reactor cross section generation, in which MC simulations are used only to produce UFG principal cross sections and isotropic elastic scattering cross sections. Scattering matrices were constructed using tallied isotropic scattering cross sections and energy transfer functions. Broad-group cross sections are then generated with UFG spectrum obtained in deterministic UFG transport calculations.

Anisotropic scattering cross sections are not explicitly involved in diffusion theory calculations. Instead, diffusion coefficient defined with the transport cross section is used. Rigorous determination of transport cross section and diffusion coefficient requires the knowledge of current (P_1 flux moment) spectrum. Because of the same reason just mentioned above, MC codes often generate transport cross section ($\Sigma_{tr,g}$) with the out-scatter approximation:

$$\Sigma_{tr,g} = \Sigma_{t,g} - \frac{\sum_{g'}\left(\Sigma_{s1,g'\to g}J_{g'}\right)}{J_g} \approx \Sigma_{t,g} - \frac{\sum_{g'}\left(\Sigma_{s1,g\to g'}J_{g}\right)}{J_g} = \Sigma_{t,g} - \Sigma_{s1,g}\,, \tag{2.18}$$

where J_g and $\Sigma_{s1,g}$ denotes current and P_1 scattering cross section, respectively. Here the current spectrum cancels out but the P_1 scattering cross section comes from scalar flux weighting. Further group condensation of transport cross section and diffusion coefficient would also turn to scalar flux weighting. To overcome this limitation, alternative approaches were developed in various MC codes to determine diffusion coefficients with current weighted transport cross section [93] or the cumulative migration method (CMM) [94].

2.4 Potential Options for CFTR Analysis

Through the literature survey, MC methods turn to be the only choice that is directly applicable to coupled-spectrum reactor core analysis. But the computational inefficiency makes them inappropriate for scoping design calculations which involve iterations to optimize design parameters. Similarly, one-step deterministic methods are not appropriate either for coupled-

spectrum reactor applications. Among the legacy two-step methods, the fast reactor analysis methods are more applicable to coupled-spectrum systems than those developed for thermal reactors, because of the rigorous self-shielding treatment in fast lattice codes. There is no fundamental difference in the whole-core transport calculation between fast and thermal spectrum reactors with provided group constants. But because a coupled-spectrum reactor would require whole-core depletion calculation for fuel cycle analysis as it shares the fast-reactor feature of significant global spectrum transition effects, the fast reactor core calculation method based on the VARIANT and REBUS-3 codes is preferred in that the whole-core depletion calculation capability with transport flux solution is readily available. The missing parts include a nodal equivalence model to reduce homogenization error, and the support of burnup dependent cross sections for all reactions.

There were attempts to model the coupled-spectrum reactors using existing tools. The conceptual design study for VCTR was performed using a hybrid approach [11]. Multigroup cross sections were generated from a full-core MC simulation with Serpent [29], and deterministic transport calculations were performed with the MAMMOTH code [95]. It was reported that MAMMOTH transport calculations of VCTR yielded eigenvalue errors larger than 1,000 pcm even with the cross sections obtained from a full core Serpent simulation. Later, using SPH factors derived from the reference Serpent full-core solution in MAMMOTH calculations produced accurate eigenvalue and power distribution [96].

Based on these considerations, it was decided to develop an efficient hybrid two-step method for coupled fast-thermal core analysis by improving the current fast reactor analysis methods and by developing a procedure to generate multigroup cross sections and nodal equivalence parameters based on Monte Carlo simulations with Serpent [29] or OpenMC [30]. For

high-order transport calculations, the MC^2-3 code remains an alternative option to generate consistently weighted anisotropic scattering cross sections.

Chapter 3

Limitations in Current Fast Reactor Analysis Methods

As discussed in Chapter 2, the new two-step method for CFTR analysis is to be developed by improving the current fast reactor analysis methods. Therefore, it is necessary to first evaluate the applicability of the legacy fast reactor analysis methods to CFTRs. Quantitative assessments would help highlight the major deficiencies of existing methods and draw a baseline for the development of a new method. For this purpose, a simplified one-dimensional (1D) coupled-spectrum problem was studied to clarify the impact of each approximation adopted in the current methods. This chapter outlines the main challenges encountered in developing a new deterministic method for CFTR analysis. We will see that the biggest difficulty is rooted in the preparation of effective multigroup cross sections (including nodal equivalence parameters) for homogenized nodal calculations.

3.1 1D Coupled Fast-Thermal Spectrum Core Problem

As shown in Figure 3.1, a 1D coupled fast-thermal spectrum reactor (CFTR-1D) problem is constructed using four types of assemblies: one fast fuel assembly (FA), one buffer assembly (BA), one moderated (thermal) fuel assembly (TA), and three graphite reflector assemblies (GRs). Since no moderator occurs in the fast fuel assembly, a fast reactor spectrum is produced in FA. The buffer assembly acts as a fast neutron reflector to the fast fuel assembly while absorbing the thermal neutrons leaking out of the thermal fuel assembly.

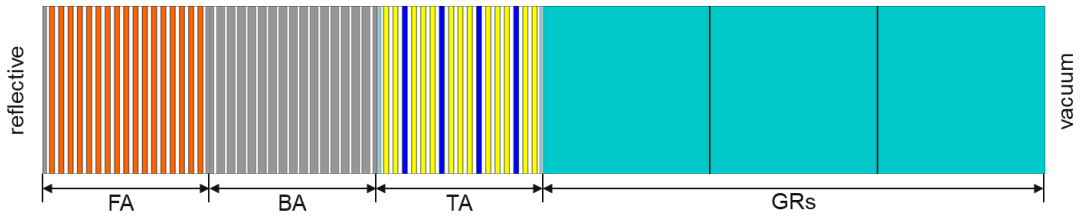

Figure 3.1 Half-Space Configuration of One-Dimensional CFTR

The fast fuel assembly is loaded with 20 at.% enriched uranium zirconium alloy (U-6Zr) that contains 6 wt.% zirconium. The buffer assembly contains only dummy plates made of stainless steel. The thermal fuel assembly is fueled with 7 at.% enriched uranium zirconium alloy (U-10Zr) containing 10 wt.% zirconium and is moderated with zirconium hydride ($ZrH_{1.6}$) solid moderator (blue plates in Figure 3.1). The graphite reflectors are modeled as homogeneous mixture of bulky graphite, coolant and zircaloy box. HT-9 stainless steel is used as the fuel cladding and assembly duct materials of the fast and buffer assemblies while zircaloy cladding/duct are chosen for the thermal fuel assembly. The whole core is universally cooled with sodium. More detailed information of the CFTR-1D model is provided in Appendix A.1.

Using continuous cross sections based on the ENDF/B-VII.0 library, a whole core Serpent [29] Monte Carlo simulation of the CFTR-1D core gives the spectral and spatial distributions of neutron fluxes as shown in Figure 3.2 and Figure 3.3, respectively. In Figure 3.2, GR1 denotes the reflector assembly next to the thermal fuel assembly. It is seen that the neutron spectrum varies significantly from the typical fast reactor spectrum in the fast fuel assembly to the thermal-peaked spectrum in the reflector assembly. It is also noted that the thermal fuel assembly is deeply under-moderated, which yields a transitional spectrum different from prototypical spectrum observed in thermal reactors. But the thermal neutron (E_n < 0.6 eV) fission still makes up about 40% of the total fission rate. The pronounced global spectral transition indicates strong inter-assembly coupling and transport effects.

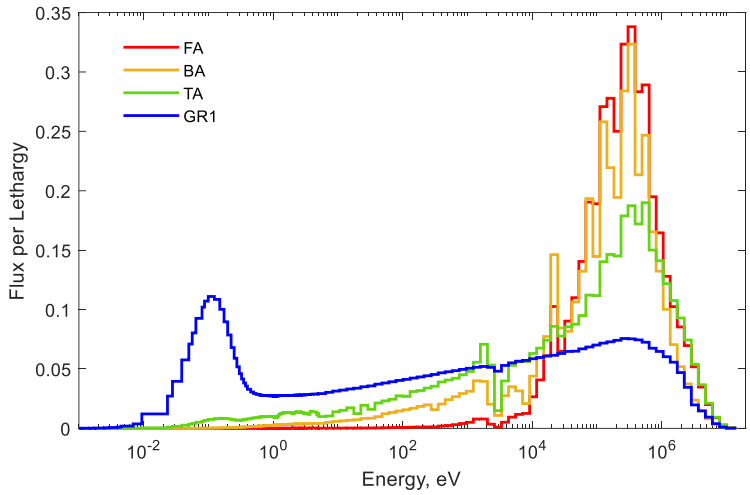

Figure 3.2 Flux Spectra in Different Assemblies of CFTR-1D Core

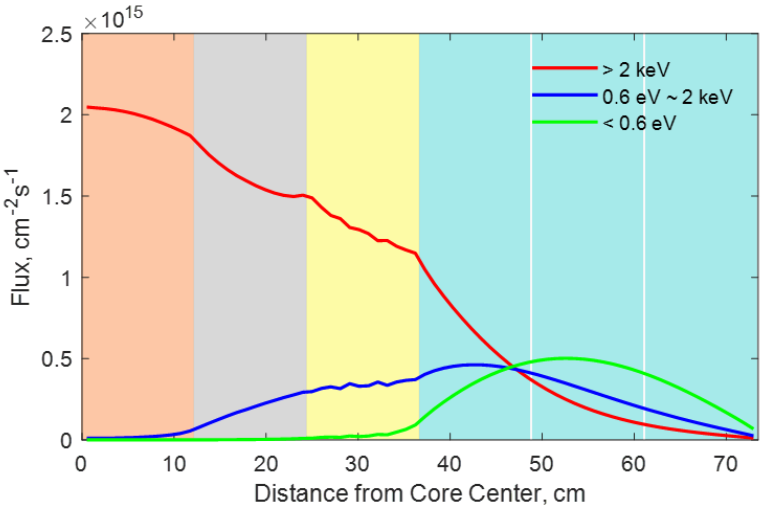

Figure 3.3 Flux Profiles with Distance from Center of CFTR-1D Core

Figure 3.3 shows the flux profiles in three energy ranges: fast (> 2 keV), intermediate (0.6 eV ~ 2 keV), and thermal (< 0.6 eV). Because of the buffer assembly, intermediate and thermal neutrons can hardly enter the fast fuel assembly. It is clearly seen that the graphite reflector assemblies act as the dominant moderators in the system. The large gradients of fast and thermal fluxes indicate significant leakage and transport effects, which may cause difficulties in diffusion theory core calculations. Later, we will see the impact of diffusion approximation in nodal core calculations for this problem.

3.2 Steady-State Transport Calculation

For multigroup nodal core calculations, accurate multigroup cross sections are essential to obtain correct flux solutions. Besides, equivalence parameters are usually introduced to reduce node homogenization errors. To quantify the impacts of individual approximations in nodal core calculations, an assembly homogenized model of CFTR-1D core is first investigated to test the applicability of the conventional approach for fast reactor cross section generation.

3.2.1 Homogenized CFTR-1D Problem

The homogenized CFTR-1D problem is illustrated in Figure 3.4. For this simplified model, the reference broad-group cross sections (BGXSs), including energy release per fission for power calculation, were directly tallied for each assembly in the reference Serpent calculation. The Serpent methodology for generating multigroup cross sections using Monte Carlo tallies is described in Ref. [88]. It is noted that the anisotropic scattering cross sections tallied in Serpent are weighted by scalar flux spectrum instead of the corresponding spectra of angular flux moments because of the infeasibility of tallying flux moments in Monte Carlo simulation. In fast spectrum systems, anisotropic scattering is important and hence needs to be rigorously considered. A previous study [92] showed that the scalar flux weighted anisotropic scattering matrices may cause over 500 pcm k-effective error. Therefore, alternative BGXSs were prepared using MC^2-3, in which high-order scattering matrices are weighted with angular flux moments. The steps to prepare BGXSs with MC^2-3 will be discussed later.

Figure 3.4 Half-Space Configuration of Homogenized CFTR-1D Core

3.2.1.1 Core Calculation with Reference BGXSs

VARIANT nodal transport calculations were performed with P_5 angular approximation and P_3 anisotropic scattering order. The spatial polynomial orders for flux, source, and leakage distribution were 6, 4, and 1, respectively. Parametric studies showed no significant improvement of solution with refined approximation orders. Two sets of reference BGXSs were tallied in 32 and 13 energy groups, respectively, which are described in Appendix B. To eliminate the errors due to scalar flux weighted anisotropic scattering cross sections of Serpent, the reference BGXSs were modified by replacing the anisotropic scattering matrices with those obtained from MC^2-3 full-core calculations. The cross sections were written in the ISOTXS format [97] for use in VARIANT.

In Table 3.1, the VARIANT transport solutions are compared with the reference Serpent solution. The ISOTXS datasets containing modified anisotropic scattering data are labeled with 'mixed'. As expected, neither 32G nor 13G cross sections directly from Serpent tallies predicted the k-effective and power distribution accurately. With the modified scattering matrices, the VARIANT solution with the 13G cross sections had slightly larger errors in eigenvalue and assembly powers but both cross section sets practically reproduced the reference solution.

Table 3.1 VARIANT transport solutions using reference broad-group cross sections

Code	Cross section*	k_{eff}	Std dev / Error	Assembly power error	
				FA	TA
Serpent	ENDF/B VII.0	1.11002	0.00004	–	–
VARIANT	ISOTXS.32G.hom_core_serp	1.11484	0.00482	1.63%	-1.53%
	ISOTXS.32G.hom_core_serp_mixed	1.11050	0.00048	-0.03%	0.03%
	ISOTXS.13G.hom_core_serp	1.11639	0.00637	2.22%	-2.07%
	ISOTXS.13G.hom_core_serp_mixed	1.11082	0.00080	0.18%	-0.17%

*Naming rule for cross section dataset: file_format.xxG.label. xx means number of broad groups and label denotes the method/model to generate the cross sections.

The flux spatial distributions of the VARIANT 32G transport solution with the modified anisotropic scattering matrices are compared to those of the reference Serpent solution in Figure 3.5. In general, the flux distributions predicted by VARIANT agreed with the Serpent results. Noticeable deviations occur in the fast flux shape in the buffer assembly and the intermediate flux shape in the graphite reflector next to the thermal fuel assembly. These deviations are mainly due to the use of spatially uniform BGXSs of each assembly in VARIANT calculations. Since the local spectra in the buffer and reflector assemblies are heavily influenced by the neighboring fuel assemblies, the variation of BGXSs in homogeneous assemblies is non-negligible. This type of homogenization error can be eliminated if a sufficiently fine group structure is used or by using smaller constant cross section zones. In practice, this error is usually blended with the common homogenization error due to local heterogeneity effects and is accommodated by equivalence parameters in nodal calculations.

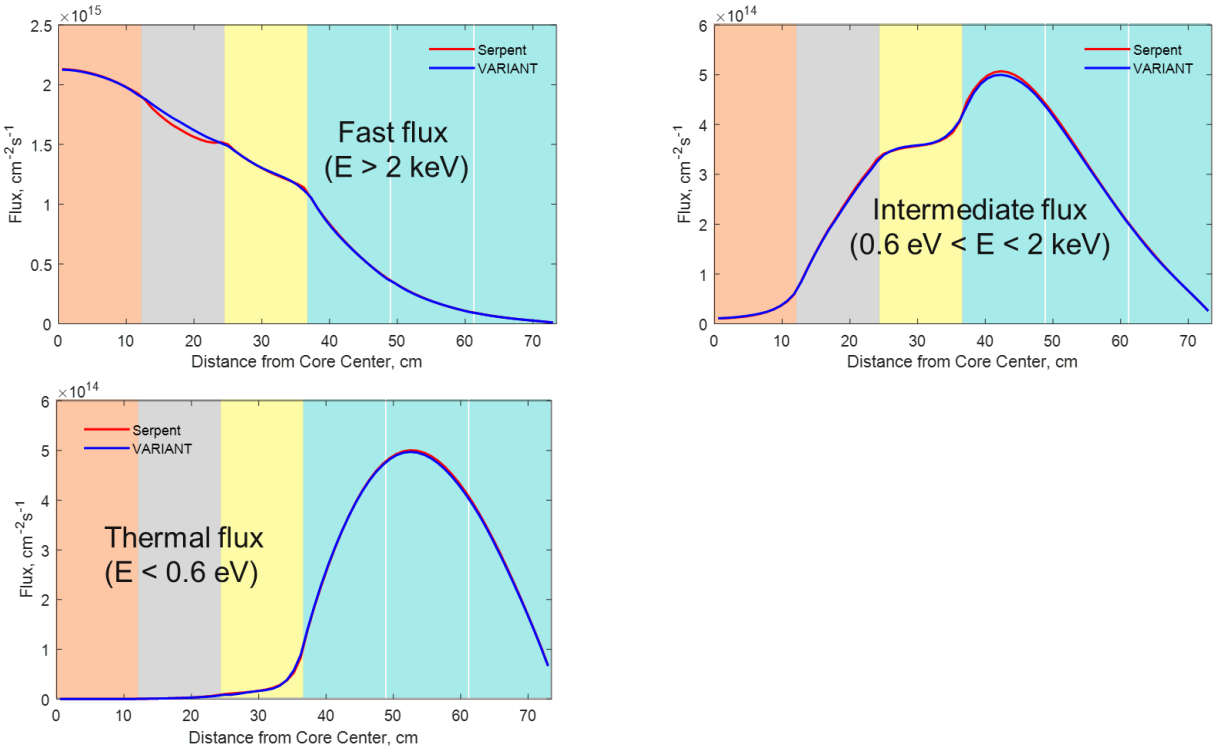

Figure 3.5 Comparison of Flux Profiles of Serpent and VARIANT 32G Transport Solutions

As shown in Table 3.1, the scalar flux weighted anisotropic scattering cross sections caused large errors in core calculations. Thus, the high order scattering matrices produced by Serpent (or other common MC codes) are not reliable for transport analysis with explicit anisotropic scattering. Using the BGXSs directly generated by Serpent, the best we can do is applying the transport corrected P_0 (TCP_0) approximation, which requires transport cross sections, and modified isotropic self-scattering matrices. Transport cross sections are generated with the out-scatter approximation in Serpent and are deduced from total cross sections and scalar flux weighted P_1 scattering cross sections [88]:

$$\Sigma_{tr} \approx \Sigma_t - \Sigma_{s1} \tag{3.1}$$

where Σ_{s1} is the P_1 scattering cross section. As well known, the outflow approximation does not produce accurate transport cross sections. A method to generate current weighted transport cross section was developed in Serpent but is not available in the publicly released version used for this dissertation [93]. The cumulative migration method (CMM) [94] implemented in OpenMC and Serpent is another option. But the current implementations are limited to those cases when the entire problem domain with periodic or reflective boundary conditions is homogenized.

Table 3.2 compares several VARIANT solutions obtained with the 32G reference BGXSs and the same spatial expansion orders as that used for Table 3.1 results but different angular approximation and anisotropic scattering orders. With the flux moment weighted anisotropic scattering matrices (Mixed case), inclusion of P_2 or P_3 order anisotropic scattering could produce accurate transport solutions. Transport calculations with P_1 scattering approximation also yielded plausible results because of error cancellation. While the eigenvalue error was reduced but the assembly power errors were increased, compared to the results with higher scattering orders. In VARIANT, the transport calculation with TCP_0 approximation was performed by subtracting the

P_1 scattering cross sections from the scalar flux weighted total cross sections and the diagonal terms of P_0 (isotropic) scattering matrices and considering only P_0 scattering. With the P_1 scattering matrices from MC^2-3 (Mixed case), it is seen that the TCP_0 approximation produced similar results as using explicit P_1 scattering order. With the P_1 scattering matrices from Serpent, the TCP_0 approximation led to significant errors in eigenvalue and power distribution as expected.

Table 3.2 Impact of angular approximation and scattering orders on VARIANT results

Angular approximation	Scattering cross section	Scattering order	Δk, pcm	Assembly power error	
				FA	TA
P_5 expansion	Mixed [(a)]	P_3	48	-0.03%	0.03%
		P_2	69	-0.02%	0.02%
		P_1	-28	-0.07%	0.06%
		TCP_0	6	0.11%	-0.10%
	Serpent	TCP_0	438	1.77%	-1.65%
P_1 expansion	Mixed	P_1	-536	-0.71%	0.67%
		P_0[(b)]	-119	0.81%	-0.71%

Notes:
(a) Combined isotropic scattering matrix of Serpent and anisotropic scattering matrices of MC^2-3.
(b) Used transport cross section and isotropic scattering matrix directly from Serpent. The diagonal terms of scattering matrix were not modified.

For diffusion (P_1 expansion) calculations, however, the inclusion of explicit P_1 anisotropic scattering resulted in larger errors than the case considering only P_0 scattering, for which the isotropic scattering matrices from Serpent were used without modifying the diagonal terms. Compared to the transport solution, using the same P_1 scattering matrices in diffusion resulted in a much worse solution, which implies significant transport effects. Assuming isotropic scattering (P_0 case), the diffusion solution had a much smaller eigenvalue error because of error cancellation as the assembly power errors were not reduced. The results in Table 3.2 illustrate that both transport effects and scattering anisotropy are significant in coupled-spectrum reactors and should be treated simultaneously for reliable core calculations.

3.2.1.2 Core Calculation with BGXSs Generated with Legacy Methods

The above analyses have been based on calculations performed using the reference cross sections. Realistic analyses usually rely on multigroup cross sections generated in simplified models, in which case group condensation errors are introduced by using a weighting spectrum deviating from the reference solution. Specifically, MC^2-3 was used to generate BGXSs for the homogenized CFTR-1D problem in two steps. Infinite medium slowing down calculations were first performed for each type of assembly to prepare ultrafine-group (989 groups) cross sections. Subsequently, a 989G transport calculation was performed with the TWODANT S_N code [75] in the Cartesian full-core model. Angular quadrature order of 12, P_3 anisotropic scattering approximation were used in two TWODANT calculations with different mesh sizes. Assembly dependent BGXSs were then obtained by condensing the 989G cross sections using the flux moment spectra of TWODANT solutions.

Table 3.3 summarizes the corresponding VARIANT broad-group transport calculation results using these BGXSs. To make consistent comparisons, the reference energy release per fission tallied in Serpent were applied in VARIANT calculations. It is seen that both 32G and 13G BGXSs generated in two-step MC^2-3/TWODANT calculations failed to reproduce the reference eigenvalue and assembly powers. The use of a finer mesh size in the TWODANT calculation did not make a noticeable difference.

Table 3.3 VARIANT transport solutions obtained with BGXSs prepared in two-step procedure

TWODANT mesh size	BGXSs for VARIANT calculation	Δk, pcm	Assembly power error	
			FA	TA
0.6 cm	ISOTXS.32G.mcc0D_twodant_0.6cm	274	-0.37%	0.35%
	ISOTXS.13G.mcc0D_twodant_0.6cm	305	-0.17%	0.15%
0.3 cm	ISOTXS.32G.mcc0D_twodant_0.3cm	275	-0.38%	0.35%
	ISOTXS.13G.mcc0D_twodant_0.3cm	306	-0.17%	0.16%

A direct comparison of 32G BGXSs as shown in Figure 3.6 revealed non-negligible errors in the macroscopic capture cross sections for fuel assemblies. The uncertainties of Serpent tallied cross sections were below 0.1% in most groups except for the low-energy (<100 eV) groups for the fast assembly, which was 0.2~0.3%. The 32G BGXSs have two error sources: inherited errors from the 989G cross sections and the use of inaccurate weighting spectra for group condensation. The weighting spectra is also affected by the errors in the 989G cross sections. For this simple 1D configuration, S_{12} angular approximation and P_3 anisotropic scattering order are considered sufficient to perform reliable transport calculations. The other important error source in TWODANT calculations is mesh size because TWODANT uses the finite difference method for spatial discretization. However, refining mesh size did not improve the spectrum solution as indicated by the results in Table 3.3 and the direct spectrum comparison in Figure 3.7, where the reference spectrum was obtained from a full-core 3483-group MOC calculation with MC^2-3. The self-shielded 3483-group cross sections used in the MOC calculation were generated from hyperfine-group fixed source calculations. Based on these observations, it seems that the broad-group cross section errors are mainly attributed to the errors in the UFG cross sections.

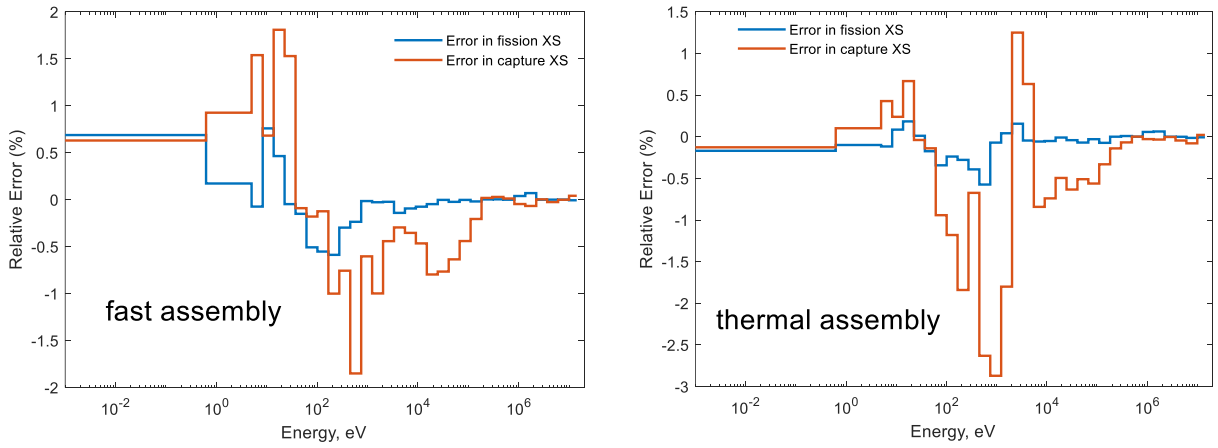

Figure 3.6 Relative Errors in 32G Macroscopic Cross Sections for Fast and Thermal Fuel Assemblies Generated in MC^2-3/TWODANT Calculations with 0.6 cm Mesh Size

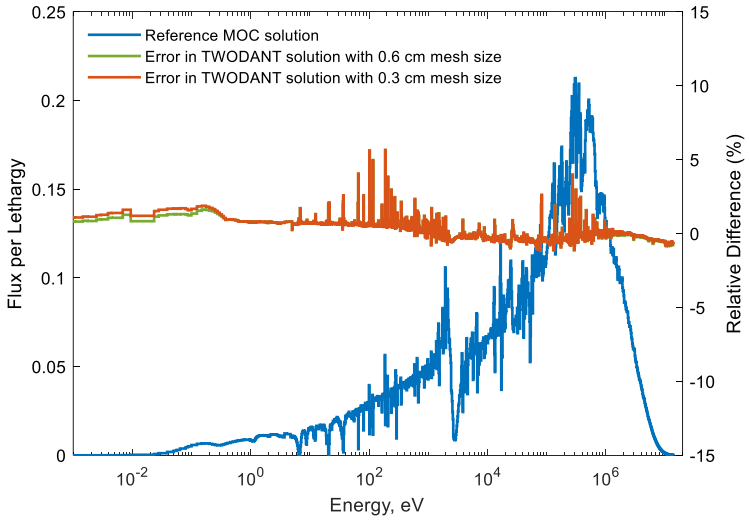

Figure 3.7 Comparison of 989G Spectrum in Thermal Assembly of TWODANT Solutions to Reference Solution of Full-core MOC Calculation

UFG cross sections are typically generated in assembly lattice calculations to consider resonance self-shielding and local heterogeneity effects. With about 1000 energy groups (default is 2082 groups in MC^2-3 for fast reactor analysis), the spectral transition effect on UFG cross sections is assumed relatively small. To quantify this effect, the UFG cross sections obtained in single assembly with reflective boundary conditions are compared to those generated in supercell models including neighboring assemblies. The supercell models used for this problem are illustrated in Figure 3.8. It is noted that a single graphite reflector (GR) with tripled atom density was used to approximately model the three reflectors in the original configuration. As the thermal assembly is highly under moderated, inclusion of graphite reflectors is essential to provide realistic moderation.

Figure 3.8 Illustration of Supercell Models for Fast (FA) and Thermal (TA) Fuel Assemblies

The UFG capture cross sections obtained with MC^2-3 in single-assembly and supercell models are compared in Figure 3.9. Clearly, the spectrum transition due to neighboring assemblies increased the UFG capture cross sections in fuel assemblies while fission cross sections were not significantly changed because the dominant resonance isotope U-238 does not have fission reaction in the resonance energy range. It explains why the broad-group fission cross sections had smaller errors than capture cross sections as shown in Figure 3.6. It is noted that the flux level below 1000 eV is negligible in fast reactors and hence the errors in UFG cross sections generated in assembly models as usually done with MC^2-3 should not make noticeable differences in fast reactor core calculations.

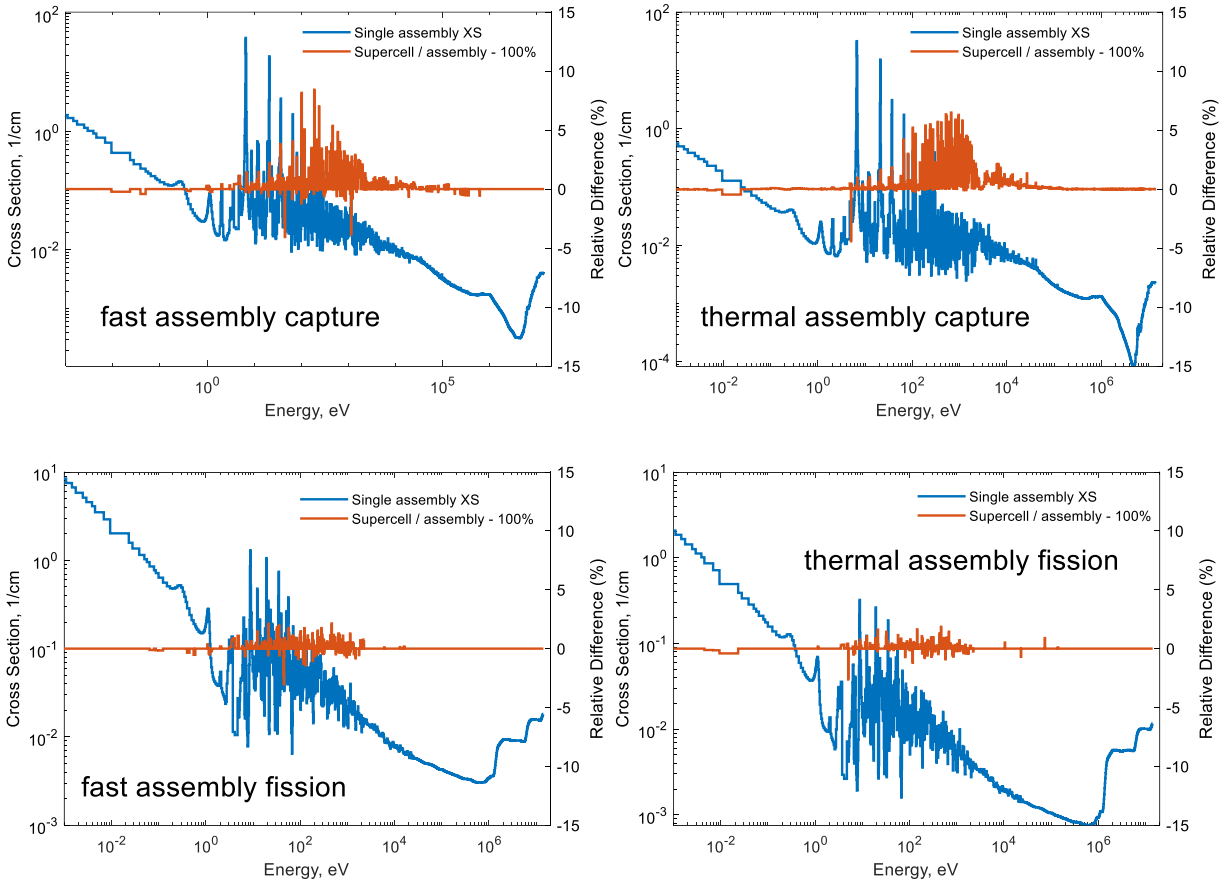

Figure 3.9 Comparison of UFG Cross Sections Generated in Assembly and Supercell Models

As shown in Figure 3.10, the spectral transition effect on thermal assembly cross section is well accommodated once supercell model is used. The few noticeable cross section error below 100 eV in the fast assembly is due to the neglect of thermal neutron source from the thermal assembly in the fast supercell model. It is also noted from Figure 3.11 that the environment impact becomes smaller when the fuel to moderator ratio decreases in the thermal assembly and the local spectrum is less affected by the external moderation in the graphite reflector. Another example is that the spectrum predicted in an assembly lattice calculation approaches the asymptotic spectrum in well moderated Light Water Reactors (LWRs) and hence few-group cross sections are typically generated in assembly lattice calculations.

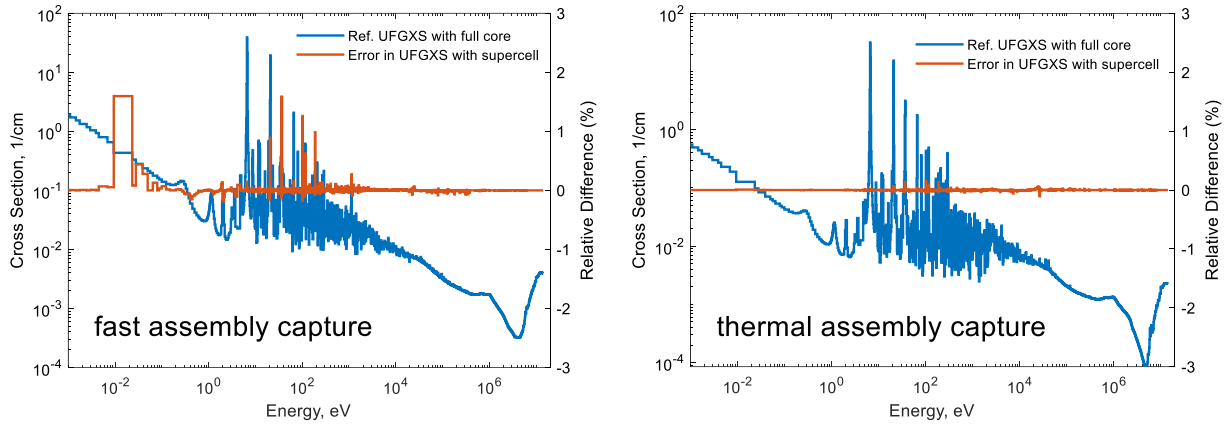

Figure 3.10 Comparison of UFG Cross Sections Generated in Supercell and Full-Core Models

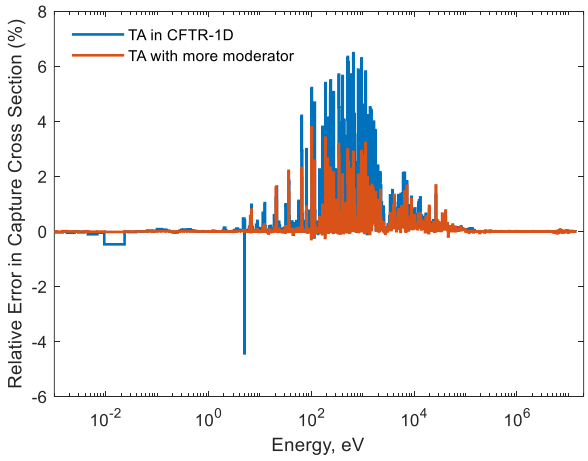

Figure 3.11 Deviations in UFG Cross Sections of Single-Assembly Model from Supercell for Thermal Assemblies with Different Fuel/Moderator Ratios

With supercell models to account for spectral transition effects, the only approximation is on the boundary condition, which is anticipated to have impacts on the local flux distribution and assembly homogenized cross sections. However, the exact knowledge of boundary conditions is as hard as to obtain the full-core solution. Before switching to approximated treatment of boundary conditions, the performance of supercell models was tested in broad-group cross section generation and core calculations. By replacing the single-assembly calculations with supercell calculations for UFG cross section generation in the MC^2-3/TWODANT calculation procedure, two sets of BGXSs were generated and their performances in VARIANT core calculations are compared with the BGXSs obtained without use of supercell models in Table 3.4.

Table 3.4 VARIANT transport solutions obtained with BGXSs generated using MC^2-3

MC^2-3 model	Broad group structure	Δk, pcm	Assembly power error	
			FA	TA
Single assembly & full core model	32G	274	-0.37%	0.35%
	13G	305	-0.17%	0.15%
Supercell & full core model	32G	146	0.30%	-0.28%
	13G	179	0.51%	-0.48%
Full core model	32G	181	0.31%	-0.29%

It is seen that the use of supercell model for UFG cross section preparation improved the predicted eigenvalue in core calculations. In fact, the two 32G cross section sets obtained respectively in the two-step procedure and in a direct full-core MC^2-3 calculation (the last case in Table 3.4) produced similar core calculation results. The remaining errors in VARIANT solutions are mainly due to the approximations in MC^2-3 to produce UFG cross sections. Uniform 3483-group cross sections were assumed for each assembly to perform MC^2-3 supercell and full-core MOC calculations in a practical time. Although assemblies are homogenized in the CFTR-1D problem and about 1000 groups are used for UFG cross sections, there exists cross section variation

within an assembly when it is next to a different type of assembly. Figure 3.12 shows the deviations in the assembly averaged UFG cross sections of MC^2-3 supercell calculation from Serpent supercell simulation. It should be noted that this error did not appear in the comparison of Figure 3.10 because the same approximation of uniform cross sections within each assembly was applied in both supercell and full-core MC^2-3 calculations.

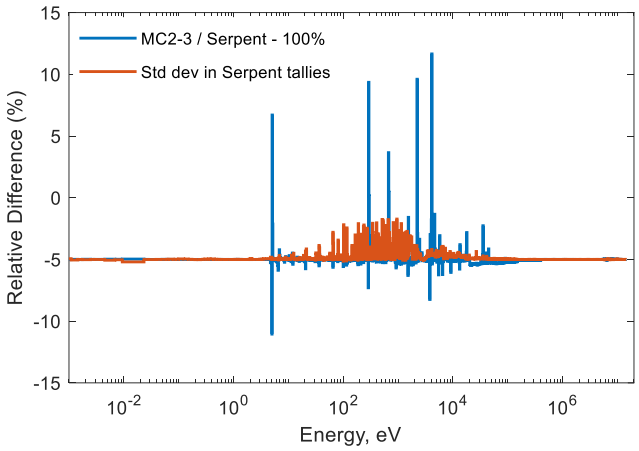

Figure 3.12 Deviations in UFG Thermal Assembly Capture Cross Sections of MC^2-3 Supercell MOC Calculation from Serpent Supercell Simulation

In principle, we can divide each assembly into smaller constant cross section zones to eliminate the spatial dependence. An alternative means is through continuous-energy Monte Carlo simulation, where the UFG cross sections are effective averages of space independent pointwise cross sections. For clarification, another set of UFG cross sections were generated in Serpent supercell calculations and used in TWODANT calculations (anisotropic scattering cross sections were replaced with MC^2-3 values). The condensed 32G cross sections were compared with those generated in MC^2-3 supercell and TWODANT full-core calculations in Figure 3.13. It is shown that the errors in supercell UFG cross sections did make a considerable difference in the resultant broad-group cross sections.

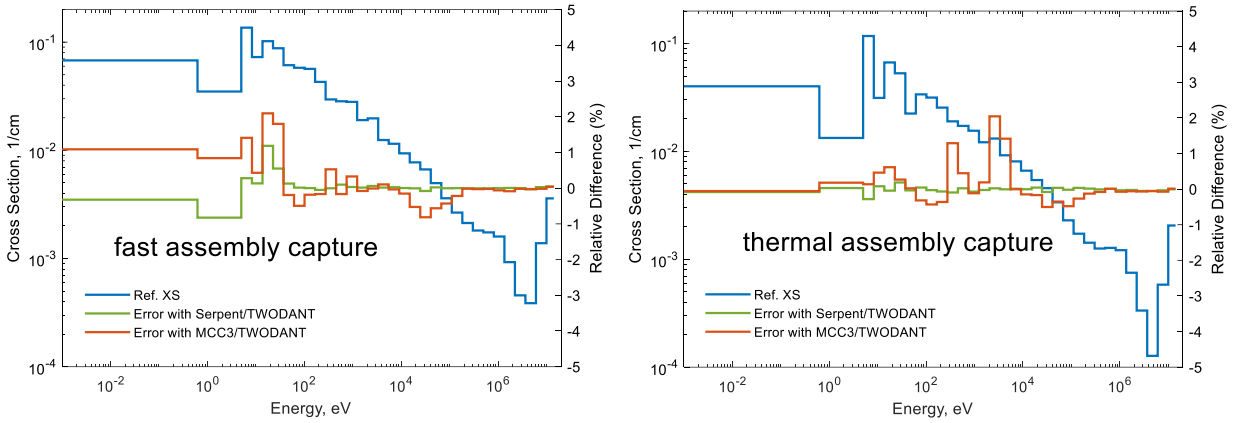

Figure 3.13 Errors in 32G Capture Cross Sections Condensed from UFG Cross Sections Obtained in Serpent or MC^2-3 Supercell Calculations

3.2.2 Heterogeneous CFTR-1D Problem

For the heterogeneous CFTR-1D problem, the reference BGXSs (13G) were tallied in Serpent full-core simulation for each assembly. Direct use of Serpent cross sections in VARIANT nodal transport calculation would not produce accurate solutions, as shown in Table 3.5. One error source is the scalar flux weighted anisotropic scattering cross sections as discussed in Section 3.2.1. Flux moment weighted anisotropic scattering matrices were prepared separately using MC^2-3 with both homogenized and heterogeneous full-core models. Replacement of Serpent anisotropic scattering matrices with MC^2-3 values for the homogeneous and heterogeneous models resulted in two mixed cross section sets, which are labeled "_mixedA" and "_mixedB", respectively.

Table 3.5 Eigenvalue and assembly power errors of VARIANT transport solutions using reference broad-group cross sections for heterogeneous CFTR-1D problem

Code	Cross section	k_{eff}	Std dev / Error	Assembly power error	
				FA	TA
Serpent	ENDF/B VII.0	1.13549	0.00004	–	–
VARIANT	ISOTXS.13G.core_serp	1.13830	0.00281	2.05%	-1.79%
	ISOTXS.13G.core_serp_mixedA	1.13358	-0.00191	0.16%	-0.14%
	ISOTXS.13G.core_serp_mixedB	1.13343	-0.00206	0.03%	-0.02%

It is seen from Table 3.5 that the two mixed cross section sets yielded similar results for this specific problem. It may indicate that the anisotropic scattering cross sections could be approximately generated with homogenized models. The other major error source is assembly homogenization. Even if the homogenized cross sections are weighted with the flux obtained in the heterogeneous full-core calculation, additional equivalence parameters are needed to simultaneously preserve both average reaction rates and net leakage [51]. For VARIANT nodal transport calculations, a partial current based discontinuity factor (PCDF) was developed to better fit the red-black iteration scheme for the response matrix formulation of the even-parity transport equation. Detailed derivation of PCDF and its implementation in VARIANT will be presented in Chapter 4. Here we just apply it to the CFTR-1D problem to exemplify the limitation in the current VARIANT method.

Table 3.6 presents the VARIANT core calculation results obtained with the reference BGXSs and PCDFs. For transport (P_5) calculations considering explicit anisotropic scattering, the anisotropic scattering matrices were generated with MC^2-3 for the heterogeneous core model. PCDFs were generated using the reference flux and surface partial currents tallied in the Serpent heterogeneous core calculation. It is seen that VARIANT calculations with PCDFs reproduce the reference heterogeneous solution in terms of eigenvalue and average assembly powers, regardless of the cross section set or transport approximation used in the homogenized calculation. Figure 3.14 compares the spatial flux distributions of VARIANT homogenized calculations to those of reference heterogeneous simulation results with Serpent. The VARIANT flux profiles match the reference profile except at fuel pin positions in the thermal assembly. Flux form functions are needed to represent these local heterogeneities. The thermal flux is not shown here because it is insignificant outside the reflector region, and it is also reproduced just as the higher energy fluxes.

Table 3.6 VARIANT solutions obtained with reference BGXSs and PCDFs

Cross section set	Angular expansion /Scattering orders	Δk, pcm	Assembly power error	
			FA	TA
ISOTXS.13G.core_serp	P_5 / P_3	-1	0.01%	-0.01%
	P_1 / P_0	3	0.00%	0.00%
ISOTXS.13G.core_serp_mixedB	P_5 / P_3	-1	0.01%	-0.01%
	P_1 / P_0	2	0.00%	0.00%

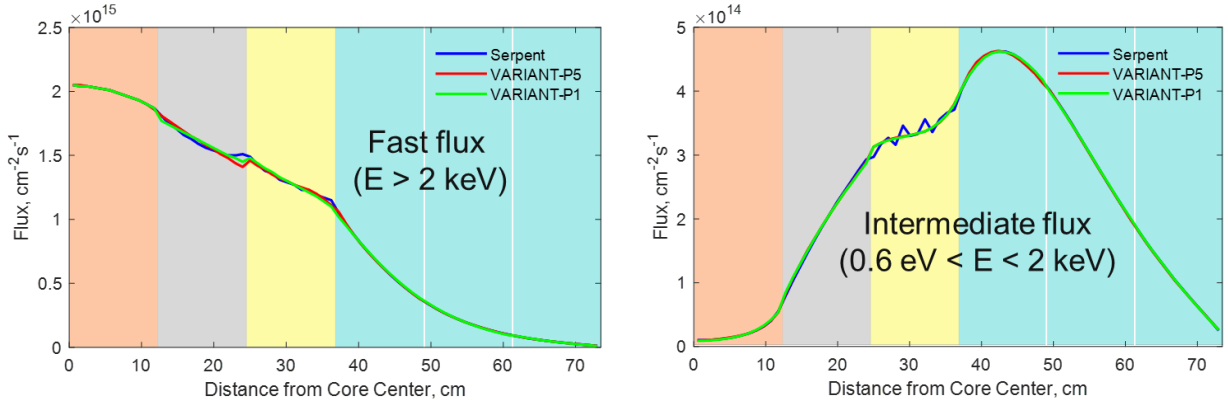

Figure 3.14 VARIANT Flux Profiles Obtained with Reference Serpent XSs and PCDFs in Heterogeneous CFTR-1D Core

The above tests indicate that assembly homogenization error is non-negligible in the coupled fast-thermal reactor. In Section 3.2.1, it is shown that accurate BGXSs for coupled reactor analyses can be obtained in supercell calculations with proper leakage corrections. However, discontinuity factor is expected to be more sensitive to the boundary condition of supercell models. The problem is how to generate satisfactory PCDFs in local calculations without relying on the full-core reference solution.

3.3 Whole-Core Depletion Calculation

There are three major error sources in depletion calculations: approximations applied in Bateman equation solver, simplifications in depletion chain, approximations adopted in transport calculation for flux solution. In this section, the REBUS-3 code was examined in all aspects using

simple depletion problems to highlight its main deficiency for coupled-spectrum reactor analyses. First, the current Bateman equation solver of REBUS-3 was compared to alternative solvers for homogeneous depletion calculations to ensure its accuracy and applicability to model more detailed depletion chains for thermal spectrum depletion problems. Then, a simplified depletion chain was tested with REBUS-3 for thermal depletion calculations. The impacts of multiple simplifications of depletion chain were discussed as well. At last, full-core depletion calculations were performed for the CFTR-1D core problem for integral test of the VARIANT/REBUS-3 core calculation procedure. The reference depletion solutions were obtained with Serpent burnup calculations. For REBUS-3 depletion calculations, microscopic cross sections were generated with the OpenMC Monte Carlo code of version 0.12.0, which is released with HDF5 cross section libraries generated from ENDF/B-VII.1. To be consistent, both Serpent and OpenMC used nuclear data from the ENDF/B-VII.1 library.

3.3.1 Bateman Equation Solver

The Bateman equation can be simply put as:

$$\frac{d}{dt}\vec{N}(t) = \mathbf{A}(\phi, \sigma, \lambda, \gamma, t)\vec{N}(t) \tag{3.2}$$

where $\vec{N}(t)$ is the time dependent nuclide density vector, **A** is the depletion transmutation rate matrix (burn matrix) depending on flux (ϕ), microscopic cross section (σ), decay constant (λ), and reaction branching ratio (γ). The time dependency of burn matrix is due to the time dependency of flux and cross sections. Perhaps the predictor-corrector method is the most widely used approach for time discretization of Eq. (3.2). REBUS-3 employs the predictor-corrector method along with region density iteration. The end-of-step nuclide densities are iteratively determined in multiple corrector steps until they converge within a user-specified tolerance [73]. Recently,

predictor-corrector methods involving high-order extrapolation/interpolation have been developed for burnup calculations based on Monte Carlo so that the longer time steps can be used to reduce the required number of costly Monte Carlo simulations [98-100]. Nevertheless, since the flux solution is obtained in efficient nodal calculations and the region density iteration method allows to use large time steps without loss of accuracy, it is not imperative to modify the current predictor-corrector algorithm of REBUS-3 for potential efficiency improvement.

With a constant burn matrix $\bar{\mathbf{A}}$ representing the average nuclide transmutation rates in a discretized time interval Δt, a formal solution to the discretized Eq. (3.2) can be written as:

$$\vec{N}(t + \Delta t) = exp[\bar{\mathbf{A}}\Delta t]\,\vec{N}(t). \tag{3.3}$$

Eq. (3.3) involves the evaluation of matrix exponential $exp[\bar{\mathbf{A}}\Delta t]$. There exist dozens of methods obtained from classical results in analysis, approximation theory, and matrix theory [101,102]. Among these methods, series expansion methods with scaling and squaring algorithm are efficient and easy to implement and hence are widely adopted. REBUS-3 employs the Taylor series expansion method with scaling and squaring algorithm, which works very well for fast reactor depletion calculation [103] because the burn matrix for fast reactor fuel cycle analysis is relatively small, and the equation stiffness is reduced by removing those short-lived fission products from depletion chain, assuming they are transmuted immediately. This approximation is acceptable in fast reactor analysis since the impact of fission products on neutronics properties is small and the short-term phenomenon is out of interest in fuel cycle analysis. However, in thermal spectrum systems, the large absorption cross sections of many fission products lead to a pronounced perturbation of the neutronics characteristics of the core. Build-up of fission products must be properly modeled to predict the reactivity level accurately. In this case, important fission products such as xenon and samarium, and burnable absorbers such as gadolinium and erbium, need to be

modeled explicitly, which poses a greater stiffness onto the system of depletion equations because of their large decay and/or large disintegration rates.

When the matrix norm is large, an unfavorably short time step and a large scaling and squaring order are required. Matrix squaring is not cheap and accumulated round-off errors in continuous squaring will lead to large numerical errors. Recently, alternative methods dedicated to nuclear depletion problems were developed for detailed depletion calculations with complicated burn chains of thousands of nuclides including very short-lived nuclides with half-life less than a second [104-107]. Refs. [105] and [107] compared the series expansion method with Padé approximation, the Chebyshev rational approximation method (CRAM), and the Krylov subspace method for computing the exponential of a large burn matrix. Compared to the reference solution obtained with the transmutation trajectory analysis [108], the CRAM method outperforms the other methods with better accuracy and efficiency. The implementation of CRAM method in the Serpent code eliminates the need of special treatment of short-lived nuclides. In this circumstance, a natural question is whether REBUS-3 needs to be modified to use the CRAM method as well for thermal system depletion.

The current REBUS-3 algorithm for the matrix exponential solution is first tested with a manufactured small depletion problem. This problem contains only five nuclides: U-235, I-135, Xe-135, Cs-135, and a pseudo nuclide DUMP. Only fission reaction of U-235 and capture reaction of I-135, Xe-135, and Cs-135 are considered, respectively. The pseudo nuclide is assumed to have no reactions. The decay chain considered here is as shown in Figure 3.15. The initial number density, one-group cross section, and decay constant of each isotope, and fission yields of fission products are given in Table 3.7. A constant flux of 2×10^{14} n/cm^{2}s is assumed for depletion. This simple test problem is made to mimic the thermal system burn matrix with large decay and

disintegration rate terms for fission products and a widespread eigenvalue spectrum. For this simple problem with linear chains, an analytical reference solution was obtained by direct integration of the original differential equations. Using the TDECAY subroutine of REBUS-3, the nuclide densities after one-step depletion are calculated and compared to the reference results. The scaling and squaring algorithm with Padé approximation implemented in the *expm* function of MATLAB [109] and the CRAM method (of 14th order) implemented in EXPOKIT [110] are also compared for this problem.

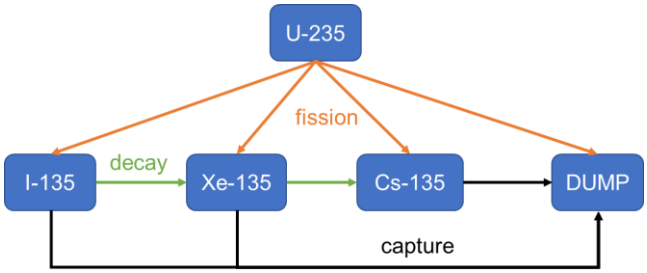

Figure 3.15 Simplified Depletion Chain for Five-Nuclide Test Problem

Table 3.7 Setup of five-nuclide depletion test

Isotope	Initial Density, 1/barn-cm	Fission cross section, barn	Capture cross section, barn	Decay constant, 1/s	Fission yield
U-235	0.02	5.00E+02	-	-	-
I-135	0.00	-	1.00E+02	2.92E-05	0.6
Xe-135	0.00	-	3.00E+06	2.11E-05	0.3
Cs-135	0.00	-	1.00E+01	0.00E+00	0.1
DUMP	0.00	-	-	stable	1.0

Different time intervals spanning from 0.01 to 1000 days were used in the test. The maximum time interval of 1000 day is impractically large for normal depletion calculation and is used to test the robustness of algorithms. The reference nuclide densities of the analytical solution are presented in Table 3.8. The corresponding maximum absolute relative errors of different methods are summarized in Table 3.9. In REBUS-3, the Taylor series is truncated when the infinity norm of the last expansion term is less than 10^{-8}. Table 3.10 shows that refined truncation criteria

(TC) for Taylor expansion provide very marginal improvement of the nuclide density results. This is because of the numeric round-off errors in finite precision arithmetic and more importantly in the repeated squaring of the scaled matrix exponential. Over-scaling of the original matrix sometimes deteriorates the accuracy in addition to the computational efficiency. In MATLAB, the scaling order is carefully selected to avoid over-scaling [109]. From the comparison, all the three algorithms yield sufficiently accurate results for this small matrix exponential problem. The series method with Padé expansion in MATLAB produced even better solutions than the arising CRAM method.

Table 3.8 Reference nuclide densities (1/barn-cm) of five-nuclide test problem

Time interval, day	0.01	0.1	1	10	100	1000
U-235	1.9998E-02	1.9983E-02	1.9828E-02	1.8345E-02	8.4295E-03	3.5377E-06
I-135	1.0238E-06	9.1586E-06	3.7554E-05	3.7798E-05	1.7368E-05	7.2893E-09
Xe-135	4.1208E-07	1.3179E-06	2.7161E-06	2.6635E-06	1.2239E-06	5.1365E-10
Cs-135	1.7684E-07	1.8994E-06	2.1095E-05	2.1458E-04	1.4952E-03	2.2412E-03
DUMP	1.8431E-06	2.2169E-05	2.8275E-04	3.0559E-03	2.1627E-02	3.7752E-02

Table 3.9 Maximum absolute relative errors in nuclide densities of different methods

Time interval, day	0.01	0.1	1	10	100	1000
REBUS-3 (Taylor)	2.93E-10	1.27E-11	4.34E-13	3.33E-15	0.00E+00	8.75E-13
MATLAB (Padé)	9.77E-15	7.77E-15	0.00E+00	1.09E-14	7.48E-14	1.13E-12
EXPOKIT (CRAM)	8.38E-12	8.49E-12	7.57E-12	5.44E-12	5.63E-12	9.53E-09

Table 3.10 Maximum relative errors in rebus-3 results with different truncation criteria

Time interval, day	0.01	0.1	1	10	100	1000
TC = 10^{-8}	2.93E-10	1.27E-11	4.34E-13	3.33E-15	0.00E+00	8.75E-13
TC = 10^{-12}	2.91E-10	1.24E-11	4.34E-13	3.33E-15	0.00E+00	8.75E-13
TC = 10^{-15}	2.91E-10	1.24E-11	4.34E-13	3.33E-15	0.00E+00	8.75E-13

The REBUS-3 algorithm for computing matrix exponential was further tested for a more realistic, homogenized pin-cell depletion problem. The pin cell configuration and the homogenized composition with fresh fuel is given in Table 3.11. A simplified depletion chain was developed to explicitly track 29 actinides, 151 fission products, and three dummy isotopes used to truncate depletion chains. Construction of this depletion chain is discussed later in Section 3.3.2, along with other considerations of the REBUS-3 depletion model.

Table 3.11 Configuration of pin cell depletion problem

Fuel form (enrichment)	UO_2 (3.0 wt. %)
Fuel pellet radius, cm	0.4125
Cladding thickness, cm	0.0625
Pin pitch, cm	1.26
Fission power level, kW/m	35.0
Initial homogenized composition:	
Isotope	Number density, 1/barn-cm
U235	2.35126E-04
U238	7.50639E-03
O16	3.39916E-02
H1	3.70174E-02
Al27	6.61413E-03

The burn matrix generated by REBUS-3 at BOC was extracted to test the matrix exponential solver for computing the nuclide densities after one-step depletion of 1, 10, and 100 days. The reference solution was obtained using the *MatrixExp* function of the Wolfram Mathematica 13.0 software [111]. *MatrixExp* can compute the matrix exponential to an arbitrary precision, depending on the matrix characteristics. To get an exact reference solution, the matrix exponential was calculated with the matrix decomposition option. Specifically, either Jordan decomposition or the Putzer's method [112] is used to evaluate the matrix exponential analytically. For a matrix of Jordan canonical form, the matrix exponential is composed of only a finite number of terms of matrix powers.

Table 3.12 compares the performances of the three tested algorithms for computing matrix exponential in terms of accuracy and efficiency. The REBUS-3 implementation of the Taylor series method in the TDECAY subroutine was adopted in a Fortran test program. The EXPOKIT implementation of the14th order CRAM method (written in MATLAB script) and the built-in *expm* function of MATLAB were directly used for the test. For a middle-size burn matrix consisting of 183 nuclides, the scaling and squaring methods with Taylor expansion or Padé approximation produced more accurate results than the CRAM method, while CRAM shows better efficiency than the scaling and squaring method with Taylor expansion in REBUS-3.

Table 3.12 Comparison of REBUS-3, MATLAB, and EXPOKIT for pin-cell depletion

	Time interval, day	1	10	100
Maximum Absolute Relative Error in Nuclide Density	REBUS-3 (Taylor)	3.42E-11	4.65E-13	5.42E-13
	MATLAB (Padé)	9.99E-15	6.32E-14	5.28E-13
	MATLAB (Taylor)	1.07E-14	1.40E-13	6.27E-13
	EXPOKIT (CRAM)	1.12E-03	4.97E-04	3.62E-05
Computational Time, Second	REBUS-3 (Taylor)	0.0188	0.0231	0.0283
	MATLAB (Padé)	0.0023	0.0026	0.0027
	MATLAB (Taylor)	0.0059	0.0059	0.0061
	EXPOKIT (CRAM)	0.0035	0.0035	0.0035

The timing of each algorithm was performed by executing the same calculation 100 times and taking the average CPU time. It must be noted that the REBUS-3 implementation of Taylor series method also evaluates the interval averaged matrix exponential for edits of burnup, breeding ratio, etc. For consistent comparisons, a MATLAB implementation of the Taylor series method only for matrix exponential evaluation was tested as well. It turns out that efficiencies of all the three algorithms are not sensitive to the norm of medium size burn matrix, whereas the additional operations in REBUS-3 implementation cause a logarithmical increase of time cost with increasing

time step size. Despite of this, the REBUS-3 method is reasonably efficient for routine depletion calculations with assembly homogenized core models. At each step, fuel depletion calculations for ~300 fuel assemblies with 10 axial zones in each assembly will take about one minute.

Figure 3.16 and Figure 3.17 show the absolute relative differences in the nuclide densities of modeled fission products and actinides after 100-day depletion of the pin cell, respectively. It is seen that REBUS-3 and MATLAB methods predicted consistently more accurate results than the CRAM method. A test calculation in Ref. [105] shows that the scaling and squaring expansion method with Padé approximation has numeric instability issue and predicts unphysical nuclide densities with a detailed depletion chain including over 1500 nuclides. It is expected that the REBUS-3 method would face similar problem when applied to huge burn matrices, which are usually seen in lattice physics calculation with depletion rather than in nodal core calculations. In the whole core depletion calculations for fuel cycle analyses, simplified depletion chains are used, and the size of burn matrix is limited. Under this circumstance, the above comparison indicates no urgent need to modify the current REBUS-3 code for matrix exponential computation.

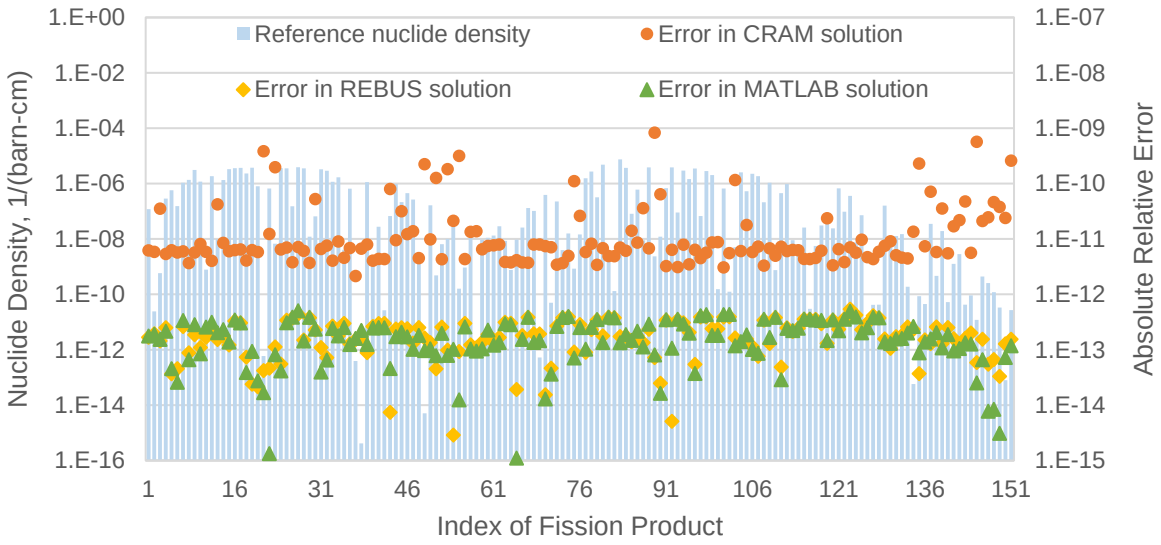

Figure 3.16 Comparison of Fission Product Densities after 100-day Pin-cell Depletion

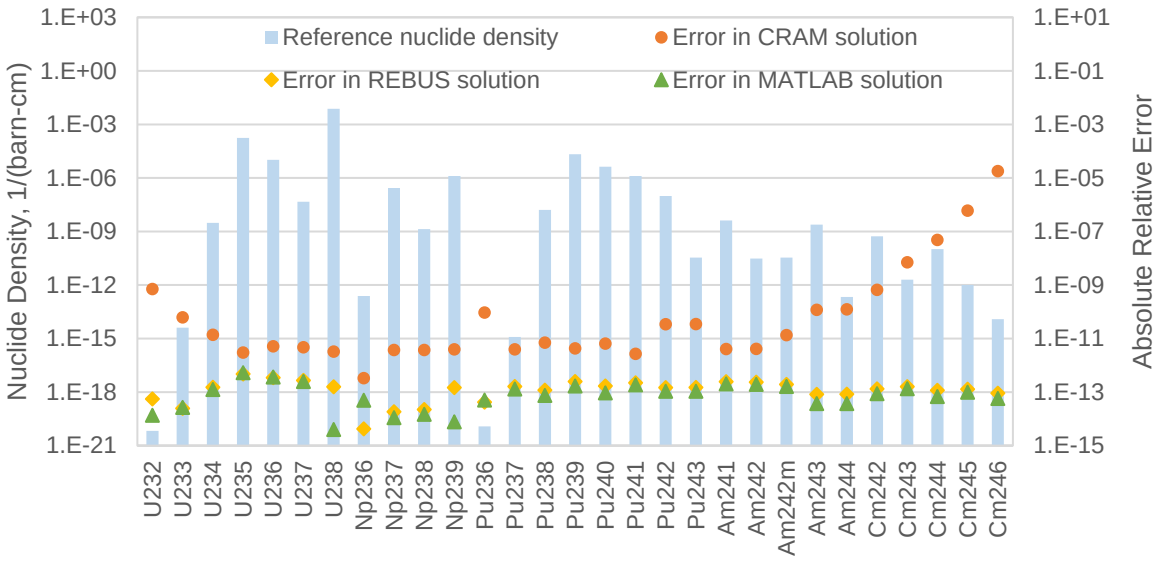

Figure 3.17 Comparison of Actinide Densities after 100-day Pin-cell Depletion

3.3.2 Depletion Chain

Depending on the final goal of depletion calculations, nuclide transmutation and decay are modeled in different levels of details. A detailed burnup chain may include thousands of nuclides for source term evaluations while only a few hundred (less than 500) important nuclides are needed in reactivity and power calculations. In fuel cycle analyses of fast reactors, the size of burn matrix is further reduced to less than 100 by utilizing lumped fission product models. In thermal reactor analyses, fission products with large thermal absorption cross sections should be explicitly traced. The Generalized Perturbation Theory [113-115] provides a practical approach to identify the important fission product isotopes to be explicitly modeled. In Ref. [115], a simplified 464-nuclide chain was developed for LWR lattice depletion calculations. Using the simplified chain, the effective neutron multiplication factor could be accurately predicted within 10 pcm deviation for burnup up to 80 MWD/kg. The depletion chain for core calculations can be further simplified to include about 200 nuclides only [114]. A simpler depletion chain is beneficial to saving memory usage, computational time, and the efforts to generate isotopic cross sections. In this thesis work,

isotopic cross section generation heavily relies on Monte Carlo simulation. The computational resource spent on cross section tallies is proportional to the number of tracked nuclides.

For the targeted solid uranium or plutonium fueled coupled-spectrum reactors, a burn chain was developed based on the simplified depletion chain library of OpenMC version 0.12.0, by removing thorium and protactinium nuclides and a few short-lived fission products with half-life less than 0.01 days, and truncating fission product activation at Ho-165. The OpenMC chain library is built with chain nuclides included in the VERA depletion benchmark suite [116]. The further simplified chain contains 29 actinides, 151 fission product or activation nuclides, and three dummy isotopes for chain truncation. A full list of these nuclides is provided in Table 3.13.

Table 3.13 Nuclides included in the simplified depletion chain for REBUS-3 calculation

Heavy metals		U232, U233, U234, U235, U236, U237, U238, Np236, Np237, Np238, Np239, Pu236, Pu237, Pu238, Pu239, Pu240, Pu241, Pu242, Pu243, Am241, Am242, Am242m, Am243, Am244, Cm242, Cm243, Cm244, Cm245, Cm246
Fission or activation products	w/ cross section	Br81, Kr82, Kr83, Kr84, Kr85, Kr86, Sr89, Sr90, Y89, Y90, Y91, Zr90, Zr91, Zr92, Zr93, Zr94, Zr95, Zr96, Nb95, Mo94, Mo95, Mo96, Mo97, Mo98, Mo99, Mo100, Tc99, Ru100, Ru101, Ru102, Ru103, Ru104, Ru105, Ru106, Rh103, Rh105, Pd104, Pd105, Pd106, Pd107, Pd108, Ag107, Ag109, Ag110m, Ag111, Cd110, Cd111, Cd112, Cd113, Cd114, In115, Sb121, Sb123, Sb125, Te127m, Te129m, Te132, I127, I129, I130, I131, I135, Xe128, Xe130, Xe131, Xe132, Xe133, Xe134, Xe135, Xe136, Cs133, Cs134, Cs135, Cs136, Cs137, Ba134, Ba137, Ba140, La139, La140, Ce140, Ce141, Ce142, Ce143, Ce144, Pr141, Pr142, Pr143, Nd142, Nd143, Nd144, Nd145, Nd146, Nd147, Nd148, Nd150, Pm147, Pm148, Pm148m, Pm149, Pm151, Sm147, Sm148, Sm149, Sm150, Sm151, Sm152, Sm153, Sm154, Eu151, Eu152, Eu153, Eu154, Eu155, Eu156, Eu157, Gd152, Gd154, Gd155, Gd156, Gd157, Gd158, Gd160, Tb159, Tb160, Dy160, Dy161, Dy162, Dy163, Dy164, Ho165
	w/o cross section	Br82, Tc99m, Rh102, Rh102m, Rh103m, Rh106m, Pd109, Cd115, Sb127, Te127, I128, I132, Xe135m, Pr144, Nd149, Pm150, Sm155, Gd159, Tb161, Dy165
Dummy isotopes		DUMP1, DUMP2, DUMFP

It is noted that 20 fission products or activation nuclides do not have neutron reaction cross sections in the ENDF library. They are interim nuclides with short half-life (greater than 0.01 days) and their decay daughter nuclides are explicitly traced. These nuclides are included with zero cross sections and used only in depletion calculations. The dummy isotopes DUMP1 and DUMP2 with zero cross sections are used to truncate transmutation chain of heavy nuclides. The dummy isotope DUMFP is used to represent fission products that are not explicitly tracked. DUMFP is assumed to have scattering reactions mainly and few absorption reactions, and hence is approximately treated as Mo92 in transport calculations.

To be used in REBUS-3, a python script was developed to convert the XML format library of OpenMC into type 09 and 25 input cards of the A.BURN dataset used by REBUS-3. In this procedure, the average energy of neutrons inducing fissions (AFE) is provided to interpolate the energy dependent fission yield data given in the OpenMC library because REBUS-3 only handles fixed yield data. The constant branching ratios (BRs) for producing metastable isomers in Serpent were adopted in the simplified burn chain for REBUS-3. The same set of BRs are also available in the chain library of OpenMC. These constant BRs are calculated from energy dependent values using typical PWR flux spectrum as:

$$\bar{\gamma} = \frac{\int_0^\infty \gamma(E)\sigma(E)\phi(E)dE}{\int_0^\infty \sigma(E)\phi(E)dE}, \tag{3.4}$$

where $\gamma(E)$ is the energy dependent branching ratio for specific isotope and reaction type and the other symbols are standard notations in reactor physics.

The simplified burn chain was tested using the homogenized thermal pin cell problem presented in Section 3.3.1. First, a reference Serpent depletion calculation was performed for a burnup of 40 MWD/kg with a detailed burn chain considering ~1200 nuclides. The burnup isotopic cross sections were tallied in a series of OpenMC simulations with the same material composition

from Serpent solution at each depletion step. Then, a REBUS-3 calculation was performed with the simplified burn chain and burnup dependent isotopic cross sections. As Serpent normalizes reaction rates to the total fission power, the isotopic fission Q-values (constant energy release per fission event) used in Serpent were extracted and applied in the REBUS-3 power calculation.

Figure 3.18 compares the k-infinity (k-inf) results of REBUS-3 depletion solution to the reference Monte Carlo solutions. The REBUS-3 solution was obtained with fission yields corresponding to the AFE at the middle of cycle and BRs collapsed with a typical PWR flux spectrum. The OpenMC results are from the steady-state calculations for isotopic cross section generation. The comparison shows good agreement between REBUS-3 and Serpent depletion solutions. The k-inf error is less than 40 pcm and is within 3σ uncertainty of Serpent results. The remaining errors should be mainly due to uncertainties in the tallied isotopic cross sections as the OpenMC calculation with the same compositions and nuclear data libraries showed comparable deviations from Serpent results.

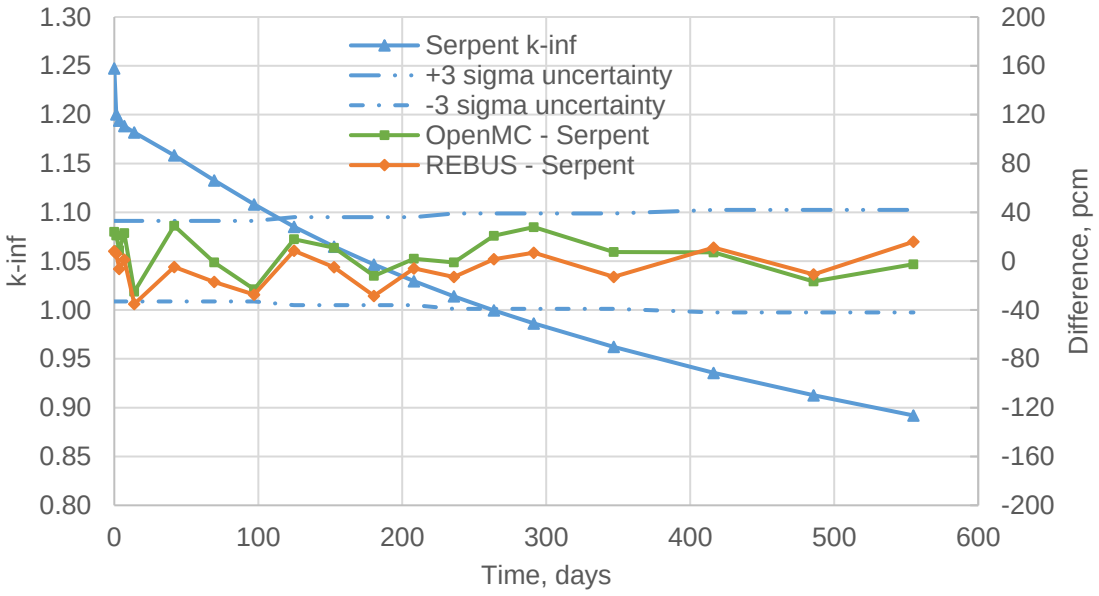

Figure 3.18 Eigenvalue Errors of REBUS-3 Depletion Solution with Simplified Burn Chain

Figure 3.19 shows the corresponding errors in the predicted end-of-cycle (EOC) number densities of heavy nuclides of the REBUS-3 depletion solution. It is shown that the fuel depletion can be accurately modeled with the simplified burn chain, with less than 1% difference in actinide number densities. As shown in Figure 3.20, the number densities of most fission products are also accurately predicted. A few nuclides show larger errors because of the simplification of burn chain. Since the primary goal is to catch reactivity and power change with fuel depletion, the test results confirmed the validity of the simplified burn chain.

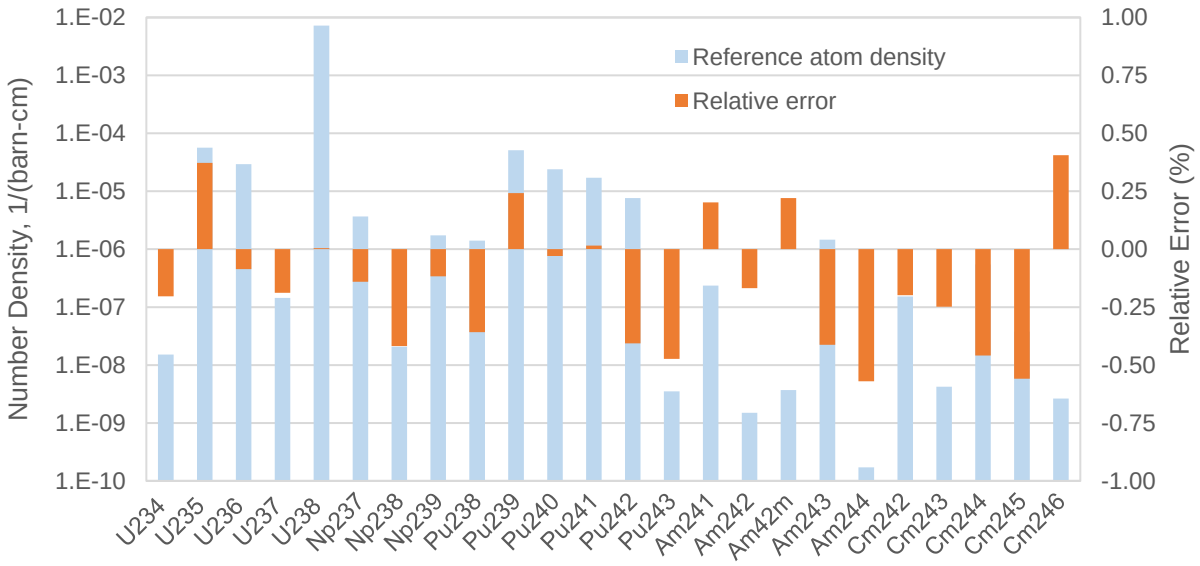

Figure 3.19 Errors in Heavy Nuclide Number Densities at EOC of REBUS-3 Depletion Solution with Simplified Burn Chain (Nuclides of number density < 10^{-10} $barn^{-1}cm^{-1}$ are not shown)

During fuel depletion, AFE changes because of spectrum shift, which results in different fission yield fractions. The impact of fission yields on depletion solution was investigated by choosing AFE at the beginning and middle of fuel cycle, and by setting AFE to 500 keV, which is a typical value in fast reactors. As aforementioned, in lack of the library of energy dependent branching ratios for neutron capture/absorption reactions, constant BRs collapsed with representative flux spectrum are used in common Monte Carlo codes. To quantify the impact of

different BRs under different spectra, a comparative REBUS-3 calculation was performed with the same simplified depletion chain, same middle-of-cycle AFE, but a different set of BRs given in the depletion chain library of OpenMC [117], which are calculated with a prototypical flux spectrum in sodium-cooled fast reactors (SFRs).

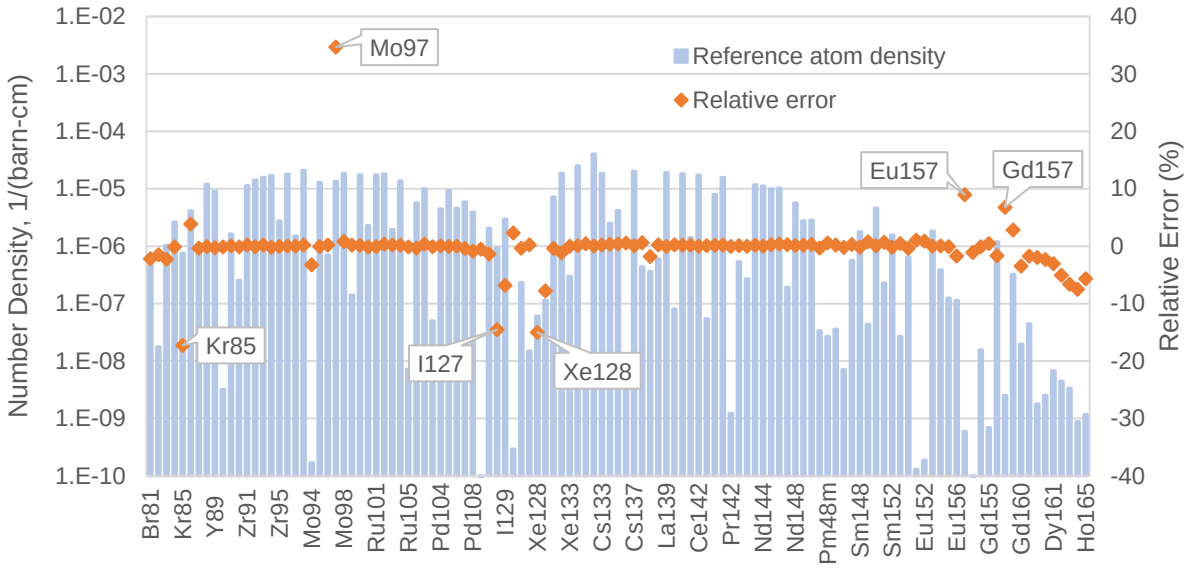

Figure 3.20 Errors in Fission Product Number Densities at EOC of REBUS-3 Depletion Solution with Simplified Burn Chain

Figure 3.21 compares the isomer production BRs weighted with PWR and SFR flux spectra. Those isotopes whose BRs are more sensitive to the weighting flux spectrum are highlighted. It is seen that most BRs are not sensitive to the weighting spectrum. In the simplified burn chain, where the two tungsten nuclides having distinct BRs are excluded, the biggest difference is in the Am241 capture BR to yield metastable Am241m. Figure 3.22 shows the k-inf difference caused by using different fission yield fractions (via AFE specification) and branching ratios in the depletion calculation. It is seen that for a thermal reactor, the spectrum change during depletion would not cause such a significant change in fission yield fractions that leads to noticeable change in reactivity. In fast spectrum systems, this effect would be even smaller because

of negligible absorption in fission products. However, the different yield fractions between fast and thermal spectrum systems made 50 pcm difference in k-inf. Thus, it is necessary to consider the spectrum dependent fission yields in coupled-spectrum reactors.

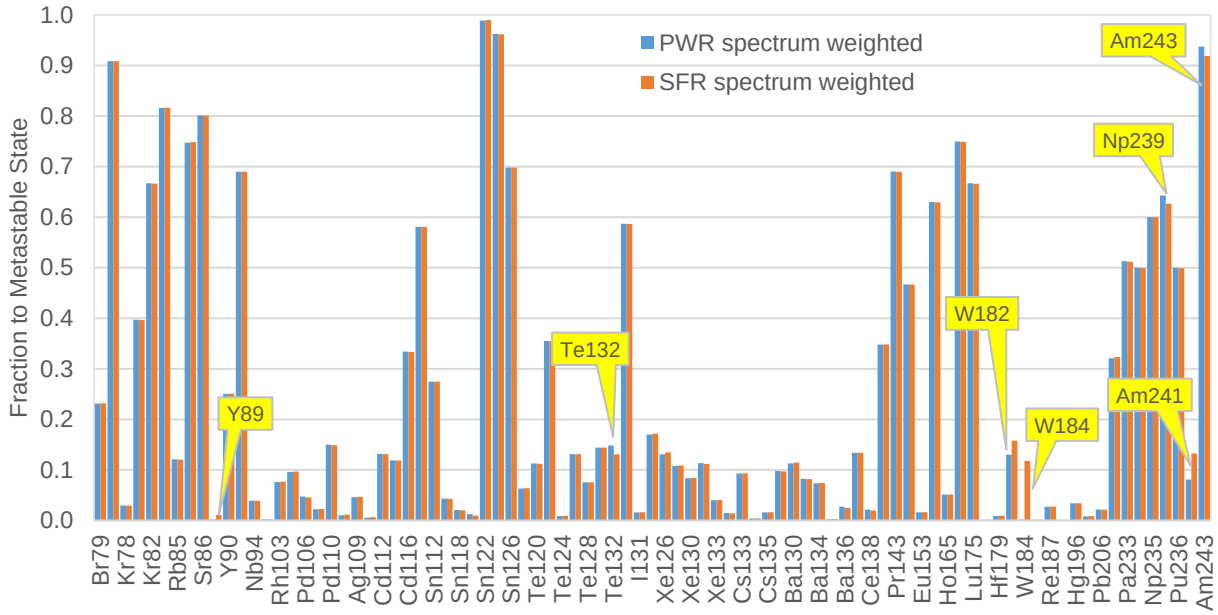

Figure 3.21 Comparison of Branching Ratios Weighted with PWR and SFR Flux Spectrum

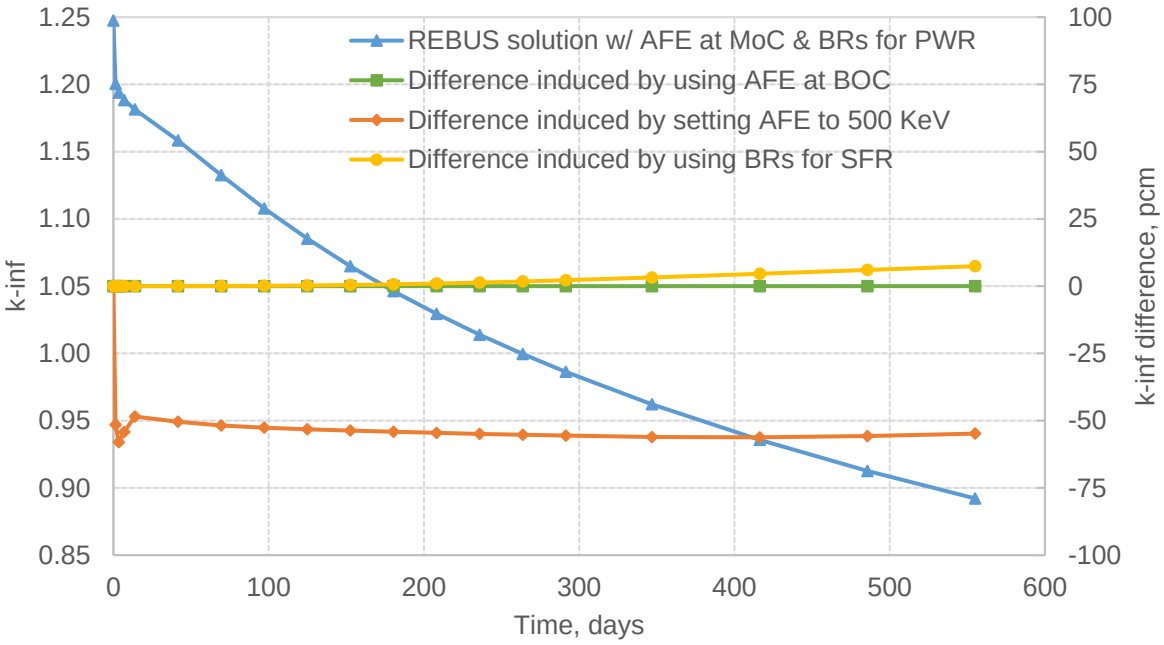

Figure 3.22 Impacts of Inaccurate Fission Yield Fractions and Branching Ratios

Figure 3.22 shows the impact of the neutron energy dependence of reaction branching ratios is marginal, as indicated by Figure 3.21, because the tested pin cell depletion started with fresh uranium fuel. With plutonium fuel, burned fuel, or recycled spent fuel, which easily breeds or contains more americium, incorrect BRs would have a larger impact. In fast reactors, use of TRU is not uncommon and hence the impact of inaccurate BRs is larger. Different BRs or fission yields of the same nuclide can be modeled in the REBUS-3 depletion chain with different isotope labels. Different BRs are manageable by this approach while it is too cumbersome for fission yields considering many actinides.

Overall, the above tests show that the simplified burn chain derived in this subsection is acceptable for scoping whole-core depletion calculations with REBUS-3. Without further clarification, it will be used in later depletion calculations of this thesis work.

3.3.3 CFTR-1D Depletion Problem

An integral test of REBUS-3 was performed using the heterogeneous CFTR-1D model. The reference solution to a 480-day whole-core depletion problem under constant total fission power was obtained with Serpent. To save computational efforts while accounting for the flux variation in each assembly, the fast and thermal fuel assemblies were divided into three and five depletion zones, respectively, as shown in Figure 3.23. Each zone is depleted under the zone-averaged flux and atom the density variation in each zone is ignored. For consistent comparison, the constant extrapolation and linear interpolation option was used with single sub-step for each time step in the Serpent depletion calculation. Figure 3.24 shows the evolution of core multiplication factor and assembly averaged burnups of the Serpent reference solution. At the end of cycle (EOC), the fuel burnups are about 32 and 40 MWD/kgU in the fast and thermal assemblies, respectively.

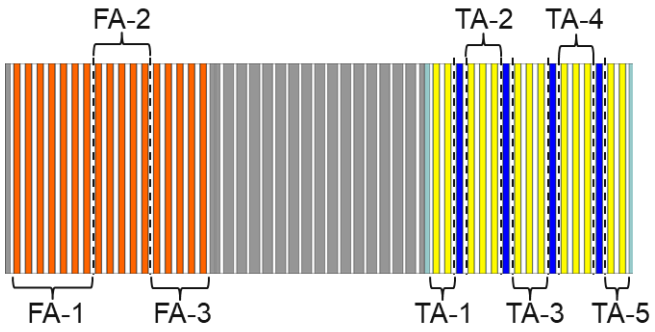

Figure 3.23 Grouping of Fuel Plates in Different Depletion Zones

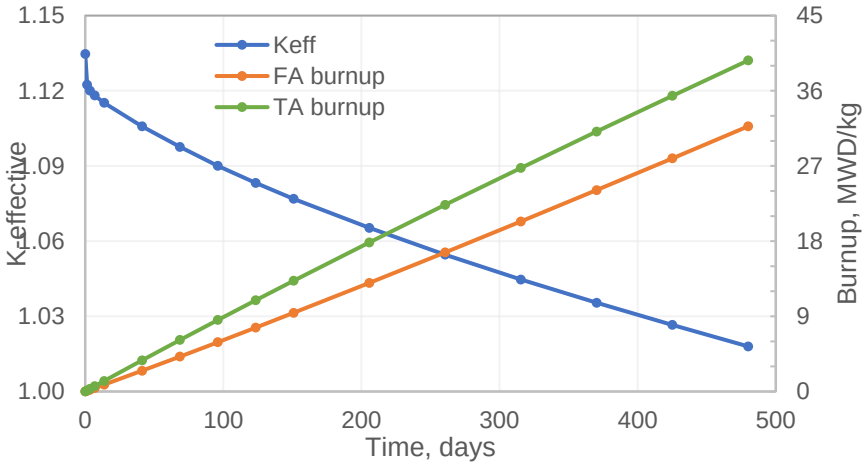

Figure 3.24 Depletion History of CFTR-1D Core of Reference Monte Carlo Solution

In this test, the VARIANT P_1 nodal diffusion option was used in REBUS-3 whole core depletion calculations, using multigroup cross sections generated from Monte Carlo simulations directly. The simplified burn chain derived in Section 3.3.2 was used with constant fission yields corresponding to average energy of neutrons causing fission at the middle of cycle and fixed branching ratios and fission Q-values (for power normalization) consistent with Serpent.

Unlike fast reactors, the stronger burnup dependence of cross sections in coupled-spectrum reactors necessitates burnup dependent isotopic cross sections for whole-core depletion calculations with VARIANT/REBUS. As the first step to quantify the limitations in the existing methods, the reference BGXSs were generated in 13 groups from the reference Monte Carlo full-

core depletion calculation. Since Serpent cannot tally isotopic scattering matrices, the OpenMC code was used to tally microscopic cross sections in fuel assemblies instead. As an example, Figure 3.25 shows the burnup dependent fission cross sections of U235 in the two fuel assemblies of the CFTR-1D core. Regardless of assembly type, the cross sections in fast groups are practically constant while pronounced cross section change occurs in the last two groups (<5 eV). It is expected that for a fast assembly located far away from the thermal spectrum region, constant isotopic cross sections can be used in that the thermal flux would be so small that the error in thermal group cross section does not make a noticeable difference in core calculations.

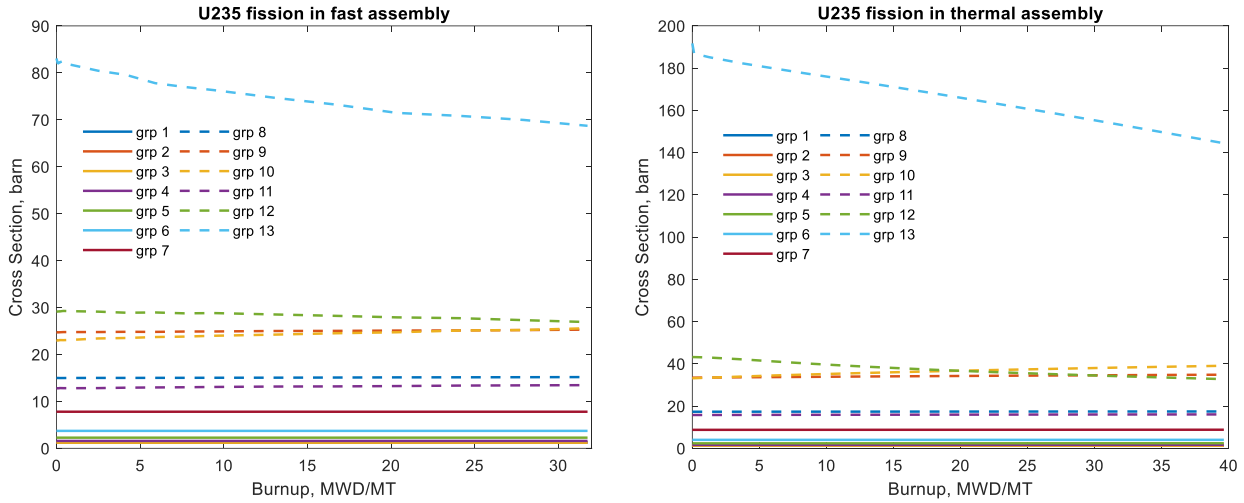

Figure 3.25 Burnup Dependent Fission Cross Section of U235 in Fast and Thermal Assemblies

For nonfuel assemblies, only macroscopic cross sections were generated. It is seen from Figure 3.26 that the macroscopic BGXSs do not vary significantly as expected. Even if the thermal-group (group 13) absorption cross section of the buffer assembly (BA) slightly decreases because of spectrum hardening in the neighboring thermal fuel assembly, the absorption cross section itself is much smaller than the scattering cross section. That is, except for control rod assembly (which is not present in CFTR-1D), using constant BGXSs (generated in representative environment) for nonfuel assemblies would not introduce significant errors in core calculations.

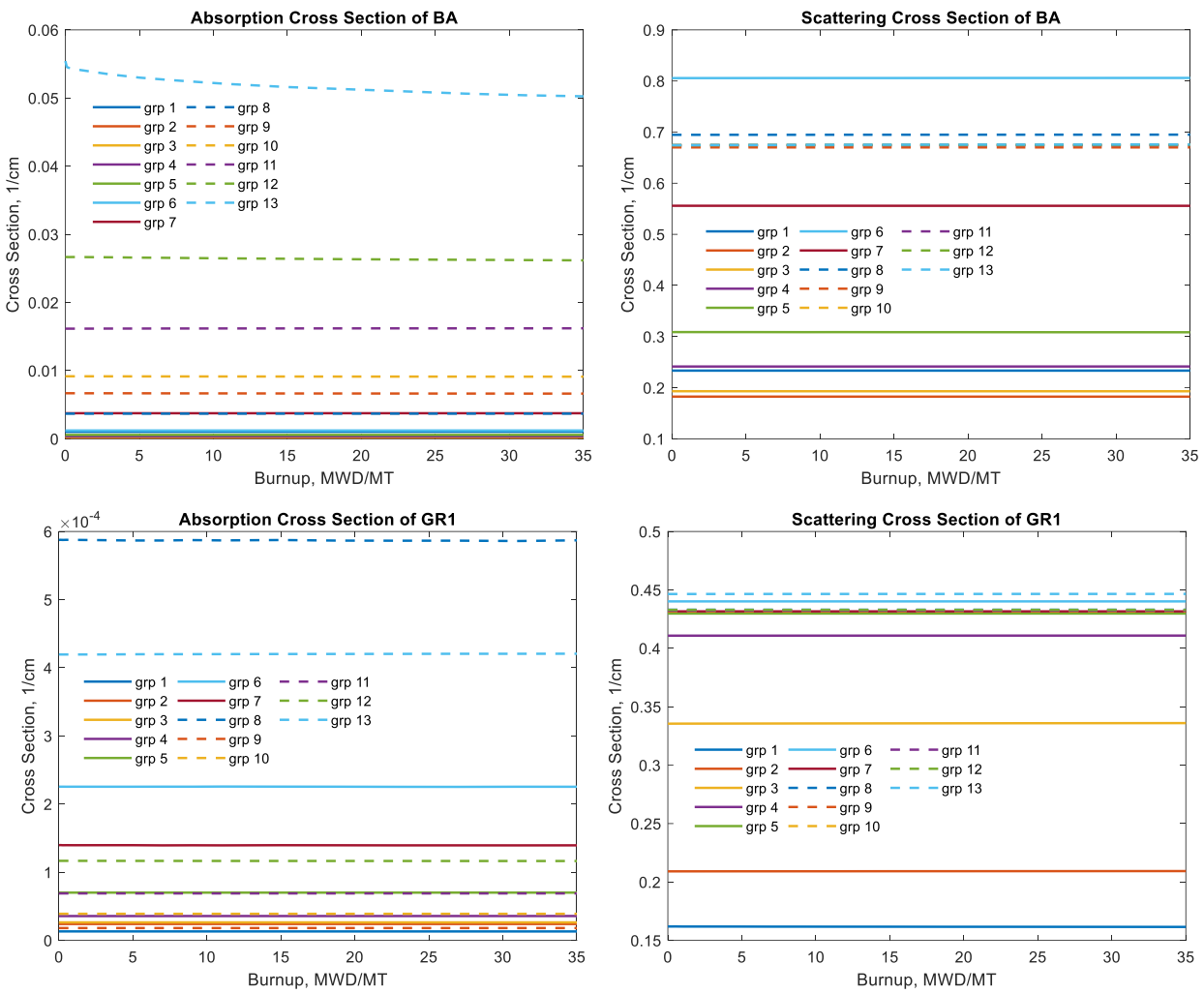

Figure 3.26 Macroscopic BGXSs for Buffer Assembly (BA) and Graphite Reflector (GR1) vs Core Averaged Burnup

Figure 3.27 and Figure 3.28 show the impact of burnup dependency of fuel assembly cross sections on REBUS-3whole core depletion calculation by comparing eigenvalue and assembly power solutions obtained with four different cross section sets. The first one is an ISOTXS dataset generated at equilibrium xenon state, which is approximately reached after about a week of full core depletion. The second is an ISOTXS dataset generated at the middle of cycle (MOC). The third one is a VARIXS dataset containing burnup dependent cross sections for all compositions. Buffer assembly cross sections are functionalized with burnups of the fast fuel assembly and

reflector assembly cross sections are functionalized with the thermal assembly burnups. The last one is a VARIXS dataset containing burnup dependent cross sections for fuel assemblies only, but constant cross sections generated at equilibrium xenon state for the buffer and reflector assemblies. Unity PCDFs were applied in the four calculations and hence the errors due to assembly homogenization were involved.

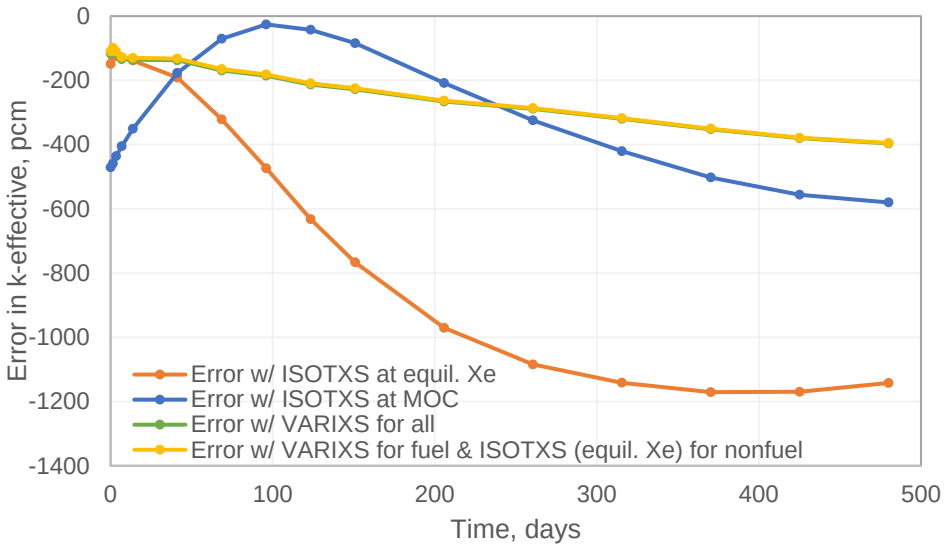

Figure 3.27 K-effective Error of REBUS-3 Depletion Solutions with ISOTXS or VARIXS

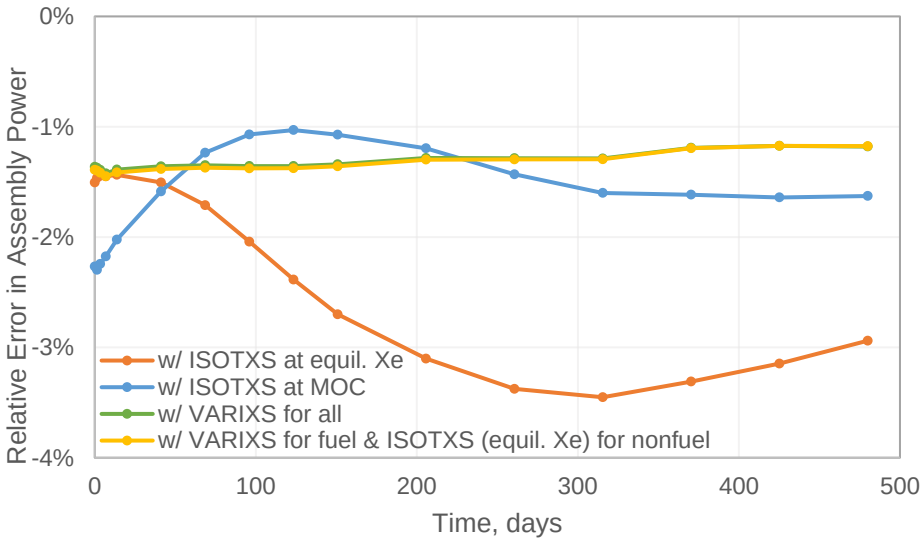

Figure 3.28 Thermal Assembly Power Errors of REBUS-3 Solution Obtained with ISOTXS or VARIXS

As expected, without catching the burnup dependency of fuel cross sections, significant errors were introduced and accumulated in depletion calculations. When burnup dependent fuel cross sections were used, the two core calculations with burnup dependent and constant cross sections for nonfuel assemblies showed less than 10 pcm difference in k-effective and less than 0.1% difference in thermal assembly power. Therefore, constant macroscopic cross sections were used for buffer and reflector assemblies in the following analyses of the CFTR-1D problem.

To eliminate the assembly homogenization error in nodal calculations, a set of PCDFs were generated using the reference BGXSs, nodal average fluxes, and surface average partial currents tallied in Serpent core calculations. Using the reference PCDFs, the REBUS-3 depletion calculation reproduced the Serpent reference depletion solution as shown in Figure 3.29 and Figure 3.30. The maximum error in k-effective is 39 pcm and the relative error in assembly power is less than 0.3%. Comparatively, using PCDFs generated at BOC with equilibrium xenon concentration led to significant eigenvalue errors greater than 1000 pcm, which is worse than the solution obtained using unity PCDFs, i.e., without correcting assembly homogenization errors.

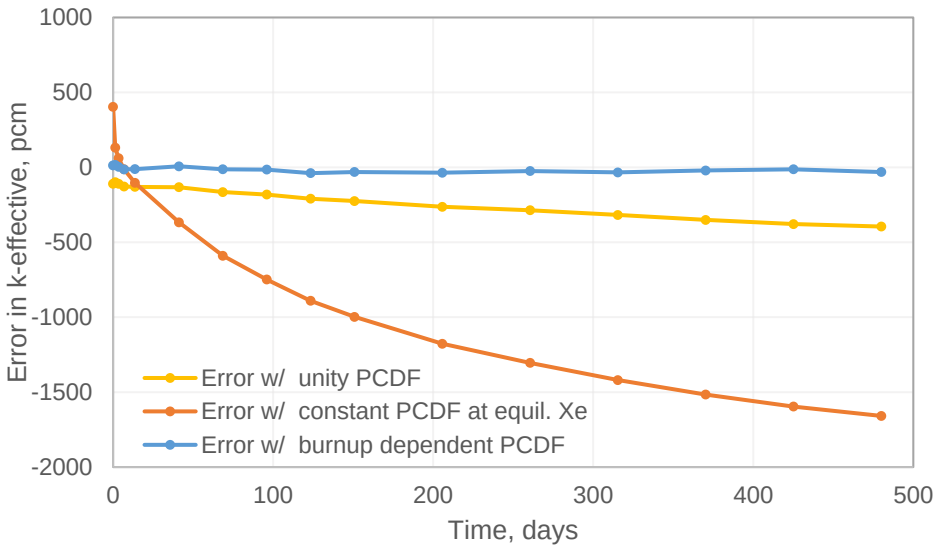

Figure 3.29 K-effective Error of REBUS-3 Solution Obtained with VARIXS and Different PCDFs

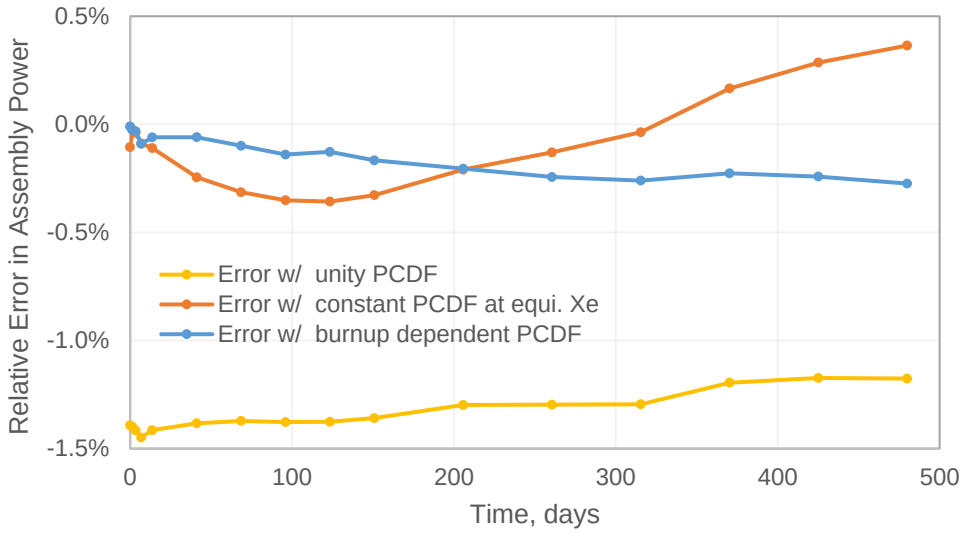

Figure 3.30 Thermal Assembly Power Errors of REBUS-3 Solution Obtained with VARIXS and Different PCDFs

However, Figure 3.30 shows that using BOC PCDFs reduced the assembly power error to below 0.5% from above 1.0% with unity PCDFs. Therefore, the use of equivalence parameter (here PCDF) is critical for eliminating homogenization errors in nodal core calculations, and it is necessary to consider the burnup dependence of the equivalence parameter.

It is worthwhile to test the performance of BGXSs and PCDFs generated using approximate models, such as lattice or supercell models for conventional LWR analyses, in whole-core depletion calculations. As discussed in Section 3.2, supercell models are necessary to produce reliable BGXSs for the CFTR-1D problem. Burnup dependent cross sections and PCDFs were generated in supercell depletion calculations with Serpent and OpenMC. The two supercell models used in supercell depletion calculations are shown in Figure 3.31. BGXSs and PCDFs for the fast fuel and buffer assemblies were generated using the Sup-SA model with all reflective boundary conditions. The Sup-TA model was used for the thermal fuel and all graphite reflector assemblies. The boundary conditions for Sup-TA are reflective on the left and vacuum on the right boundaries, respectively.

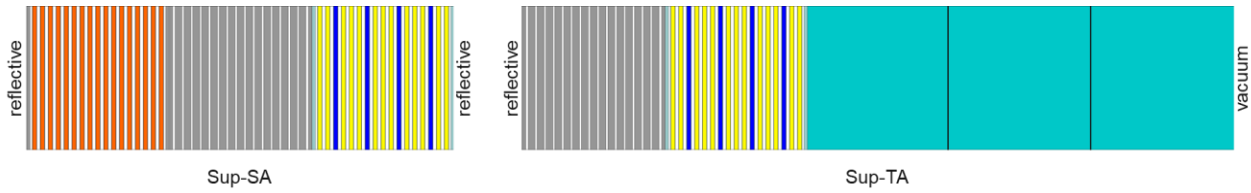

Figure 3.31 One-dimensional Supercell models for Fuel Assemblies

Figure 3.32 compares the eigenvalue errors of REBUS-3 depletion solutions obtained with burnup dependent cross sections and PCDFs generated in full-core and supercell models. The corresponding errors in thermal assembly power are compared in Figure 3.33. Compared to the best solution obtained with the VARIXS and PCDFs generated from the reference full-core solution, replacing the reference VARIXS from the full-core model with the VARIXS from the supercell models caused a smaller difference in depletion solution than replacing the reference PCDFs with the approximate PCDFs generated in supercell models. On the contrary, the depletion solutions with supercell PCDFs showed large errors in eigenvalue and assembly powers, regardless of the model used to generate VARIXS.

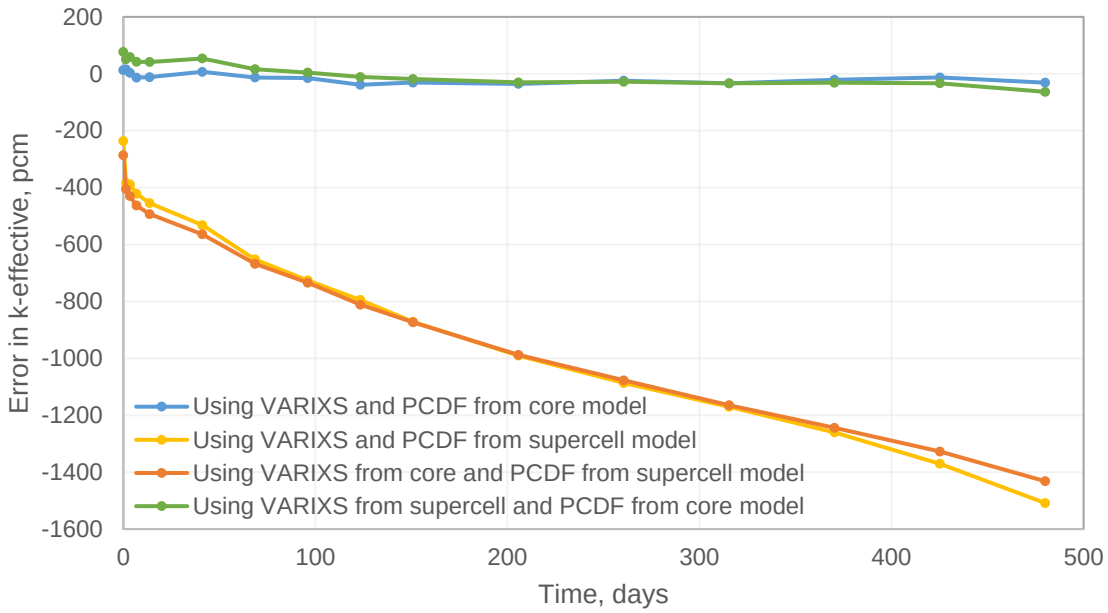

Figure 3.32 K-effective Error of REBUS-3 Depletion Solutions with VARIXS and PCDFs from Full-core and Supercell Models

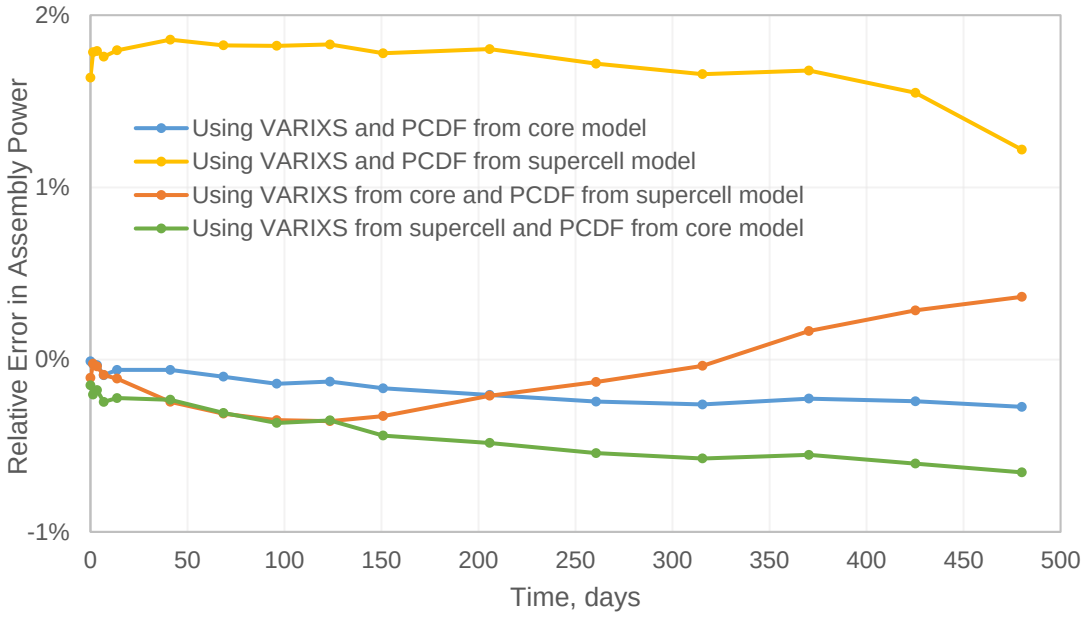

Figure 3.33 Thermal Assembly Power Errors of REBUS-3 Depletion Solutions with VARIXS and PCDFs from Full-core and Supercell Models

It must be noted that PCDFs should be generated with the same BGXSs to be used in subsequent core calculations and the error due to inconsistent use of VARIXS and PCDFs was imbedded here. Nevertheless, it is the inaccurate PCDFs from supercell models that made the larger impact on the depletion solution. This is expected since homogenized BGXSs are volume averaged quantities and they can be well approximated in supercell models, which produce similar average flux spectra as in the core environment. However, PCDFs are defined on nodal surfaces to reproduce local interface conditions and hence are more sensitive to surface leakage, which cannot be properly modeled in supercells.

3.4 Observations

This chapter presents a thorough case study of a simplified coupled-spectrum core problem to highlight the capability gap in the current two-step methods for fast reactor analysis. Through the tests, the biggest challenge turns to be the multigroup cross sections generation considering

resonance self-shielding, local heterogeneity, and global spectrum transition effects. The conventional MC^2-3 approach works reasonably well except for the computational inefficiency to model thermal system in detailed heterogeneous geometries. The Monte Carlo based lattice calculation provides an alternative way for multigroup cross section generation without the complication of self-shielding treatment. The only drawback of generating anisotropic scattering cross section with scalar flux weighting can be overcome by leveraging MC^2-3 calculation.

The second important finding is the need of nodal equivalence parameter for coupled-spectrum reactor analysis. The nodal equivalence parameter can be used as a general correction factor based on the known reference solution. The last part is the test of the REBUS-3 code for non-fast spectrum depletion problems. It turns out the REBUS-3 code can be applied to coupled-spectrum depletion problem with a more detailed depletion chain. The current solution algorithm in REBUS-3 for solving the Bateman equation is sufficiently efficient and accurate for thermal depletion problems. For coupled transport and depletion calculations, other than burnup dependent cross sections, the burnup dependence of nodal equivalence parameters needs to be considered.

Chapter 4

Two-Step Method for Coupled-Spectrum Core Analysis

The two-step method for coupled-spectrum reactor analysis is developed based on the fast reactor analysis code suite of Argonne National Laboratory (ANL). The tests performed in Chapter 3 highlighted the major limitations in the existing methods. In this Chapter, three componential topics of the proposed method, i.e., multigroup cross section preparation, nodal transport calculation, and full-core depletion calculation, are first discussed in separate sections, followed by a summary of the overall procedure for core calculations.

4.1 Multigroup Cross Section Generation

Effective multigroup cross sections (XSs) are essential for accurate deterministic neutronics calculations. The preparation of multigroup XSs is one of the major challenges in deterministic method development. Multigroup XSs for core calculations are typically generated in approximate models with detailed energy resolution but simpler geometry configuration. The major physics to be considered include neutron slowing-down, resonance self-shielding in heterogeneous geometry, and spectrum shift due to environmental impacts. Fast and thermal lattice codes treat the three aspects in different ways. Thermal lattice codes rely on functionalized fine-group cross section libraries that are pre-generated for specific reactor types. The resonance self-shielding is treated approximately with equivalence theory, self-shielding factors, or subgroup methods. On the other hand, fast lattice codes such as MC^2-3 rigorously deals with complex

resonance phenomena especially the resonance interference effect via ultrafine- or hyperfine-group slowing-down calculations for specific compositions.

Comparatively, the method adopted by MC^2-3 is more generalized and has been extended to thermal systems [49]. Ultrafine-group (~3500 groups) or even hyperfine-group (~400,000 groups) slowing-down calculations can be performed for the full energy range, 10^{-5} eV ~ 14 MeV, encountered in nuclear fission reactors. Neutron transport in heterogeneous Cartesian and hexagonal assembly lattices can be modeled with the Method of Characteristics (MOC). However, ultrafine-group MOC calculations in heterogeneous geometries are extremely time-consuming and hence a general application is limited. Besides, MC^2-3 does not have the depletion calculation capability required for generating burnup dependent cross sections.

This dissertation does not intend to develop a new cross section generation code but to search for a new computational procedure utilizing existing codes for multigroup XS generation. In this situation, parallelized Monte Carlo (MC) simulation becomes a complementary option to model neutron transport in heterogeneous geometries efficiently and MC^2-3 is used only to prepare flux moment weighted anisotropic scattering cross sections when necessary. Among the many Monte Carlo codes for reactor physics simulations, Serpent [29] and OpenMC [30] were selected because of their convenient built-in capabilities of tallying multigroup XSs. Serpent has built-in depletion calculation capability while OpenMC provides Python API functions for depletion. The reason of choosing both MC codes for cross section generation is that Serpent cannot tally isotopic scattering matrices whereas OpenMC does not support current tally on hexagonal mesh surfaces, which is needed for partial current discontinuity factor generation. The discontinuity factor is discussed in Section 4.2. It is anticipated that only OpenMC will be needed in the future when the required capability is implemented.

4.1.1 General Approach

In this study, assembly homogenized multigroup XSs are mainly generated with Serpent version 2.1.31 and OpenMC version 0.12.0. Figure 4.1 shows the general procedure to generate multigroup XSs based on MC supercell calculations. The continuous-energy MC simulation in explicit heterogeneous geometry eliminates the need of a sophisticated resonance self-shielding method. Serpent depletion calculations are performed for each type of fuel assembly with supercell models including a targeted assembly and its neighbors. The use of supercell models would accommodate most of the spectral transition effects between adjacent assemblies. Different approaches to consider global spectral transition effects were investigated and eventually it was decided to represent the core environment approximately with surface source or buffer zones in supercell calculations. At each burnup state, the burned fuel compositions are used in an equivalent OpenMC model to generate burnup dependent isotopic cross sections. Burnup independent macroscopic cross sections for nonfuel assemblies are tallied in Serpent directly.

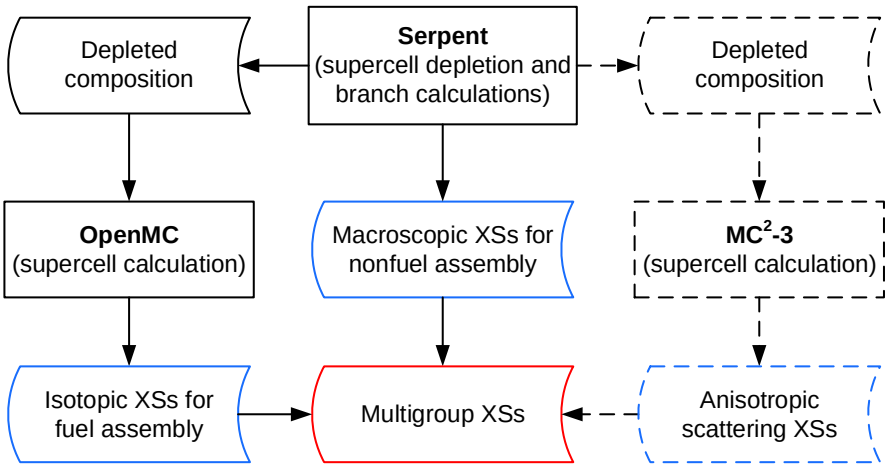

Figure 4.1 General Procedure of MC based Multigroup Cross Section Generation

One drawback of MC based cross section generation is that the anisotropic scattering cross sections are weighted with the spectrum of scalar flux instead of the corresponding flux moment

[88]. Using MC generated anisotropic scattering matrices in deterministic transport calculations would introduce non-negligible errors [92]. To overcome this limitation, anisotropic scattering XSs generated in MC^2-3 supercell calculations are used in transport calculations when anisotropic scattering is considered explicitly. In the following subsections, each aspect of the XS generation scheme is discussed in more details.

4.1.2 Energy Group Structure

Depending on the targeted reactor type, the broad energy group structure used in core calculations varies from few-group structures, e.g., two groups for LWRs and four to seven groups for graphite moderated gas-cooled reactors, to multigroup structures (>10 groups) for fast reactors. The essence is to catch energy spectral properties in cross section generation with approximate models while minimizing computational burden in full-core calculations. Cross sections are less sensitive to the approximate models when represented in a refined energy group structure. Without pursuing an optimized group structure, we started with the widely adopted 33-group structure in MC^2-3 for fast reactor analyses and adapted it for coupled-spectrum reactors. The resultant 32-group (32G) structure is shown in Table B.1 of Appendix B. A coarser group structure consisting of 13 groups (13G) was developed by refining the last two groups (below 454 eV) of the MC^2-3 9-group structure for fast reactor calculations. The detailed group boundaries are also provided in Appendix B. For both the 32G and 13G structures, a single thermal energy group below 0.6 eV is defined because there is not much resonance in the thermal energy range and cross sections will be functionalized with state conditions.

In Chapter 3, both 32G and 13G structures were used in test calculations. It is shown in Table 3.1, Table 3.3, and Table 3.4 that the two broad-group structures yielded comparable transport solutions with either reference full-core model or assembly supercell model for cross

section generation. Replacing 32G structure with 13G structure in core calculations induced only ~30 pcm differences in eigenvalue. Although none of them reproduced the reference solution, the major error source is not the use of coarser group structure but in the model to produce the weighting spectra for group condensation.

In addition to the two broad-group structures, a fine-group structure consisting of 86 groups (86G) and an ultrafine-group structure consisting of 989 groups (989G) were derived to investigate leakage correction models. The 86G structure combines the 60 groups above 5.0 eV of the MC^2-3 70-group structure and the 26 groups below 5.0 eV of the SCALE 56-group. The 989G structure contains 892 groups above 5.0 eV of the MC^2-3 1041-group structure and 97 groups below 5.0 eV of the SCALE 252-group structure. The two finer group structures are supersets of the above broad-group structures and are used in the fine-group full-core transport calculation to account for global spectrum transition effects.

In the conventional MC^2-3 scheme for fast reactor cross section generation, full-core transport calculations are performed in ultrafine group level and ultrafine-group XSs are prepared in unit cell or assembly lattice calculations. In a previous study [118] conducted by the author, it is shown that a fine-group structure (~100 groups) can be used for the full-core calculation once the supercell model is used to prepare the fine-group XSs. As shown in Figure 4.2, the fine-group XSs tallied in a supercell model including immediate neighbors agreed well with the reference XSs tallied in the full-core model.

In Ref. [118], a 157-group structure consisting of 60 groups above 5.0 eV and 97 groups below 5.0 eV was used. Figure 4.3 shows that the number of fine groups can be further reduced to 86 by using only 26 groups below 5.0 eV. The 86G capture cross sections tallied in supercell (see Figure 3.8) and full-core models are practically the same for the thermal assembly. The relatively

large XS errors of the fast assembly below 100 eV are due to neglect of thermal neutrons from the thermal zone in the supercell calculation. Below 0.01 eV, the fast assembly supercell model did not produce statistically meaningful XS tally due to the small thermal flux level.

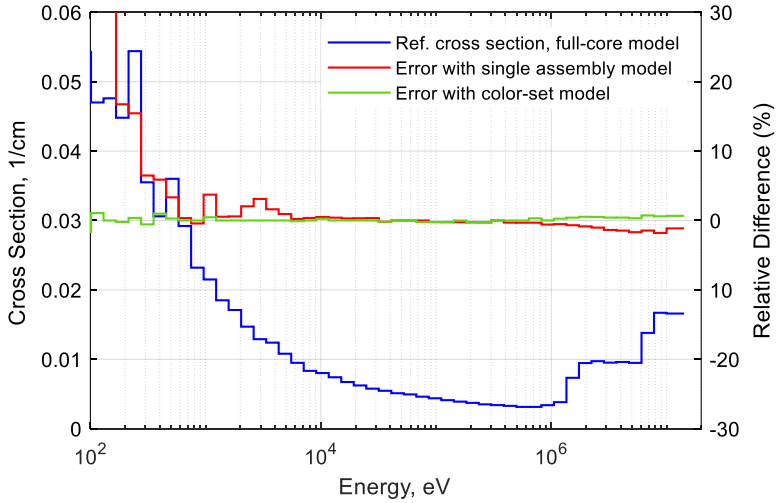

Figure 4.2 Comparison of Macroscopic Fission Cross Sections of a Fast-zone Fuel Assembly in a Coupled Fast-Thermal Spectrum Reactor [118]

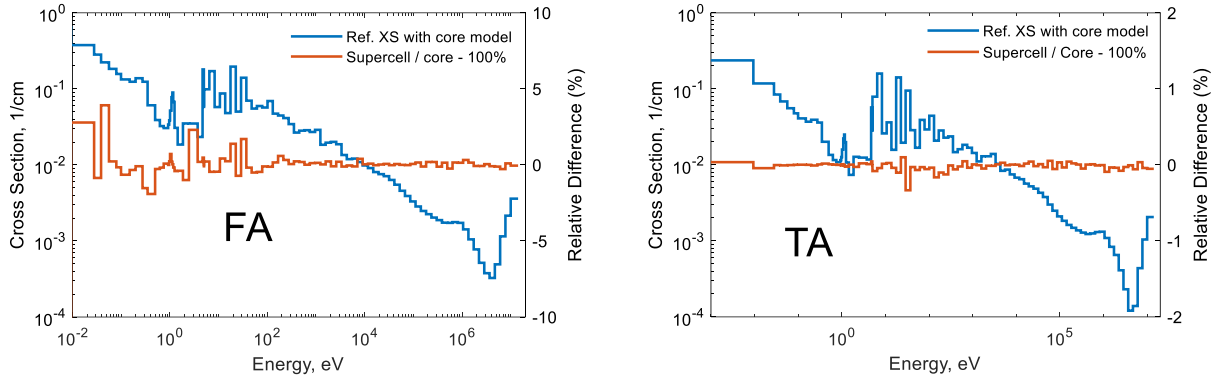

Figure 4.3 Comparison of 86G Macroscopic Capture XSs of Fast Assembly (FA) and Thermal Assembly (TA) in CFTR-1D Core

4.1.3 Selection of Supercell Models

For LWR analyses with legacy two-step methods, critical buckling search is still a common approach in lattice calculations to generate few-group cross sections with nonzero net leakage. Supercell (color set) models were used to account for spectral transition between oxide and MOX

fuel assemblies [119] or between fuel assembly and reflector, in which case reflective conditions are imposed on the outer boundaries and the buckling search for critical spectrum is typically not performed. The decision to generate multigroup XSs primarily with supercell models was made based on several compromises necessary for coupled-spectrum reactor analysis. The obvious negative side is that supercell calculations would be more expensive than assembly lattice calculations and the number of unique supercell types is generally larger than assembly types in a specific core configuration. On the other side, supercell models would significantly alleviate the burden of treating inter-assembly spectral interference.

Typically, over 1,000 groups need to be used in assembly calculation to catch the spectrum transition between fuel and reflector assemblies in a fast reactor [120]. But as shown in Chapter 3, even with an UFG (989G) structure, non-negligible deviations in capture cross sections in the resonance region were observed in CFTR-1D (see Figure 3.9). From the practical point of view, tallying UFG cross sections in heterogeneous Monte Carlo simulation is prohibitively expensive. Thus, assembly supercell models are necessary for cross section generations for a heterogeneous core with distinct assembly types. With supercell models, the tilted distribution of burnup states in a fuel assembly can also be partially considered when generating burnup dependent cross sections.

The selection of supercell models is largely based on engineering heuristics. The general standard for valid supercell models in this study is that fine-group cross sections can be generated accurately. With reliable fine-group cross sections, leakage correction models can be applied to produce accurate broad-group cross sections when the global spectral transition effect is pronounced. Through parametric studies, the modeled problem domain should extend at least three mean free paths (MFPs) away from the assembly of interested. By MFP, we meant the neutron mean free path in the neighborhood. This is usually satisfied by including immediate neighboring

assemblies in the supercell model in water moderated thermal reactors. With graphite moderator, or when the neutron moderation predominantly occurs outside the fuel assembly (like in CFTR-1D), the supercell model should include a sufficiently thick buffer zone such that the fuel to moderator ratio is roughly preserved. The buffer zone size can be reduced by increasing atom density to preserve the optical thickness.

In fast reactors, due to the longer neutron MFP, inclusion of more assemblies beyond the immediate neighbors seems inevitable. However, because not many neutrons reach the heavy nuclide resonance region (< 1 keV), inclusion of distinct neighbors in the supercell model would be sufficient to account for spectral interference in the high-energy range, as exemplified in Figure 4.2 and Figure 4.3, where the fast assembly supercell included only adjacent neighbors and reflective boundary conditions were imposed. Reflective boundary conditions imply that distant assemblies have similar spectral properties. It is not true in general but in typical CFTR designs the fast zone locates inside the core for better neutron economy. The thermal neutrons from the exterior thermal zone can hardly enter the fast zone when a buffer zone exists. They induce small errors in the fine-group cross sections as shown in Figure 4.3. Treatment of this long-range environmental effect is discussed in the next section.

4.1.4 Correction of Global Spectrum Transition

To accommodate global spectral transition effects in coupled-spectrum reactors, the first trial was an analogy to the conventional MC^2-3 two-step approach. Fine-group XSs are initially prepared in supercell MC calculations and then are used in homogenized full-core calculations to produce region dependent fine-group spectra. Subsequently, region dependent broad-group XSs are generated by collapsing the fine-group XSs with corresponding fine-group spectra. As tested for the CFTR-1D problem in Chapter 3 and for a larger 2D coupled-spectrum core problem in a

previous study [118], the two-step approach worked well for steady-state transport analysis as only one fine-group full-core (with simplified geometry) calculation is needed. However, the core configuration changes with fuel depletion and it is unknown when cross sections are generated. Instead of repeating full-core calculations at each burnup state, alternative approaches to consider global spectral transition effects in supercell calculations were pursued, and eventually a background source approximation correction was selected.

4.1.4.1 Leakage Model for Monte Carlo Methods

Several leakage correction models have been developed for MC based lattice calculations. The capability of homogeneous B_1 calculation for critical buckling search is available in Serpent. The B_1 calculation is performed with internal deterministic solver using tallied multigroup cross sections during the standard MC transport simulation. An energy independent critical buckling is determined for the homogenized region. When only part of the modeled geometry is to be homogenized with supercell models, the use of B_1 calculation for leakage correction does not make much sense as the realistic environment is already included in the model. Hence, this capability of Serpent was not further investigated in this study.

The B_1 method implemented in MC codes is an analogy to that utilized in deterministic lattice codes. Other leakage correction methods developed purely in the Monte Carlo framework include critical albedo search [121] and layer expansion method [122]. Just as its name implies, critical albedo search finds the critical state by adjusting the weight of neutrons reflected at the boundary. As for the layer expansion method, neutrons are tracked beyond the reflective or periodic boundaries in an expanded fictitious lattice. The neutron weight is modified at certain expanded layer such that the desired eigenvalue is reached. To some extent, these two methods are like critical buckling search but can be easily incorporated into heterogeneous MC simulations.

Especially, the albedo search can be directly applied to supercell models. Both methods were implemented in Serpent, but the layer expansion method is not included in the standard distribution package of the Serpent code [122]. Comparisons between the two methods showed similar performances [122].

The limitation of albedo search is that only one degree of freedom is given like buckling search. The same energy independent albedo is uniformly applied to all boundaries. Serpent allows individual albedos in the x-, y-, and z-direction (all with reflective boundary conditions) with user specified fractions but not for individual boundaries. Nonetheless, the specification of direction dependent albedo fractions is fully empirical and requires trial and error. This would cause problems when the environment is not symmetrical and global flux gradient exists.

For example, Figure 4.4 compares the 32G capture cross sections directly generated with the supercell models, as shown in Figure 4.5, for the thermal fuel assembly in the homogenized CFTR-1D problem. The supercell-1 includes the buffer assembly and all three graphite reflectors, and the supercell-2 includes only one and half reflectors. Without albedo search, vacuum condition is imposed on the right boundary. When albedo search is applied to reproduce the reference reactivity level, the same albedo is imposed on both left and right boundaries of the 1D supercells.

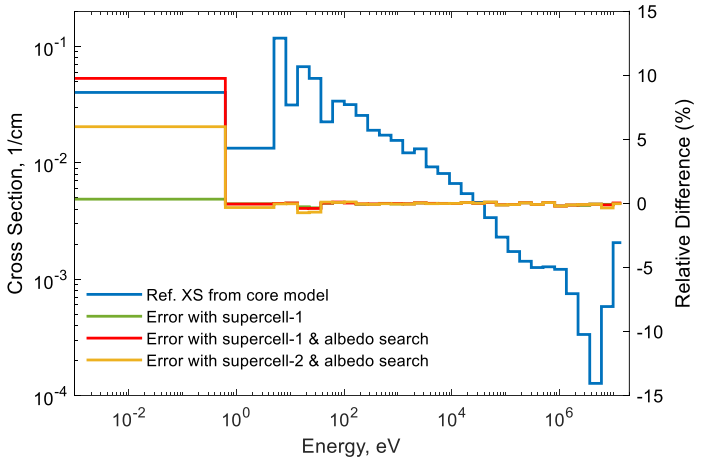

Figure 4.4 Comparison of 32G Capture XS of Thermal Assembly in CFTR-1D Core

Figure 4.5 Supercell Models for Thermal Assembly in Homogenized CFTR-1D (Vacuum conditions on the right are replaced with reflective ones when albedo search is invoked.)

Figure 4.4 shows that the supercell calculations with albedo search resulted in large errors in the thermal group cross section. This is because the physical vacuum boundary condition is changed to an arbitrary partially reflective condition. Consequently, more neutrons are reflected into fuel assembly from the graphite reflectors, as implied by the flux spectrum comparison in Figure 4.6. The error is reduced when less reflectors are included, but a "correct" configuration is not intuitive.

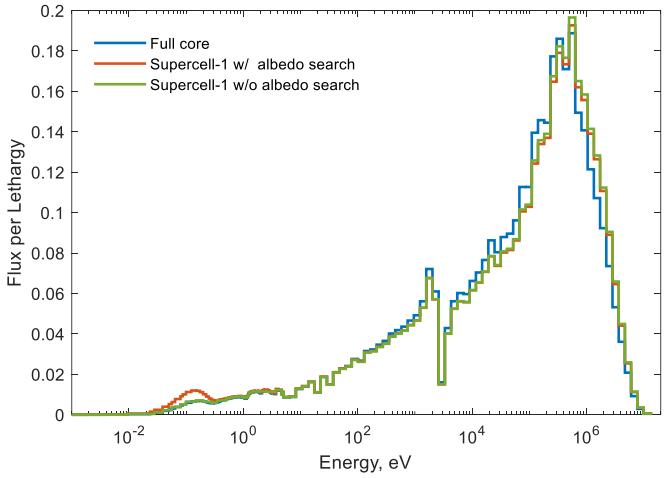

Figure 4.6 Flux spectrum of Thermal Assembly in CFTR-1D Core

4.1.4.2 Buckling Search for Supercell

Because of the limited applicability of the albedo search technique to supercell problems with non-uniform boundary conditions, an alternative approach is needed. Besides, the critical

buckling/albedo search methods only partially eliminate the spectrum distortion due to scaled fission source. The bigger difficulty is the spectral transition effect, for which the energy dependence of leakage needs to be considered. With supercell models and a fine-group structure, a large portion of the spectral transition effects due to neighbor assemblies is already considered.

A case study was performed to investigate the impact of long-range spectral transition effects using the homogenized CFTR-1D problem and 86G cross sections generated with supercell models. For high-order transport calculations, the anisotropic scattering matrices were generated with MC^2-3. Table 4.1 shows the corresponding transport results of VARIANT obtained with different anisotropic scattering matrices for the thermal assembly. The principal (e.g., total, capture, fission, etc.) and isotropic scattering XSs are all tallied in Serpent supercell simulations. It is seen that using the anisotropic scattering XSs from the MC^2-3 supercell calculation does not reproduce the reference solution. It was later revealed that the thermal assembly anisotropic scattering XSs from the supercell MC^2-3 calculation have non-negligible errors. As shown in Figure 4.7, while isotropic scattering cross sections of supercell and full core agree with each other just like the other principal cross sections, the P_1 anisotropic scattering cross section generated with the supercell model noticeably deviates from that of the core model.

Table 4.1 VARIANT transport solutions obtained with 86G XSs generated in supercell models

Source of principal & isotropic scattering XSs	Source of anisotropic scattering XSs	Δk, pcm	Assembly power error	
			FA	TA
Serpent supercell	MC^2-3 whole core	-16	0.02%	-0.02%
	MC^2-3 supercell	142	0.62%	-0.58%
	Buckled supercell[(a)]	49	0.54%	-0.51%
	Group buckled supercell[(b)]	25	0.03%	-0.03%

Notes:
(a) Use UFG cross sections and perform group independent buckling search
(b) Use UFG cross sections and impose group dependent buckling deduced from reference leakage

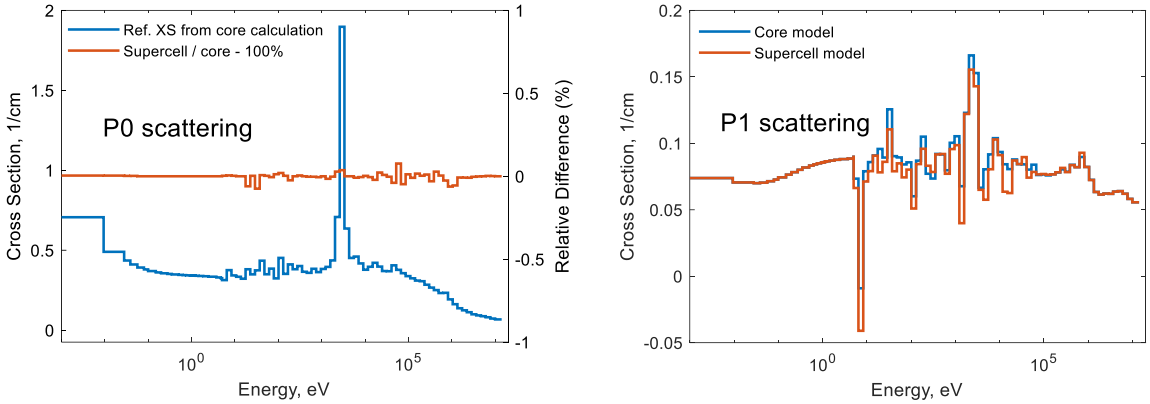

Figure 4.7 Thermal Assembly Scattering Cross Sections Generated by MC^2-3

The thermal assembly supercell model cannot consider the long-range environmental effects due to the fast assembly. To correct the spectrum tilt due to differently scaled fission source, a buckling search was performed to yield the same reactivity level in the supercell calculation. Unlike Monte Carlo albedo search, the leakage correction was only performed for the left boundary and the vacuum condition was retained on the right boundary. First a set of UFG cross sections were generated in supercell models. Then UFG supercell transport calculations were performed with VARIANT and the buckling of the buffer assembly was iteratively selected such that the desired k-effective was reached. In VARIANT, the given buckling is used to modify the removal cross section of specified composition (here the buffer assembly composition), which equivalently alters the neutron balance resembling leakage change. At last, the UFG spectrum obtained at the same reactivity state as the reference core calculation was used to condense UFG cross sections into 86 groups.

However, the group independent buckling search did not resolve the error in anisotropic scattering cross section as shown in Table 4.1 (buckled supercell case). Figure 4.8 explains the reason. As the scalar flux spectrum is roughly reproduced, the P_1 flux moment spectrum used to condense the P_1 scattering cross sections still deviates from core solution. This implies that the

current (and higher-order flux moments) spectrum is more sensitive to the boundary condition. Alternatively, a group dependent buckling was deduced from the reference leakage of core calculation and imposed in the buffer assembly composition. This is equivalent to providing an external source to the supercell. Without matching k-effective, the group dependent buckling significantly improved the P_1 flux moment spectrum as shown in Figure 4.9. Using the resultant 86G anisotropic scattering cross section in the VARIANT core calculation, the reference solution was reproduced as shown in Table 4.1 (group buckled supercell case).

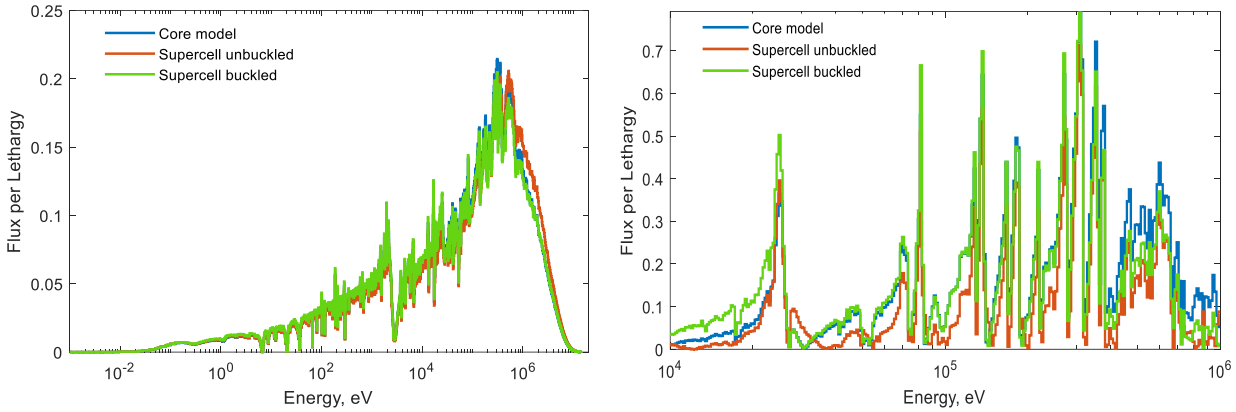

Figure 4.8 Comparison of Scalar Flux (Left) and P_1 Flux Moment (Right) Spectra of 989G VARIANT Transport Solutions to Core and Supercell Problems

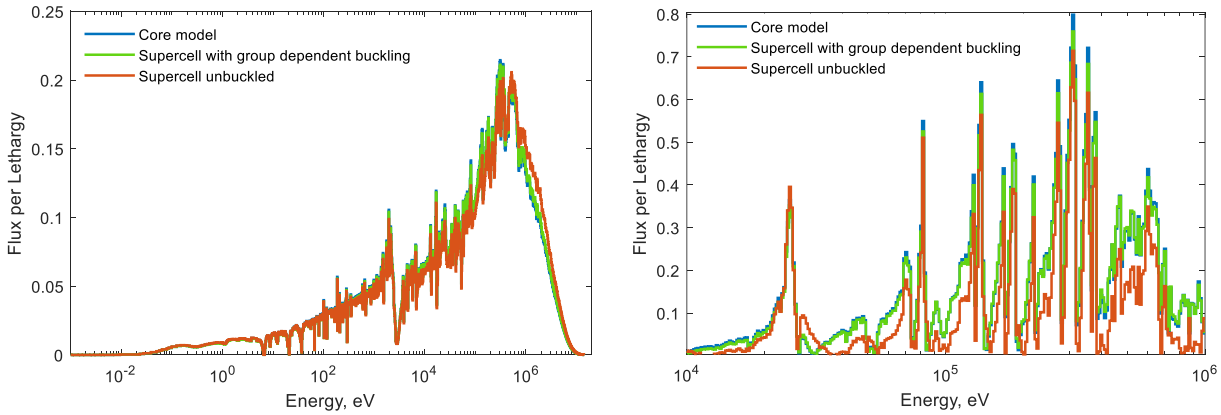

Figure 4.9 Comparison of Scalar Flux (Left) and P_1 Flux Moment (Right) Spectra of 989G VARIANT Transport Solutions to Core and Supercell with Group Dependent Buckling

The above test indicates that the energy dependence of leakage makes a larger difference in multigroup cross sections than the spectrum tilt due to different reactivity level. This observation inspired the background source approximation for handling long-range spectrum transition effects.

4.1.4.3 Background Source Approximation

In practical supercell calculations, the group dependent leakage correction is provided by imposing an approximate background source on the supercell boundary. This way, broad-group cross sections can be directly generated from Monte Carlo supercell simulations. The background source can be either a buffer zone producing representative neutron source or a fixed surface source. Figure 4.10 and Figure 4.11 show the supercell models for the fast (FA) and thermal (TA) fuel assemblies in the homogenized CFTR-1D core and the corresponding broad-group (13G) capture cross sections generated using these models, respectively. The fast assembly supercell model includes a half-width thermal assembly as the thermal neutron source zone. The thermal assembly supercell model does not include a fast zone (otherwise it would be the full core) but a surface source on the left boundary, for which the spectrum of the fast assembly leakage obtained in the fast assembly supercell model was used.

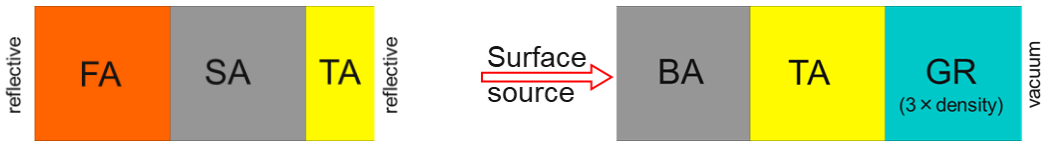

Figure 4.10 Fuel Assembly Supercell Models with Background Source

With a thermal source zone, the fast assembly cross sections were accurately generated in most groups. The thermal group cross section has a larger error because of the reflective boundary condition outside the source zone. The thermal assembly cross sections were also improved, especially in a high-energy group.

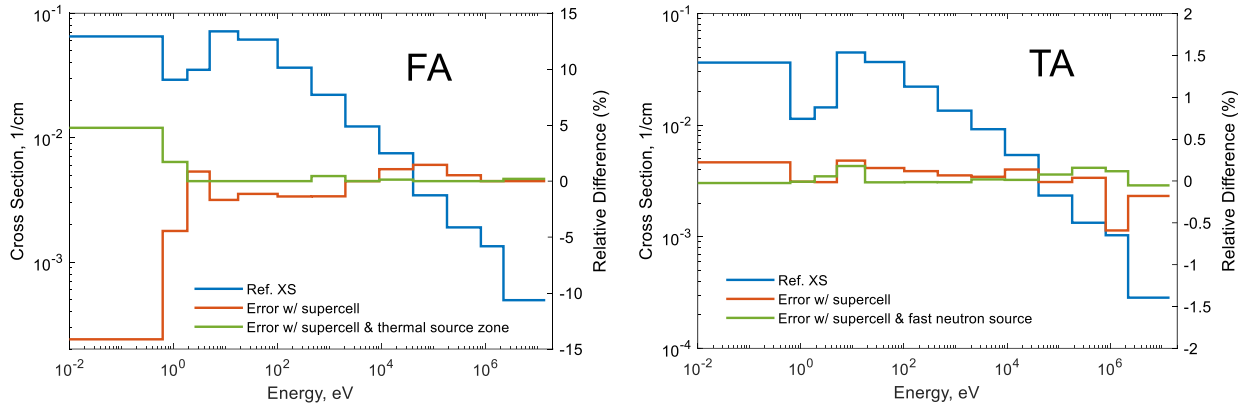

Figure 4.11 13G Capture Cross Sections Obtained in Supercell Models with Background Source

Burnup dependent cross sections for fuel assemblies are generated in Monte Carlo depletion calculations in supercell models. The global core environment changes with depletion, but in supercell depletion, the background source zone or the surface source is assumed unchanged. This assumption is based on the observation that the leakage spectrum does not vary drastically with depletion, as shown Figure 4.12.

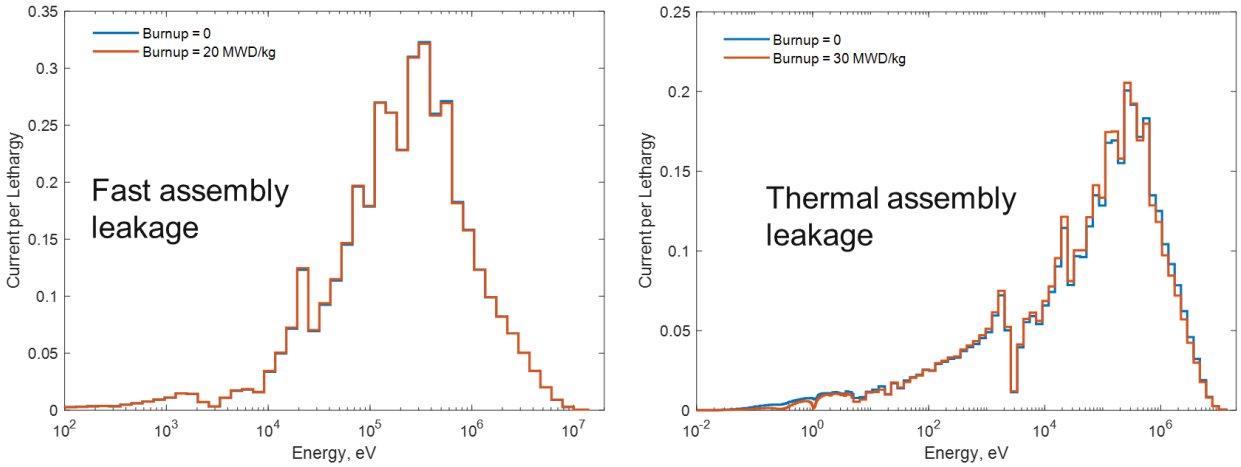

Figure 4.12 Spectrum Variation with Fuel Depletion in CFTR-1D Core

4.2 Nodal Transport Method with Partial Current Discontinuity Factor

In this study, a new transport equivalence method was developed for implementation in the variational nodal transport code VARIANT. A nodal equivalence theory based on scalar flux DFs

was previously incorporated in VARIANT for prismatic Very High Temperature Reactor (VHTR) analysis [70], but it was limited to P_1 approximation. However, diffusion theory solutions may not be satisfactory for coupled fast-thermal reactor analysis because of the pronounced transport and anisotropic scattering effects in the fast zone. In order to enhance the flux solution accuracy by reducing the assembly homogenization error, a new nodal equivalence theory method based on partial current discontinuity factors (PCDFs) has been developed for black-box homogenization and incorporated in VARIANT [118]. The PCDF based nodal equivalency model is derived in this section along with the method to generate PCDFs for core calculations.

4.2.1 Variational Nodal Transport Method

The VARIANT code solves the neutron transport equation in 3D Cartesian and hexagonal geometries based on assembly homogenized core models. It is based on the variational nodal method that guarantees nodal balance and permits refinement using hierarchical complete polynomial trial functions in space and spherical harmonics in angle. In the variational nodal method, the second-order form of the even-parity transport equation [36] is solved in each node and the even-parity fluxes of adjoining nodes are coupled through odd-parity fluxes at the nodal interface.

The derivation of the second-order form of the even-parity transport equation starts with splitting the angular flux into even- and odd-parity components as:

$$\psi_g(\vec{r},\hat{\Omega}) = \psi_g^+(\vec{r},\hat{\Omega}) + \psi_g^-(\vec{r},\hat{\Omega}), \tag{4.1}$$

where $\psi_g^+(\vec{r},\hat{\Omega})$ and $\psi_g^-(\vec{r},\hat{\Omega})$ are the even- and odd-parity angular fluxes that satisfy the following properties:

$$\psi_g^+(\vec{r},-\hat{\Omega}) = \psi_g^+(\vec{r},\hat{\Omega}),\ \ \psi_g^-(\vec{r},-\hat{\Omega}) = -\psi_g^-(\vec{r},\hat{\Omega}). \tag{4.2}$$

Coupled transport equations for even- and odd-parity angular fluxes are obtained by adding and subtracting the Boltzmann transport equations for $\hat{\Omega}$ and $-\hat{\Omega}$ directions. By eliminating the odd-parity angular flux, the second-order form of the even-parity transport equation can be obtained as:

$$-\hat{\Omega}\cdot\vec{\nabla}\left[\frac{1}{\Sigma_{t,g}(\vec{r})}\hat{\Omega}\cdot\vec{\nabla}\psi_g^+(\vec{r},\hat{\Omega})\right]+\Sigma_{t,g}(\vec{r})\psi_g^+(\vec{r},\hat{\Omega})=\Sigma_{s,g\to g}(\vec{r})\phi_g(\vec{r})+Q_g(\vec{r},\hat{\Omega}), \qquad (4.3)$$

where $Q_g(\vec{r},\hat{\Omega})$ includes fission source as well as scattering source from other groups. It is noted that isotropic scattering is assumed in the derivation of Eq. (4.3) for simplicity while anisotropic scattering is treated in VARIANT as discussed in Ref. [67].

The variational nodal method is derived from the functional defined on nodal volumes and nodal interfaces, where the odd-parity flux is used as a Lagrange multiplier. Requiring this functional to be stationary with respect to variations of ψ_g^+ and ψ_g^- leads to the second-order form of the even-parity equation within each node, given in Eq. (4.3), and the odd-parity transport equation at the interfaces:

$$\hat{\Omega}\cdot\vec{\nabla}\psi_g^+(\vec{r},\hat{\Omega})+\Sigma_{t,g}(\vec{r})\psi_g^-(\vec{r},\hat{\Omega})=0. \qquad (4.4)$$

This functional is reduced to a quadratic form by expanding the even- and odd-parity fluxes in terms of complete polynomial trial functions in space and spherical harmonics in angle. The intra-nodal distribution of the even-parity angular flux of group g is expanded as:

$$\psi_g^+(\vec{r},\hat{\Omega})=\sum_{i,m}f_i(\vec{r})g_m(\hat{\Omega})\zeta_{g,im}^+, \qquad (4.5)$$

where $f_i(\vec{r})$'s are complete polynomial trial functions, $g_m(\hat{\Omega})$'s are even-order spherical harmonics, and $\zeta_{g,im}^+$'s are the expansion coefficients called the flux moments. The odd-parity angular flux on each nodal interface γ is represented as:

$$\psi^{-}_{\gamma,g}(\vec{r},\hat{\Omega}) = \sum_{j,n} h_{\gamma,j}(\vec{r}) k_{\gamma,n}(\hat{\Omega}) \chi^{-}_{\gamma g,jn}\,, \tag{4.6}$$

where $h_{\gamma,j}(\vec{r})$'s are polynomial trial functions and $k_{\gamma,n}(\hat{\Omega})$'s are odd-order spherical harmonics, and $\chi^{-}_{\gamma g,jn}$'s are odd-parity flux moments.

The linear system of equations for the expansion coefficients or even- and odd-flux moments $\zeta^{+}_{g,im}$ and $\chi^{-}_{\gamma g,jn}$ is obtained by requiring the reduced functional to be stationary with respect to variations of these flux moments. To efficiently solve the system of algebraic equations of flux moments, a linear transformation of the flux moment variables is applied [123]:

$$\vec{J}^{\pm}_{\gamma,g} = \frac{1}{4}\vec{\zeta}_{\gamma,g} \pm \frac{1}{2}\vec{\chi}_{\gamma,g}, \tag{4.7}$$

where $\vec{J}^{\pm}_{\gamma,g}$ is a vector of partial current moments on surface γ, $\vec{\zeta}_{\gamma,g}$ and $\vec{\chi}_{\gamma,g}$ are vectors of even- and odd-parity flux moments on the same surface. Eventually, a set of nodal response matrix equations are obtained for the partial currents of neutrons exiting and entering the node. The inter-nodal continuity conditions for the partial current moments are then used to solve the global equations using the red-black iteration method [123].

4.2.2 Partial Current Discontinuity Factor

Now we derive the partial current discontinuity factor for VARIANT implementation. This section is largely adapted from a previous publication [118] of the author. Omitting the group index, the within-group nodal response matrix equation for partial currents is simply put as:

$$\vec{J}^{+} = \vec{S} + \boldsymbol{R}\vec{J}^{-}, \tag{4.8}$$

where $\vec{J}^{+}$ and $\vec{J}^{-}$ are the outgoing and incoming partial-current-like vectors, $\vec{S}$ is the volumetric source term for this group, and $\boldsymbol{R}$ is the response matrix. In the P_1 approximation, $\vec{J}^{+}$ and $\vec{J}^{-}$ reduce to the surface partial currents in diffusion theory model. In a higher order angular approximation,

they are linear combinations of even- and odd-parity angular fluxes across nodal surfaces. The response matrix equations for a heterogeneous node and its equivalent homogenized node can be written as:

$$\vec{J}_h^+ = \vec{S}_h + \boldsymbol{R}_h \vec{J}_h^-, \tag{4.9}$$

$$\vec{J}_m^+ = \vec{S}_m + \boldsymbol{R}_m \vec{J}_m^-, \tag{4.10}$$

where the subscripts h and m denote the quantities in the heterogeneous and homogenized nodes, respectively. With the flux-volume weighting for cross section homogenization, the node average reaction rates and hence the volumetric source can be preserved only when the net leakage of the homogenized node matches that of the reference heterogeneous node as:

$$\vec{J}_m^+ - \vec{J}_m^- = \vec{J}_h^+ - \vec{J}_h^-. \tag{4.11}$$

To satisfy Eq. (4.11), the discontinuity condition of partial currents of the homogenized nodes is introduced with a PCDF for each partial current moment i on each nodal surface γ as:

$$f_{\gamma,i}^+ = \frac{J_{h,\gamma,i}^+}{J_{m,\gamma,i}^+}, \quad f_{\gamma,i}^- = \frac{J_{h,\gamma,i}^-}{J_{m,\gamma,i}^-}, \tag{4.12}$$

where $f_{\gamma,i}^+$ and $f_{\gamma,i}^-$ are the PCDFs for outgoing and incoming currents, respectively. By combining Eq. (4.12) for all partial current moments, one obtains

$$\vec{J}_m^+ = \boldsymbol{D}_+ \vec{J}_h^+, \quad \vec{J}_m^- = \boldsymbol{D}_- \vec{J}_h^-, \tag{4.13}$$

where $\boldsymbol{D}_+$ and $\boldsymbol{D}_-$ are diagonal matrices composed of $1/f_{i,\gamma}^+$ and $1/f_{i,\gamma}^-$, respectively.

Eq. (4.7) says that the net current acts as the odd-parity flux and hence the physically required continuity of net current across nodal interface implies the continuity of odd-parity angular flux. Thus, the discontinuity of partial currents is equivalent to the discontinuity of even-parity angular flux. Therefore, a discontinuity factor (EPDF) can be directly introduced for the even-parity flux [55]. The reason that PCDF is preferred over EPDF for VARIANT

implementation is discussed in Section 4.2.3. Inserting Eq. (4.13) into Eq. (4.10) and requiring the reference volumetric source to be preserved yield

$$\boldsymbol{D}_{+}\vec{J}_h^{+} = \vec{S}_h + \boldsymbol{R}_m\boldsymbol{D}_{-}\vec{J}_h^{-}. \tag{4.14}$$

Using Eq. (4.13), Eq. (4.11) can also be written as

$$\boldsymbol{D}_{+}\vec{J}_h^{+} - \boldsymbol{D}_{-}\vec{J}_h^{-} = \vec{J}_h^{+} - \vec{J}_h^{-}. \tag{4.15}$$

Subtracting Eq. (4.14) from Eq. (4.15) yields

$$(\boldsymbol{R}_m - \boldsymbol{I})\vec{J}_m^{-} = \vec{J}_h^{+} - \vec{J}_h^{-} - \vec{S}_h, \tag{4.16}$$

where $\boldsymbol{I}$ is the identity matrix. Therefore, for given partial currents $\vec{J}_h^{\pm}$ and volumetric source $\vec{S}_h$ in the heterogeneous node, the in-coming partial currents in the homogenized node can be determined by solving Eq. (4.16) iteratively as:

$$\begin{aligned} &\vec{J}_m^{-(0)} = \vec{J}_h^{-}, \qquad \vec{J}_m^{+(k+1)} = \boldsymbol{R}_m\vec{J}_m^{-(k)} + \vec{S}_h, \\ &\vec{J}_m^{-(k+1)} = \vec{J}_m^{+(k+1)} - \left(\vec{J}_h^{+} - \vec{J}_h^{-}\right), \quad k = 1,2,\cdots. \end{aligned} \tag{4.17}$$

Once the partial currents in the homogenized node are determined using given reference values in the heterogeneous node, the PCDFs can be deduced from Eq. (4.12). To generate PCDFs, VARIANT has been modified to solve Eq. (4.17) for each homogenized node with given reference partial currents and nodal flux. The volumetric source is internally calculated using homogenized cross sections and the reference flux.

Since PCDF is defined for each spatial and angular moment of partial currents, it can be applied to any angular approximation order in a consistent way. However, the determination of reference partial current moments in heterogeneous nodes can be non-trivial. For instance, if the reference heterogeneous problem is solved with the method of characteristics (MOC), the partial current moments must be evaluated from the spatial and angular distributions of angular fluxes at nodal interfaces using the trial functions of VARIANT. In this work, the reference nodal fluxes

and surface partial currents are obtained with Serpent MC simulations. Even though the functional expansion tally capability is available in Serpent, it is limited to tallying the distributions of scalar flux and reaction rates in Cartesian or cylindrical geometry and it is recommended to be applied to homogeneous material regions. Thus, only node-averaged flux and surface-averaged partial currents are tallied by Serpent for the time being, and PCDFs are generated only for the zeroth (flat) moments of partial currents. Nonetheless, node-averaged reaction rates and surface-integrated leakages are preserved once the core calculation is consistently performed with the same options used to generate PCDFs. That it, only the flat partial current moment is adjusted by PCDF in transport calculations and the high-order moments are assumed to be continuous at nodal interfaces.

4.2.3 Incorporation of PCDF in VARIANT

The incorporation of PCDFs in VARIANT is accomplished by modifying the nodal interface condition. As depicted in Figure 4.13, the application of PCDFs to the discontinuous partial currents (solid arrows) of two adjacent homogenized nodes make them match the reference partial currents (dotted arrows) of the corresponding heterogeneous nodes, which are continuous across the interface. In the original formulation without PCDFs, the system of nodal response matrix equations is solved iteratively with the following continuity condition of partial currents on the left (L) and right (R) side of an interface:

$$J_R^- = J_L^+, \quad J_L^- = J_R^+. \tag{4.18}$$

In the modified formulation with PCDFs, the interface conditions become

$$J_R^- = \frac{f_L^+}{f_R^-} J_L^+, \quad J_L^- = \frac{f_R^+}{f_L^-} J_R^+. \tag{4.19}$$

The implementation of Eq. (4.19) requires no changes to the red-black iteration scheme of VARIANT other than adjusting the incoming partial currents by PCDF ratios before applying the

response matrix. Again, the current implementation applies PCDF only to the flat moments of partial currents.

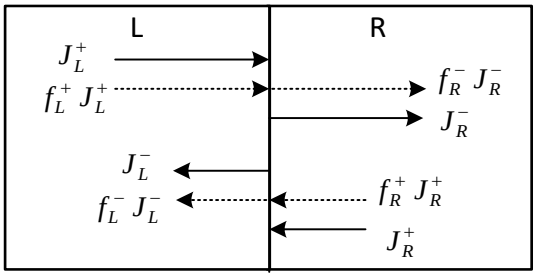

Figure 4.13 Nodal Interface Conditions Modified with PCDFs [118]

Using the relation between partial currents and surface fluxes, the even-parity discontinuity factor (f^e) for an even-parity flux moment i on surface γ can be determined as:

$$f_\gamma^e = \frac{J_{h,\gamma,i}^+ + J_{h,\gamma,i}^-}{J_{m,\gamma,i}^+ + J_{m,\gamma,i}^-}. \tag{4.20}$$

In the P_1 approximation, the EPDFs are equivalent to the conventional flux discontinuity factors. To incorporate EPDF into VARIANT, the nodal interface condition should be modified as:

$$\begin{aligned} J_R^- &= \frac{2f_L^e}{f_L^e + f_R^e} J_L^+ + \frac{f_L^e - f_R^e}{f_L^e + f_R^e} J_R^+, \text{ and} \\ J_L^- &= \frac{2f_R^e}{f_L^e + f_R^e} J_R^+ + \frac{f_R^e - f_L^e}{f_L^e + f_R^e} J_L^+. \end{aligned} \tag{4.21}$$

Compared to Eq. (4.19), the interface condition given by Eq. (4.21) requires altering the efficient red-black iteration scheme of VARIANT as the incoming partial currents depend on the outgoing partial currents from the same node. Because of this, PCDF is preferred over EPDF to be incorporated in VARIANT.

4.2.4 Use of PCDF in Transport Calculation

In Chapter 3, we showed that PCDF would reproduce the reference solution regardless of transport approximation order. Another test performed in Ref. [124] showed that even with

multigroup XSs generated in approximate models, the PCDFs obtained with the reference nodal flux and partial currents reproduced the reference solution. Discontinuity factor was originally designed to treat assembly heterogeneity effects. The discretization error is implicitly accommodated and with that one-mesh-per-assembly finite difference diffusion solution could match the reference heterogeneous solution. Then a natural question is why we are pursuing high-order transport calculations with discontinuity factor. As pointed out by Smith [125], discontinuity factors are now used to correct not only the homogenization error, but also the other deficiencies of nodal calculation models, such as the low-order transport approximation, coarse spatial discretization, and sometimes cross section errors. This is the reason the nodal model should be made to capture as many physics effects as possible, except local heterogeneity. Otherwise, discontinuity factors are nothing but lumped fudge factors, which cannot guarantee the solution accuracy when they are applied to a core model that is different from the setup on which they are generated.

Using the heterogeneous CFTR-1D problem, the PCDFs for the thermal fuel assembly generated with diffusion and higher-order transport options are compared in Figure 4.14. On the left of the thermal assembly is the buffer assembly and on the right the graphite reflectors. Except for one case, these PCDFs were generated using the reference 13G cross sections from Serpent and replaced anisotropic scattering matrices from MC^2-3. It is seen that with increased approximation orders for angular flux expansion and anisotropic scattering, the PCDFs approach asymptotic values. The difference between diffusion (P1_P0) and transport approximations is larger than that between different transport approximations. As expected, the increased scattering order makes the biggest differences in high-energy groups because scattering anisotropy is more pronounced in the fast energy range. The use of inconsistently weighted anisotropic scattering

induces less deviation in PCDFs than the diffusion approximation does. The "convergence" behavior of PCDFs can be seen more clearly in Figure 4.15, where the PCDFs for the incoming partial currents on the left surface of the thermal assembly are plotted against increasing transport approximation order. In some sense, the "converged" PCDFs represent the discontinuity conditions purely due to intra-assembly heterogeneity. The convergence property is favorable because further refinement of approximation orders in VARIANT transport calculations can be applied without regenerating PCDFs.

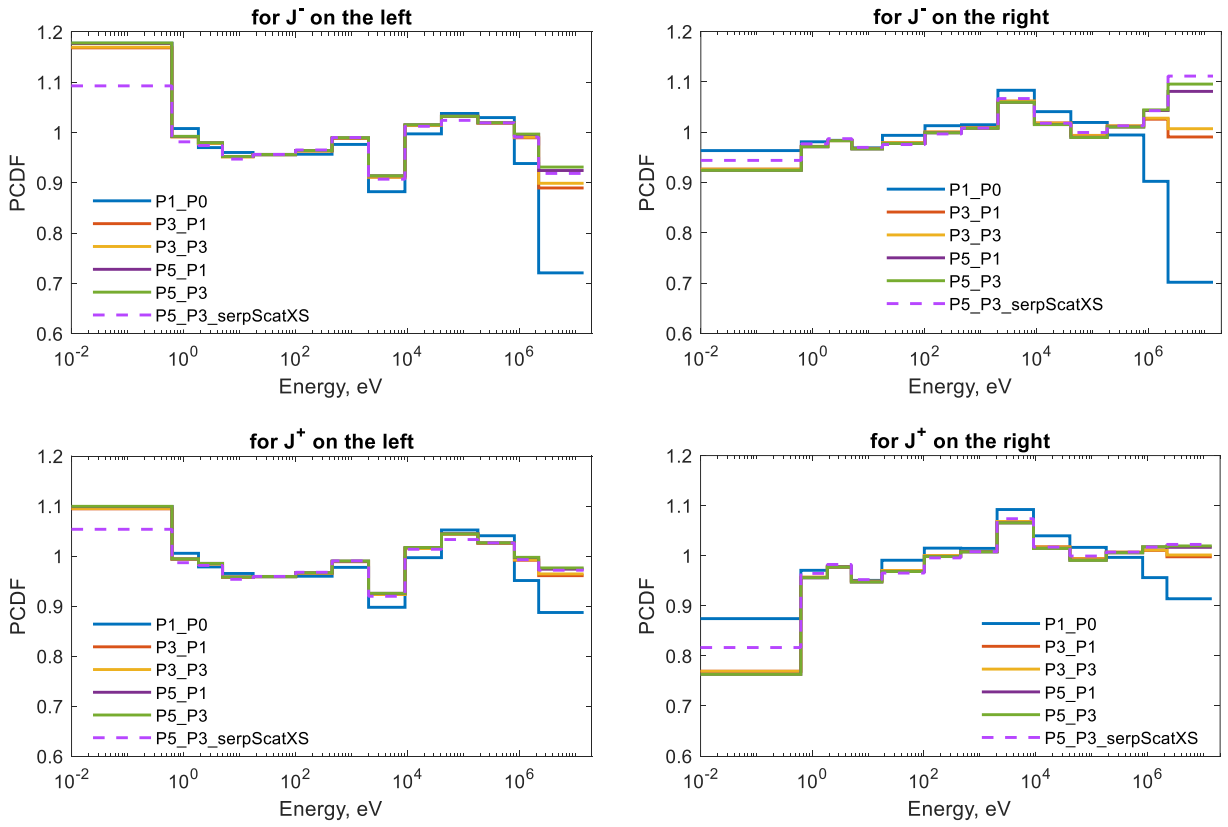

Figure 4.14 PCDFs Obtained with Different Flux Expansion and Scattering Orders on Left and Right Boundaries of Thermal Assembly in CFTR-1D Problem

Another test was performed for CFTR-1D by applying unity PCDFs to the graphite reflectors which are already homogenized in the Serpent model. The VARIANT diffusion and

transport calculation results are compared in Table 4.2, where GR1, GR2, and GR3 label the three graphite reflector assemblies and GR1 is next to the thermal fuel assembly as shown in Figure 3.4. It is seen from Table 4.2 that the transport calculations with unity PCDFs for reflectors produced more accurate eigenvalue and assembly powers than the diffusion calculations. For large problems with near homogeneous reflector regions, the use of PCDFs may be unnecessary in transport calculations, while PCDFs are necessary to correct the error induced by low-order transport approximations in diffusion calculations.

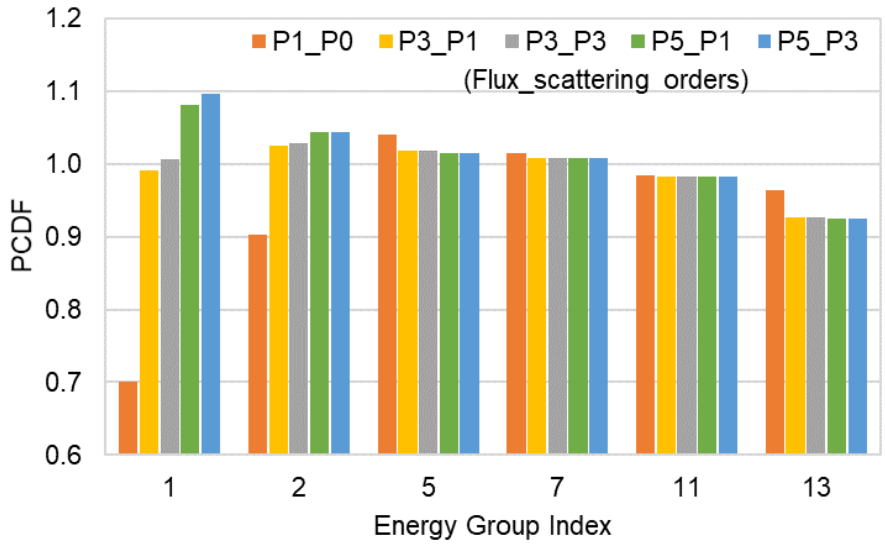

Figure 4.15 "Convergence" of PCDF with Increasing Transport Order

Table 4.2 VARIANT solutions obtained with different PCDFs for reflectors in CFTR-1D

Transport order	Use of PCDFs	Δk, pcm	Assembly power error	
			FA	TA
P_1 diffusion	Applied to all assemblies	2	0.00%	0.00%
	Not for GR1 / GR2 / GR3	-55	-0.36%	0.32%
	Not for GR2 / GR3	40	-0.08%	0.07%
P_5 / P_3 transport	Applied to all assemblies	-1	0.01%	-0.01%
	Not for GR1 / GR2 / GR3	-24	-0.25%	0.22%
	Not for GR2 / GR3	20	0.00%	0.00%

4.2.5 Generation of PCDF

PCDFs are generated by solving Eq. (4.17) for each node to be homogenized. This calculation is practically node wise if the partial current moments in the heterogeneous nodes are known from some reference calculation. From the practical point of view, approximate models must be used for the reference heterogeneous calculations. In the following subsections, the one-node and multi-node calculation procedures with given reference nodal flux and partial currents are first described. Then the approximate models used to perform the reference heterogeneous calculations are discussed.

4.2.5.1 One-node Calculation

When all the partial current moments of reference solution are given, Eq. (4.17) is directly solved for each node. All nodes are decoupled and hence it is called one-node calculation. However, since the heterogeneous solution is obtained in MC simulation with Serpent, only flat moments of partial currents and nodal average flux are tallied. Regarding nodal calculations, it is acceptable to use only the average flux for preserving average reaction rates. When homogeneous partial currents are iteratively determined, the intra-nodal flux distribution (i.e., the high-order flux moments) will be updated to preserve the surface leakage while the average flux level is forced to the reference value. But the high-order partial current moments are explicitly included in Eq. (4.17). Without the reference high-order partial current moments, the flat leakage approximation is applied in one-node calculations. Thus, the average incoming partial currents are imposed in the normal inward direction at each surface and the high-order moments of the resulting outgoing partial currents are neglected in the next iteration. In core calculations, PCDFs should be used with the same flat leakage approximation.

At a vacuum boundary surface γ, the reference incoming partial current ($J^-_{h,\gamma}$) is zero. Physically, the incoming partial current through surface γ of the homogenized node should also be zero. According to Eq. (4.11), the outgoing partial current at surface γ should be:

$$J^+_{m,\gamma} = J^+_{m,\gamma} - J^-_{m,\gamma} = J^+_{h,\gamma} - J^-_{h,\gamma} = J^+_{h,\gamma}, \tag{4.22}$$

which makes the problem over-determined because $J^+_{m,\gamma}$ is also determined by Eq. (4.10). In this situation, $J^-_{m,\gamma}$ on surface γ is forced to zero and the constraint of Eq. (4.11) is released. Instead, the net leakage out of the homogenized node through surface γ is determined as:

$$J_{\gamma,net} = f^+_\gamma J^+_{m,\gamma} = J^+_{h,\gamma}. \tag{4.23}$$

Theoretically, no negative PCDF will be produced unless the problem is ill-posed because neither the heterogeneous nor the homogenized model produces negative partial current solution. An example of the ill-posed condition is when MC tallied thermal group fluxes and partial currents of the fast-zone assemblies in CFTRs bear large uncertainties. Because of numeric errors, the near-zero reference partial currents of heterogeneous nodes can lead to negative values in the one-node calculation to generate PCDFs. In this case, the one-node calculation is skipped for low-energy groups and PCDFs are set to one to avoid numerical instability in core calculations.

4.2.5.2 Multi-node Calculation

The one-node calculation requires the flat leakage approximation, which is unphysical in transport calculations. Figure 4.16 shows the flux distributions in CFTR-1D of the VARIANT transport solutions obtained with ("_flatJ" case) and without the flat leakage approximation. It is seen that the flat leakage approximation could distort the intra-nodal flux distribution although the average flux and net leakage are preserved. To eliminate the flat leakage approximation, multi-node calculations can be performed for PCDF generation. Eq. (4.17) is solved in supercell models, where the reference nodal flux and surface partial currents are imposed only on the central node

of interest. During iteration, the surface-averaged net leakage of the reference solution is preserved while the high-order moments are iteratively determined by imposing the outgoing partial currents of neighbor nodes as incoming partial currents. The iteration terminates when the average partial currents are converged. Typically, the same supercell model for multigroup cross section generation can be used for multi-node calculations. The multi-node calculation is essentially one-node calculation because the multiple nodes are not directly coupled through continuous interface conditions.

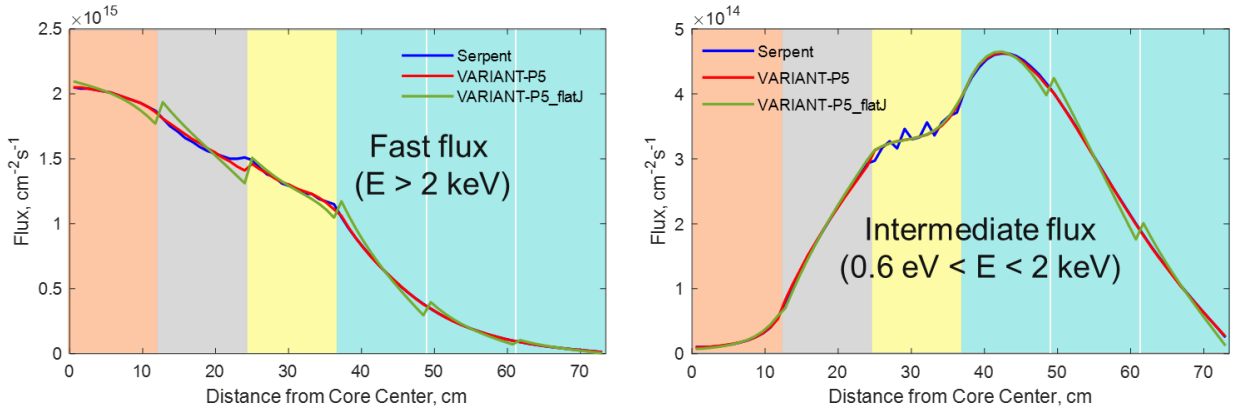

Figure 4.16 Impact of Flat Leakage Approximation on Intra-nodal Flux Shape

4.2.5.3 Approximate Models for PCDF Generation

In principle, the reference heterogeneous solution can be reproduced in a homogenized calculation using the PCDFs determined from the reference partial currents and volumetric sources of the original heterogeneous problem. But the reference heterogeneous solution cannot be known *a priori* and PCDFs must be determined approximately. For instance, the conventional assembly discontinuity factors (ADFs) are determined as surface-to-average flux ratios in assembly lattice calculations with reflective boundary conditions (BCs). This approximation was based on the observed insensitivity of ADFs to the assembly location in the core [51] and was acceptable for large commercial LWRs, where similar fuel assemblies are loaded.

Analogous to ADFs, PCDFs can be approximately computed with information from assembly lattice calculations. With reflective BCs, the flux distribution in the homogenized assembly is flat and is required to match the average flux level in the heterogeneous assembly. The flat moments of partial currents ($J^{\pm}_{m,\gamma,0}$) of surface γ of the homogenized node are of the same magnitude and can be determined as:

$$J^{+}_{m,\gamma,0} = J^{-}_{m,\gamma,0} = \frac{\phi_{m,\gamma}}{4} = \frac{\bar{\phi}_m}{4} = \frac{\bar{\phi}_h}{4}, \tag{4.24}$$

where $\phi_{m,\gamma}$ is the flux of surface γ of the homogenized node, $\bar{\phi}_m$ and $\bar{\phi}_h$ are the node-averaged fluxes in homogenized and heterogeneous assemblies, respectively. Thus, the PCDFs of surface γ are simply given by

$$f^{\pm}_{\gamma,0} = 4\frac{J^{\pm}_{h,\gamma,0}}{\bar{\phi}_h} = \frac{\bar{\phi}_{h,\gamma}}{\bar{\phi}_h}, \tag{4.25}$$

where $\bar{\phi}_{h,\gamma}$ is the reference flux of surface γ in the heterogeneous node. That is, the infinite lattice approximation leads to the same PCDF value for incoming and outgoing partial currents and the value is equal to the conventional ADF.

The infinite assembly lattice approximation might be useful for those surrounded by similar assemblies. For general applications, discontinuity factors should be determined for nonzero surface leakage. Like multigroup cross section generation, the generation of PCDF is primarily based on supercell models for coupled fast-thermal spectrum reactors. Unlike cross section generation, which relies on the representative volume-averaged spectrum, PCDFs are defined on individual surfaces and hence are more sensitive to the BCs imposed on supercells as the change of environment will change the relative magnitude of surface currents. The strategies to treat the long-range environment impacts on PCDF generation are discussed in the following subsections.

4.2.5.4 PCDF Generation with Fixed Source Calculation

In Ref. [118], we developed a method to obtain approximate BCs for heterogeneous supercell models from a full core calculation with homogenized multigroup XSs and unity PCDFs and to use them in supercell fixed source calculations for PCDF generation. This method can be schematically illustrated in Figure 4.17.

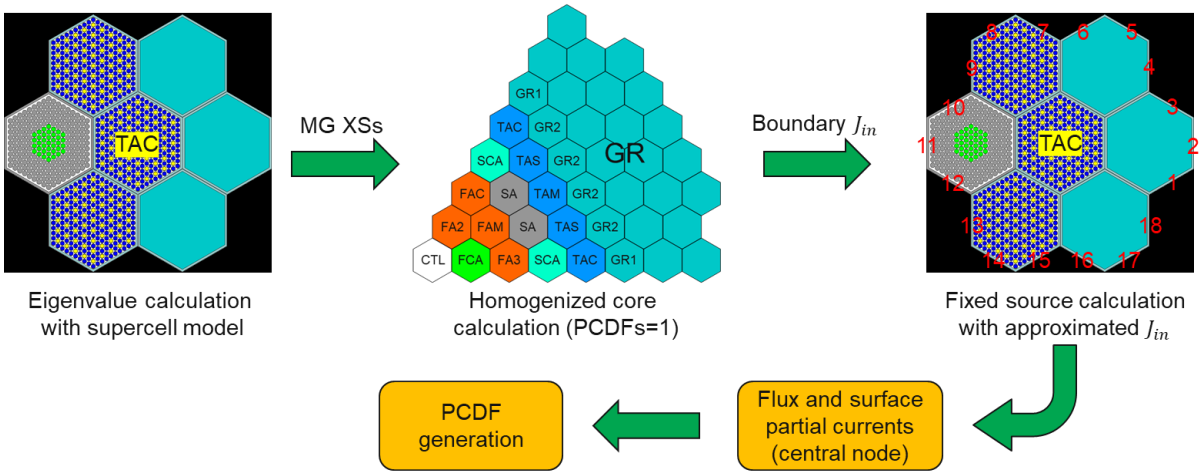

Figure 4.17 PCDF Generation with Combined Homogenized Core and Fixed Source Supercell Calculations [118]

First multigroup XSs are generated in supercell models. Then a nodal core calculation is performed with unity PCDFs to obtain nodal interface partial currents. These partial currents would be more appropriate to represent the core environment than arbitrarily assumed BCs for supercell models as shown in Figure 4.18 for the partial current spectrum on an interface between fuel and reflector assemblies in a coupled-spectrum reactor. Using the incoming partial currents as external surface sources, fixed source supercell calculations are performed with vacuum BCs. The fixed source lattice calculation is performed with Serpent, for which flat incoming partial currents are applied to the boundary surfaces in the normal inward direction. This is to simplify the source sampling process in MC simulations. The use of supercell model reduces the impact of neglecting source distributions in space and angle. To be consistent with the core condition, the fission source

is divided by the k_{eff} value of the nodal core calculation. Then PCDFs are calculated using the tallied node-averaged flux and surface partial currents in the fixed source simulation. A finer multigroup representation of the boundary condition is supposed to yield more accurate PCDFs. The fine-group incoming partial currents can be obtained either with a fine-group core calculation, or by other approximated means such as modal synthesis of fine-group solutions of lattice calculations and the broad-group solution of the core calculation.

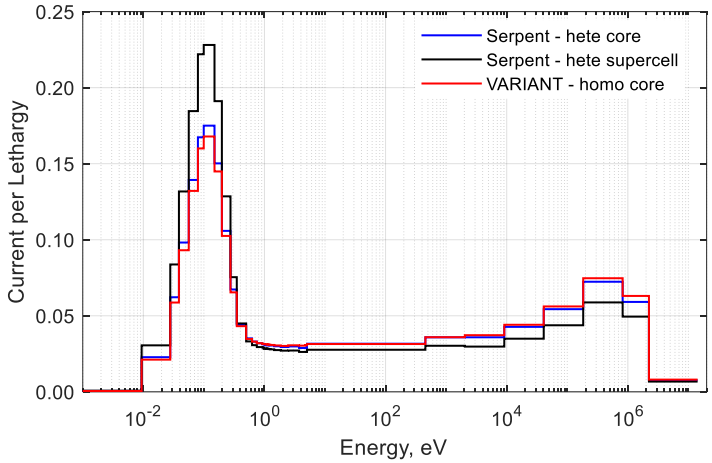

Figure 4.18 Spectrum Comparison of Incoming Partial Currents from Reflector to Fuel [118]

4.2.5.5 Imbedded PCDF Correction in Core Calculation

Using fixed source Monte Carlo simulation for PCDF generation was proved to be a reliable approach in steady state transport calculations [118]. However, it is also shown that a good approximation of the boundary condition is essential to produce accurate PCDFs. The best approximation is obtained from the homogenized nodal core calculation. Instead of repeating homogenized core calculation and local heterogeneous supercell calculations, an approach to generate PCDFs on the fly during core calculation is more desirable. This is because the core configuration keeps evolving in the design phase, and it changes with fuel depletion (and other variations of state parameters). It is not feasible to obtain the approximate BCs for fixed source

calculations in advance. There are many studies in this field that pursues functionalization of homogenized cross sections and nodal equivalence parameters with leakage BCs. [126-128] The difficulty of extending these ideas to fast or coupled-spectrum systems is that since more energy groups are used, more data points are needed to fit the cross section and discontinuity factors with the selected parameters (e.g., current to flux ratio or albedo) to represent BCs.

Given that local boundary conditions could be well approximated using nodal full-core solutions, a natural pathway to treat the environmental effects is to re-generate PCDFs in core calculations. We consider the four neutron balances to be satisfied by the same node at the local heterogeneous and homogenized supercell conditions and global heterogeneous and homogenized core conditions:

$$\vec{J}^{+}_{L,h} = \vec{S}_{L,h} + \boldsymbol{R}_m \vec{J}^{-}_{L,h}, \tag{4.26}$$

$$\vec{J}^{+}_{h,m} = \vec{S}_{L,m} + \boldsymbol{R}_m \vec{J}^{-}_{L,m}, \tag{4.27}$$

$$\vec{J}^{+}_{G,h} = \vec{S}_{G,h} + \boldsymbol{R}_h \vec{J}^{-}_{G,h}, \tag{4.28}$$

$$\vec{J}^{+}_{G,m} = \vec{S}_{G,m} + \boldsymbol{R}_m \vec{J}^{-}_{G,m}, \tag{4.29}$$

where the subscript G denotes the global core calculation results, L the local supercell calculation results, h the quantities in heterogeneous calculations, and m the quantities in homogenized calculations. Equations (4.26) and (4.27) are solved in supercell calculations when PCDFs are generated. Eq. (4.29) is satisfied in the nodal core calculation. With these known relations, we would like to approximate the neutron balance given by Eq. (4.28).

The change in neutron balance from local to global conditions occurs both in volumetric source and surface dependent partial currents. The change in volumetric source is further due to the change in reactivity and global flux gradient. It is assumed that this effect perturbs the heterogeneous and homogenized nodal balance by the similar amount. Without repeating the local

heterogeneous calculation as we do in Section 4.2.5.4, the perturbation of boundary conditions for the heterogeneous node is approximated as the differences in partial currents of the homogenized node between local and global calculations:

$$\Delta J^{+} = J^{+}_{G,h} - J^{+}_{L,h} \approx J^{+}_{G,m} - J^{+}_{L,m}\,, \tag{4.30}$$

$$\Delta J^{-} = J^{-}_{G,h} - J^{-}_{L,h} \approx J^{-}_{G,m} - J^{-}_{L,m}\,. \tag{4.31}$$

Because the local partial currents are normalized to have the same nodal average flux as the reference heterogeneous supercell calculation, which is generally different from the flux level emerging in the global calculation, the local quantities in Eqs. (4.30) and (4.31) need to be renormalized before taking the difference. Without a better theoretical basis, the renormalization is made to have the same integrated volumetric source in a node. The approximate nodal balance for the heterogeneous node in the core condition is:

$$\vec{J}^{+}_{G,h} \approx J^{+}_{L,h} + \Delta J^{+} \approx \vec{S}_{G,m} + \boldsymbol{R}_h\left(\vec{J}^{-}_{L,h} + \Delta J^{-}\right). \tag{4.32}$$

The perturbed heterogeneous partial currents are used to re-generate PCDFs for core calculations.

The above approximation does not have any good theoretical basis as the heterogeneous partial currents in global full-core and local supercell environments do not have direct correlations. To "know" the response of a heterogeneous node to given incoming partial currents, we need to have the response matrix $\boldsymbol{R}_h$ for it. The response matrices can be pre-generated for each type of heterogeneous node and used in the global core calculation to predict the heterogeneous partial currents. This approach was not adopted because of its two major deficiencies. First is the computational cost to generate response matrices, which is proportional to the number of energy groups, nodal surfaces, and state conditions. The other concern is the dependence of response matrices on the spatial and angular distribution of multigroup incoming partial currents.

4.2.6 Intra-nodal Flux and Power Reconstruction

Nodal core calculations do not reproduce the intra-nodal flux distribution in heterogeneous nodes. To obtain spatially detailed reaction rates and power distributions and to predict pin-wise fuel depletion, the flux distribution in a heterogeneous node can be reconstructed by combining the smooth flux shape from the global nodal solution and pin flux form functions (PFFFs) to incorporate local heterogeneity effects. Since VARIANT uses multivariate polynomials for spatial expansion of flux distribution within each node, the pin fluxes of the homogenized core calculation can be simply evaluated using the basis polynomials and corresponding expansion coefficients. The flux form function of group g for pin k is defined as the ratio of reference pin flux in the heterogeneous node to that in the homogenized node,

$$\mathrm{PFFF}_g^k = \frac{\bar{\phi}_{h,g}^k}{\bar{\phi}_{m,g}^k}, \tag{4.33}$$

where $\bar{\phi}_{h,g}^k$ is the average flux of group g at pin k obtained from the reference heterogeneous assembly calculation, and $\bar{\phi}_{m,g}^k$ is the average flux of group g evaluated at pin k from the polynomial flux shape of the VARIANT one-node solution for PCDF generation. With reconstructed pin fluxes, the pin power distributions in heterogeneous nodes can be determined by summing the products of flux and heating cross section over all energy groups. For pin power reconstruction, we can also define the pin power form functions (PPFFs) by the ratio of reference pin powers in heterogeneous calculation to those computed with homogeneous fluxes,

$$\mathrm{PPFF}_k = \frac{\sum_g \left[H_{h,g}^k \bar{\phi}_{h,g}^k\right]}{\sum_g \left[H_{m,g}^k \bar{\phi}_{m,g}^k\right]}, \tag{4.34}$$

where the heating cross sections $H_{h,g}^k$ and $H_{m,g}^k$ are the products of neutron reaction cross section and kinetic energy released per reaction.

4.3 Full-Core Depletion Calculation

As demonstrated in Section 3.3, the current REBUS-3 code can be applied to coupled-spectrum reactor analysis with a few improvements in burnup dependent cross section usage, representation of fission yields depending on incident neutron energy, and use of burnup dependent PCDFs in nodal core calculations. The code modifications to fulfill these needs are discussed in the following subsections.

4.3.1 Burnup Dependent Isotopic Cross Section

The current REBUS-3 can utilize burnup dependent capture and fission cross sections, which are fitted with the number density of user specified reference nuclides. To utilize variable isotopic cross sections for all reaction types depending on state parameters such as burnup, temperature, and moderator density, a new cross section dataset VARIXS (Variable Isotopic Cross Sections) was defined based on the CCCC (Committee on Computer Code Coordination) standard isotopic cross section file format ISOTXS [97]. One can think of VARIXS as nested ISOTXS's with state parameters. These parameters are not fixed but specified by user when generating the VARIXS dataset for specific reactor system. They are used only for interface purpose such that the stored cross section data can be correctly interpreted in REBUS-3. In REBUS-3, the tabulated cross sections are used through piecewise linear interpolation. For more information of VARIXS, one can refer to Appendix C.

The REBUS-3 code was modified to utilize the state dependent isotopic cross sections provided with VARIXS. A new module was added to REBUS-3 for cross section interpolation at each depletion step. The major modification to the computational flow of REBUS-3 is shown in Figure 4.19. At each depletion step, the isotopic cross sections are re-evaluated by performing multi-dimensional linear interpolation of the VARIXS data according to the updated state

parameters. For the time being, only burnup state is considered. The determination of other state parameters, such as fuel temperature and moderator density, requires a thermal-hydraulic calculation module to be implemented in REBUS-3. The updated cross sections are used in VARIANT transport calculations and in burn matrix construction for depletion calculation. This iteration is terminated when the change of nuclide densities in successive iterations is smaller than the user specified convergence criterion and is repeated at the next time step.

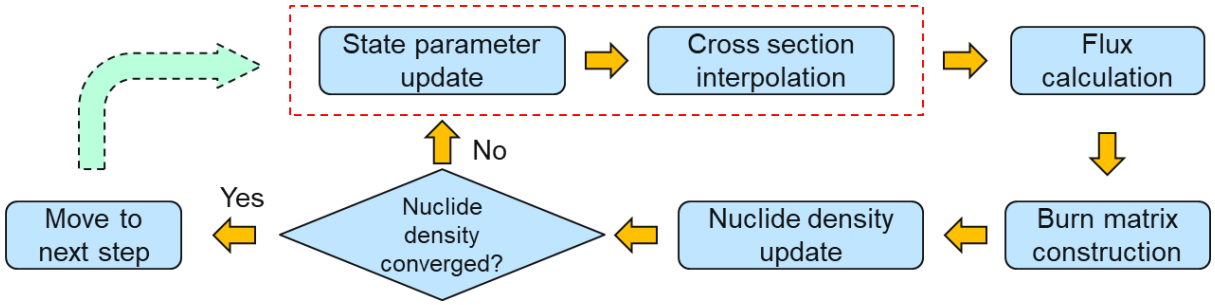

Figure 4.19 Modified Region Density Iteration for Depletion Calculation in REBUS-3

4.3.2 Energy Dependent Fission Yield

As tested in Chapter 3, the dependence of fission yields on incident neutron energy needs to be considered in depletion calculations for coupled-spectrum reactors because of the existence of distinct flux spectra in fast and thermal spectrum zones. The REBUS-3 code is modified to construct burn matrices using energy dependent fission yield data, which are interpolated in specific depletion zones with the average fission energy. The average fission energy ($\bar{E}_f^{k,i}$) for actinide i in depletion zone k is computed as:

$$\bar{E}_f^{k,i} = \frac{\sum_g \bar{E}_g \sigma_{f,g}^{k,i} \bar{\phi}_{k,g}}{\sum_g \sigma_{f,g}^{k,i} \bar{\phi}_{k,g}}, \tag{4.35}$$

where $\bar{E}_g$ is the average neutron energy of group g, $\sigma_{f,g}^{k,i}$ is fission cross section, and $\bar{\phi}_{k,g}$ is average group flux in zone k.

4.3.3 Burnup Dependent PCDF

Burnup dependent PCDFs are generated with Serpent supercell depletion calculations. At each burnup state, one-node or multi-node calculations are performed to produce PCDFs and the single-state PCDFs are then functionalized with burnup. In REBUS-3 calculations, the burnup dependent PCDFs are first linearly interpolated with burnup and then corrected according to the surface partial currents from nodal core calculation with VARIANT. A special case is that for nonfuel assembly, which does not have burnup state, the burnup dependent PCDFs are not generated as the constant macroscopic cross sections are used. The variation of PCDFs due to environmental change is approximately considered with the imbedded PCDF correction in core calculations.

4.4 Overall Procedure for Core Calculations

The overall computational procedure for coupled-spectrum reactor analysis is summarized in Figure 4.20. Starting with Serpent supercell depletion calculations, burnup dependent multigroup XSs and PCDFs are generated based on standard MC tallies and one-node/multi-node VARIANT calculations. With these XSs and PCDFs, REBUS-3 whole core depletion calculations are performed using VARIANT as the flux solver. At each burnup step, multigroup XSs and PCDFs are first interpolated according to burnup states and then used in VARIANT nodal transport calculations. The PCDFs can also be corrected during the nodal core calculation. With converged fluxes and interpolated isotopic cross sections, the burn matrix is constructed for each depletion zone and the nuclide depletion calculation is performed. The region density iteration algorithm is used for time stepping. The depletion calculation and flux calculation are iterated until the nuclide densities converge or the allowed maximum number of iterations is reached. After each depletion calculation, the burnup state is updated for XS and PCDF interpolation in the next time step.

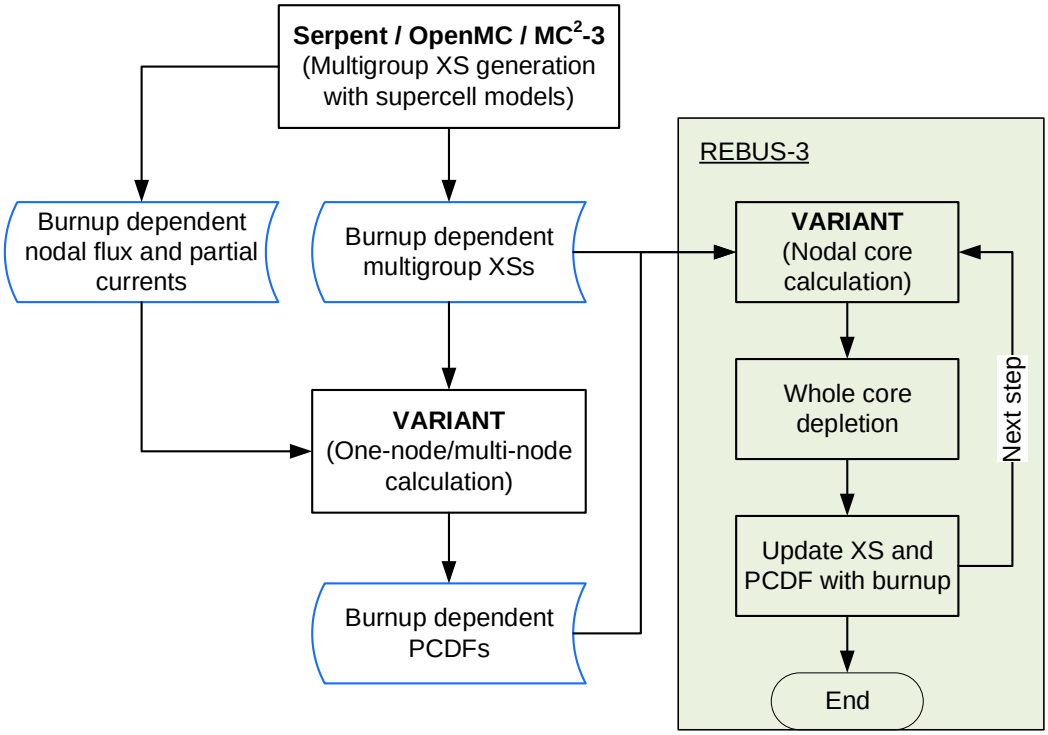

Figure 4.20 Overall Computational Procedure for CFTR Analysis

Chapter 5

Whole-Core Transport Calculation Test

The proposed core calculation method was tested using a 2D coupled fast-thermal reactor (CFTR-2D) problem derived from the low-enriched uranium core design of VCTR [11]. This chapter is focused on the test of the steady-state VARIANT transport analysis method with PCDFs. The multigroup cross section generation method with supercell was first examined. Then, the performance of PCDFs was evaluated in both nodal diffusion and transport calculations.

5.1 CFTR-2D Problem

As shown in Figure 5.1, the CFTR-2D core consists of three subzones: the inner fast spectrum zone, the outer thermal spectrum zone, and a buffer zone in between that acts as reflector of the fast zone and filters out thermal neutrons from the thermal zone. Inside the fast zone are 15 fuel assemblies, three control assemblies, and a central test loop.

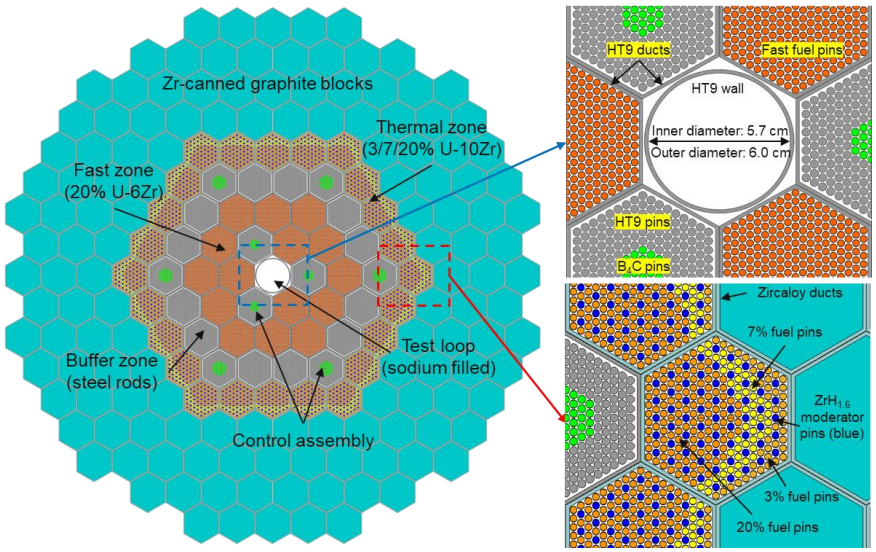

Figure 5.1 Core Configuration of 2D Coupled Fast-Thermal Spectrum Reactor

Each fast fuel assembly contains 271 fuel rods of U-6wt%Zr (U-6Zr) alloy, in which uranium is 19.95 at.% enriched in U-235. The control assembly in the fast zone consists of 198 steel dummy pins and 19 control rods. The absorber material used for the control rods is 19.90 at.% enriched (in B-10) boron carbide (B_4C). The buffer zone includes 12 steel reflector assemblies and 6 control assemblies. The thermal zone contains 24 fuel assemblies, each of which is composed of 210 U-10wt%Zr (U-10Zr) fuel rods and 61 zirconium hydride ($ZrH_{1.6}$) moderator pins. To reduce local power peaking due to returned thermal neutrons from the graphite reflector, three fuel enrichments (3.0 / 7.0 / 19.95 at.%) are used for thermal fuel pins. Each of the six thermal assemblies located at corners contains 117 pins of 19.95% enriched fuel, 51 pins of 7 at.% fuel, and 42 pins of 3 at.% fuel. Each thermal assembly on the side contains 147 pins of 19.95% fuel, 37 pins of 7 at.% fuel, and 26 pins of 3 at.% fuel. The low-enriched (3 at.%) fuel pins are arranged outwards facing the graphite reflectors while the 19.95 at.% enriched fuel pins are loaded next to the buffer zone. Outside the active core are graphite blocks canned in zircaloy as thermal reflectors. All assemblies are arranged in a triangular lattice with a 12.245 cm assembly pitch. Detailed geometric and compositional specifications of these assemblies are provided in Table A.3 of Appendix A. The CFTR-2D core is cooled by sodium. For the benchmarking purpose, a material temperature of 600 K is assumed for all components except for fuel, which is set to 900 K.

A full-core Serpent calculation was performed for CFTR-2D using the ENDF/B-VII.1 library. 2,000 active cycles with 100,000 neutron histories per cycle were simulated to obtain assembly powers with less than 0.1% statistical uncertainties. Figure 5.2 shows the core model of homogenized assemblies used for VARIANT nodal transport calculations. The labels in Figure 5.2 define unique cross section regions determined by assembly types and their positions. The homogenized multigroup XSs were generated in 13 energy groups.

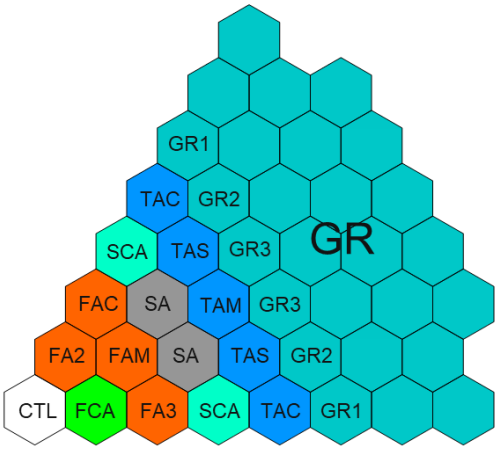

Figure 5.2 Assembly Homogenized 1/6 Core Model of CFTR-2D and Unique Assembly Types for Multigroup XS Generation

5.1.1 Cross Section and PCDF Generation

The Serpent full-core simulation of CFTR produced distinct neutron flux spectra in various assemblies as shown in Figure 5.3. Typical fast reactor spectrum is produced in the fast zone while transitional spectra occur in the buffer and thermal fuel assemblies. It turns out the thermal fuel assemblies are highly under moderated, resulting in a spectrum more like fission spectrum plus a thermal flux tail. Neutron moderation is dominantly provided by the graphite reflectors, where a large thermal flux peak is seen.

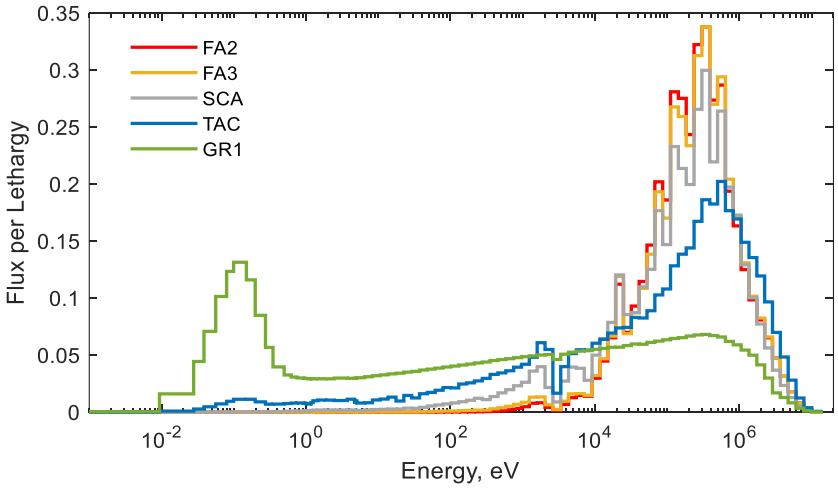

Figure 5.3 Flux Spectra of Individual Assemblies in CFTR-2D Core at BOC

The significant spectral transition in the CFTR-2D core implies that the infinite lattice calculation for each type of assembly will not produce dependable multigroup XSs for core calculations. To generate multigroup XSs with reduced models, supercell models were prepared for unique assembly types. Figure 5.4 shows three examples of the supercell models used for outer fast fuel assembly and thermal fuel assemblies. Reflective boundary conditions were imposed on the fast assembly supercell model, where part of thermal assembly is included to provide thermal neutron source. The local moderator to fuel ratio is modified by including only 7.0 at.% fuel pins were included in this part of thermal assembly such that the contribution of graphite moderation can be approximately considered. For the thermal assembly supercell models, non-uniform boundary conditions were imposed. The graphite density in reflector was doubled to preserve optical thickness in the reduced problem domain. For the inner fast zone, a supercell model with fixed source as shown in Figure 5.5 is used to generate multigroup XSs. The supercell model for graphite reflectors is shown in Figure 5.6, where vacuum condition is applied on the right and the other three boundaries are reflective.

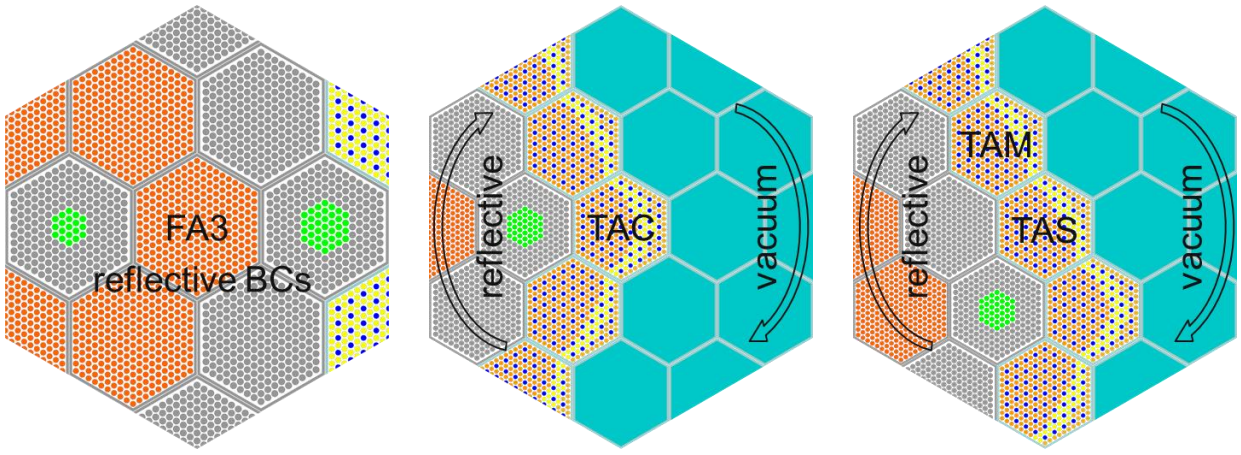

Figure 5.4 Supercell Models for Multigroup XS Generation for Fuel Assemblies
(The graphite density in two thermal assembly supercells were doubled)

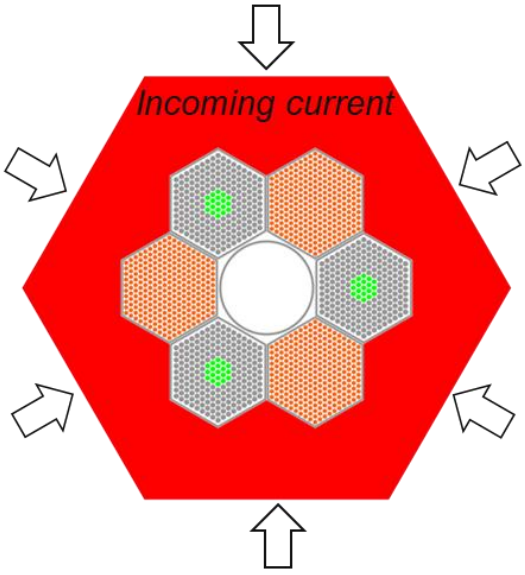

Figure 5.5 Supercell Fixed Source Calculation Model for Inner Fast Zone

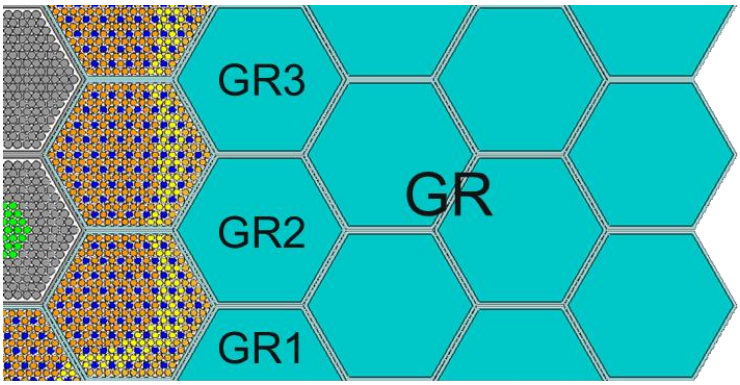

Figure 5.6 Supercell Model for Graphite Reflectors

In Figure 5.7, the 13G cross sections generated in Serpent supercell calculations are compared to the reference cross sections tallied in the full-core model. The statistical uncertainty (1σ) of cross section tally is less than 0.3% for thermal assemblies, and less than 0.7% for fast assemblies. It is shown that Serpent supercell calculations produced accurate broad-group XSs for thermal assemblies. The maximum relative error is less than 1%. The low-energy group XSs for the fast assembly had more than 1% errors but there is hardly neutron flux below 100 eV in fast assemblies. These errors are expected not to induce noticeable errors in core calculations.

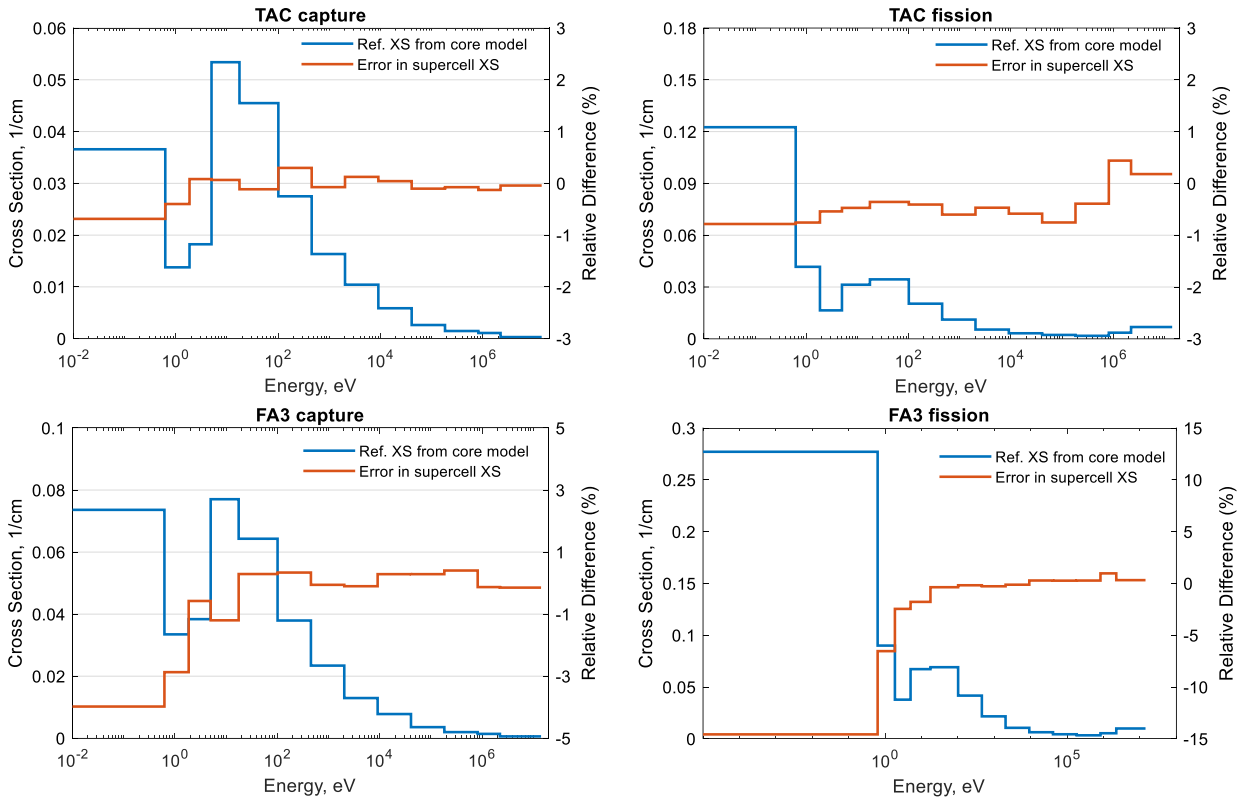

Figure 5.7 Error in 13G Cross Sections Generated with Supercell Models

For the inner fast region, the cross sections of low-energy groups are tallied with over 5% uncertainties. Nevertheless, they were accepted because of the reason just mentioned above. We care more about the cross sections in the energy range above 100 eV. Figure 5.8 shows that with the approximate surface source obtained from the thermal assembly supercell calculations, the broad-group cross sections for FA2 was significantly improved, especially between 100 eV and 1 keV. On the other hand, critical albedo search did not make noticeable improvements. Even though FA2 is located far from the thermal zone, the flux spectrum is still affected as shown in Figure 5.9.

Using these supercell models, PCDFs were generated for all unique assemblies except the outer reflectors that are not next to fuel assemblies, in one-node and multi-node calculations with P_1 diffusion and P_5 transport options, respectively. The one-node calculations were performed with the flat leakage approximation. For inner fast-zone assemblies, PCDFs for low-energy groups (E_n

< 100 eV) were set to one. These multigroup XSs and PCDFs were used in VARIANT nodal core calculations and the results are presented in the next section.

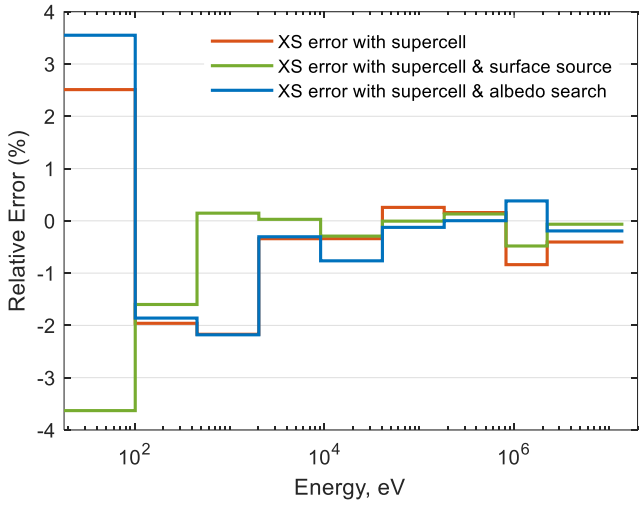

Figure 5.8 Error in 13G Cross Sections for FA2 Generated in Supercell Models

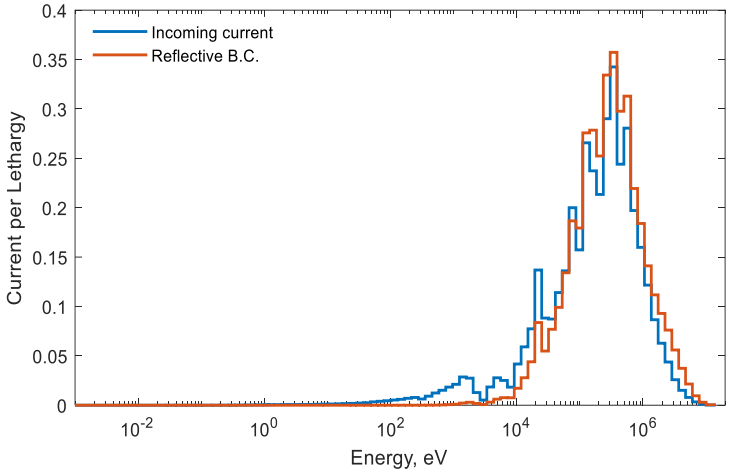

Figure 5.9 Flux Spectra in FA2 from Supercell Calculations with Different BCs

5.1.2 Core Calculation Results

The first calculation was performed with reference XSs and PCDFs obtained from the full-core simulation. The reference Monte Carlo solution of k-effective is 1.07598 ± 0.00004. The maximum statistical uncertainty (1σ) in the tallied assembly powers is 0.04%. For deterministic

power calculations, the energy release per fission is tallied for each unique fuel assembly type in Serpent simulations and used in VARIANT. The VARIANT diffusion and transport calculation results are compared in Table 5.1. Without PCDFs, neither diffusion nor transport produced accurate solution. The transport calculation resulted in better k-effective but the predicted assembly powers were not improved. This is because of the scalar flux weighted anisotropic scattering cross sections. With PCDFs, both diffusion and transport calculations produced satisfactory results with less than 200 pcm eigenvalue error and less than 0.3% errors in assembly powers. The transport results are noticeably more accurate than the diffusion results because PCDFs were not applied to the periphery reflector assemblies.

Table 5.1 VARIANT solutions with reference XSs and PCDFs for CFTR-2D problem

Transport order	Use of PCDFs	Δk, pcm	Assembly power error	
			rms	max
P_1 / P_0 diffusion	No	-1419	2.04%	3.11%
	Yes	199	0.16%	-0.28%
P_5 / P_3 transport	No	-958	2.25%	3.35%
	Yes	67	0.10%	-0.17%

Next the multigroup XSs and PCDFs generated in supercell calculations were tested. The corresponding results are summarized in Table 5.2, where the "PCDF correction" column denotes whether imbedded PCDF re-generation technique is applied during core calculations. Compared to the best achievable results given in Table 5.1, the VARIANT solutions obtained with supercell XSs and PCDFs contain non-negligible errors, especially the diffusion solution. The major error source should be the inaccurate PCDFs, because with PCDFs the supercell XSs led to similar results as the XSs tallied in the full core model. Nevertheless, the performance of imbedded PCDF correction is promising as both the eigenvalue and assembly power errors were reduced. In the transport calculation, the error reduction is more than half.

Table 5.2 VARIANT solutions with supercell XSs and PCDFs for CFTR-2D problem

Transport order	Use of PCDFs	PCDF correction?	Δk, pcm	Assembly power error	
				rms	max
P_1 / P_0 diffusion	No	-	-1424	2.23%	3.37%
	Yes	No	412	1.55%	-1.78%
		Yes	196	0.48%	-1.38%
P_5 / P_3 transport	No	-	-964	2.19%	3.30%
	Yes	No	319	0.40%	-1.24%
		Yes	168	0.26%	-0.80%

In Figure 5.10, the assembly power distributions of VARIANT solutions are compared with the Serpent reference results. Both the diffusion and transport results are obtained with PCDFs and the imbedded correction. It is shown that the diffusion calculation underestimated the fast assembly powers and overestimated the thermal assembly powers, which may be due to the flat leakage approximation used in diffusion PCDFs. Diffusion approximation generally tends to overestimate leakage out of core and the flat leakage approximation enhanced this tendency. It is noted that the reference assembly power distribution showed slight asymmetry because of tally uncertainty. Since VARIANT solutions are symmetric, the error distributions turned to be asymmetric.

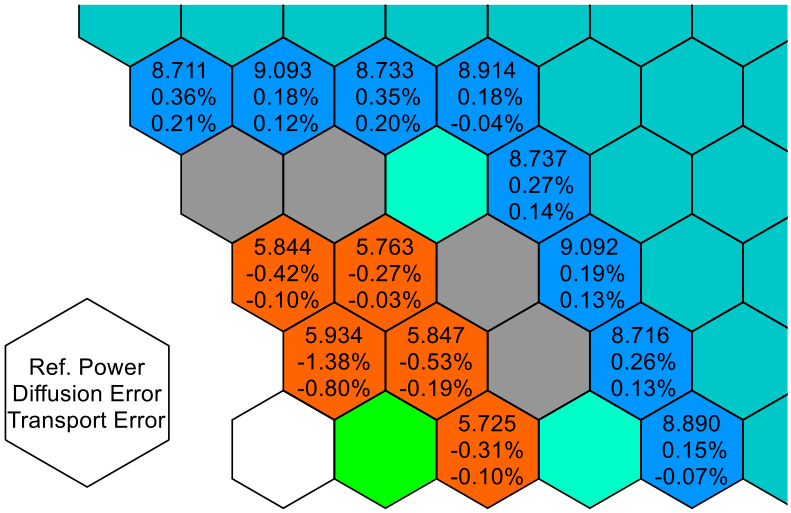

Figure 5.10 Comparison of Assembly Power Distributions in CFTR-2D

5.2 Modified CFTR-2D Problem

The CFTR-2D core does not show strong fast/thermal spectrum interference as the thermal fuel assembly is highly under-moderated. To demonstrate the applicability of the proposed method in a situation with severe spectral transition in fuel assemblies, a modified CFTR-2D core problem (CFTR-2DM) was developed by increasing the local moderator to fuel ratio in the thermal fuel assemblies. The resulting core configuration of CFTR-2DM is shown in Figure 5.11. Compared to the original CFTR-2D core, the only change is in the thermal fuel assemblies. To further simplify the problem for benchmarking purpose, a uniform thermal assembly configuration is used. Each thermal fuel assembly is now composed of 61 U-10Zr (7.0 at.% enriched in U-235) fuel rods and 210 zirconium hydride ($ZrH_{1.6}$) moderator pins. Detailed assembly geometric and compositional specifications are provided in Appendix A.

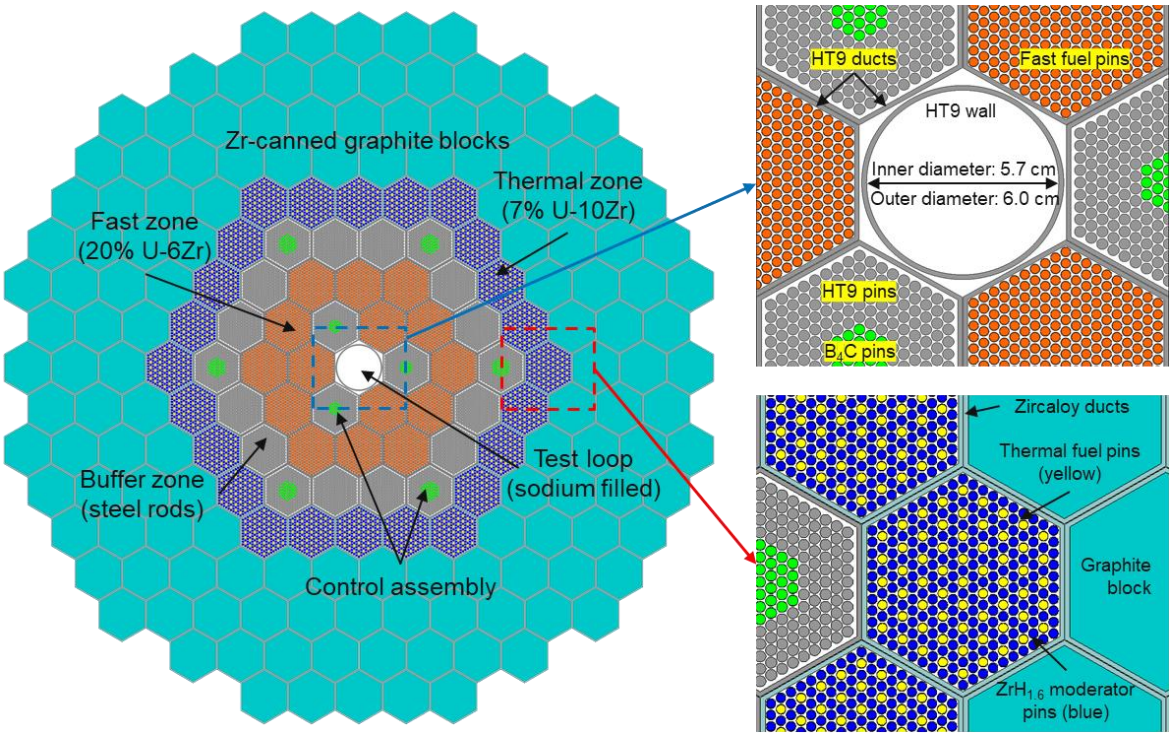

Figure 5.11 CFTR-2DM Core Configuration

With Serpent Monte Carlo simulation, the neutron spectra in different regions of the CFTR-2DM core are compared in Figure 5.12. Now with the enhanced moderation, the thermal assemblies show typical thermal reactor flux spectra. Since the thermal assembly is well moderated, the impact of fast zone on the graphite reflector spectrum is reduced, and only three unique reflector types were defined as shown in Figure 5.13.

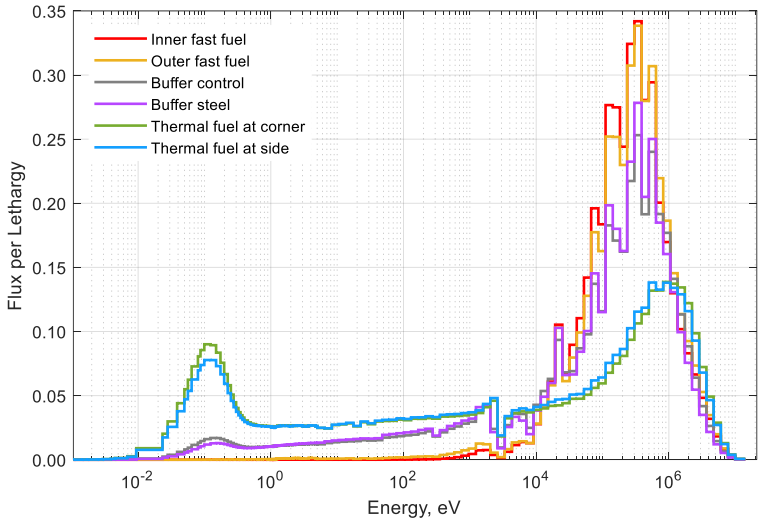

Figure 5.12 Various Neutron Flux Spectra Found in CFTR Core [118]

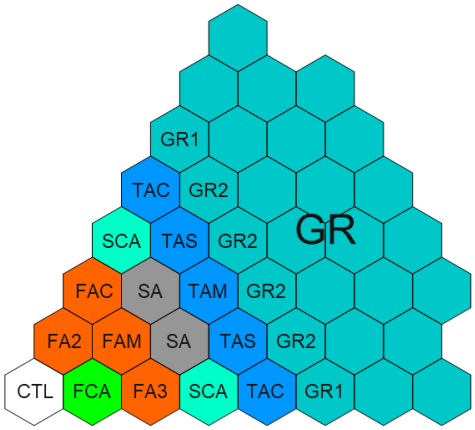

Figure 5.13 Homogenized 1/6 Core Model of CFTR-2DM and Unique Assembly Types

The reference Serpent simulation used 500,000 neutron histories per cycle for a total of 2,000 active cycles. The resulting k-effective was 1.05551±0.00002. The maximum statistical

error in tallied assembly powers is about 0.02%. In a similar procedure, 13G XSs and PCDFs were generated using supercell models and used in subsequent VARIANT calculations. The VARIANT results are summarized in Table 5.3. One can see that the VARIANT calculations without PCDFs resulted in larger assembly power errors compared to the CFTR-2D case, which indicates that the softened spectrum in the thermal assemblies led to larger local heterogeneity effects. With PCDFs, the errors in nodal calculation results were significantly reduced. An interesting observation is that the imbedded PCDF correction caused deterioration of the transport solution. This is probably because the assumption made in Eqs. (4.30) and (4.31) is less applicable to the thermal assembly with increased local heterogeneity.

Table 5.3 VARIANT solutions with supercell XSs and PCDFs for CFTR-2DM problem

Transport order	Use of PCDFs	PCDF correction?	Δk, pcm	Assembly power error	
				rms	max
P_1 / P_0 diffusion	No	-	-304	2.69%	4.26%
	Yes	No	-204	0.90%	1.42%
		Yes	-218	0.28%	0.63%
P_5 / P_3 transport	No	-	373	2.65%	4.31%
	Yes	No	-106	0.12%	-0.26%
		Yes	97	0.27%	0.59%

Alternatively, the supercell fixed source calculation approach for PCDF generation was extensively investigated in a previous study [118]. The sensitivities of PCDF to the heterogeneous model used for fixed source calculation and to the energy resolution of the approximate surface source were discussed. At that time, the performance of the supercell PCDFs was much worse than those tested here. One reason is that previously a finer energy group structure in the thermal energy range was used. Correspondingly, the PCDF is more deviated from one and hence is more sensitive to the boundary conditions of the supercell model used for PCDF generation. Another major difference is in the construction of supercell model. Previous supercell models included only half

of the adjacent assemblies with all reflective boundary conditions. In this work, PCDFs were generated in larger supercell models with non-uniform boundary conditions and background source zone to better represent the core environment.

Because of the deficient performance of supercell PCDFs, the method described in Section 4.2.5.4 was developed to generate PCDF with combined homogenized core and heterogeneous supercell fixed source calculations. Table 5.4 recalls the VARIANT transport solutions obtained with PCDFs generated in supercell eigenvalue and fixed source calculations. Table 5.5 describes how the PCDF sets used to obtain Table 5.4 results were generated. It is seen from Table 5.4 that the PCDFs generated in the supercell fixed source calculation with fine-group incoming partial currents as surface sources produced comparable transport results with the PCDFs from improved supercell models and with imbedded correction in core calculation. In addition, the assembly power distributions predicted by the fixed source (fixsrc) approach and imbedded correction (corre) are compared in Figure 5.14.

Table 5.4 Performance of PCDFs generated in supercell fixed source calculation [118]

Code	PCDF set (fast/buffer/thermal)	k_{eff}	Δk , pcm	Assembly powers errors	
				rms	max
Serpent	-	1.05551 (2*)	Ref.	-	-
VARIANT	PCDF_CEL	1.05345	-206	2.96%	4.70%
	PCDF_SRC	1.05843	292	1.20%	2.22%
	PCDF_SRC_FG	1.05758	207	0.25%	0.64%

* Standard deviation in pcm.

Table 5.5 Description of PCDF sets used to obtain Table 5.4 results

PCDF set	Serpent model	Simulation mode	Boundary condition
PCDF_CEL	Heterogeneous supercell	Eigenvalue	Reflective
PCDF_SRC	Heterogeneous supercell	Fixed source	Broad-group surface source
PCDF_SRC_FG	Heterogeneous supercell	Fixed source	Fine-group surface source

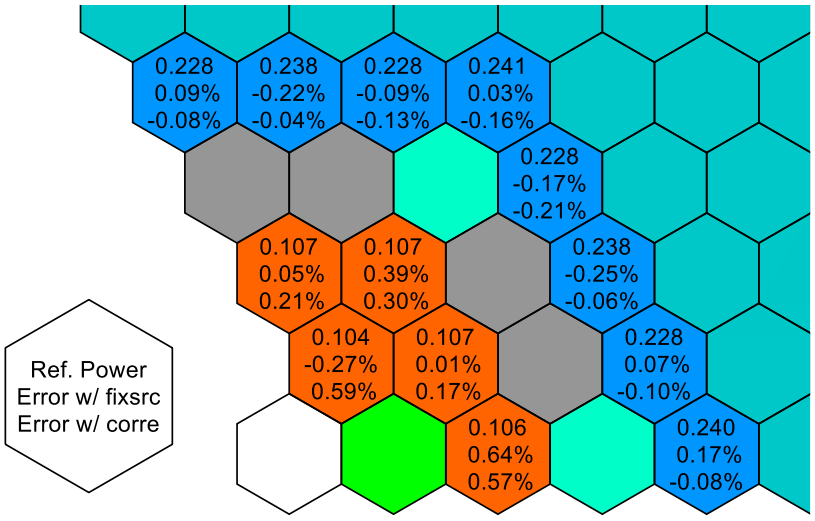

Figure 5.14 Comparison of Assembly Power Distribution in CFTR-2DM

Chapter 6

Whole-Core Depletion Calculation Test

In this chapter, the CFTR-2D problem is used to test the whole-core depletion calculation capability of the improved VARIANT/REBUS-3 codes for coupled fast-thermal spectrum reactors.

6.1 Reference Depletion Calculation

In the reference full-core depletion calculation with Serpent, each fast fuel assembly is treated as a depletion zone to save computational time. In each thermal assembly, each type of fuel pins depending on fuel enrichment are grouped into a depletion zone. The variation of burnup state within each depletion zone is not considered. With this setup, the CFTR-2D core was depleted at a constant fission power level for a 184-day fuel cycle. For each transport calculation, Serpent simulated 100,000 neutron histories per cycle for 2,000 active cycles. The total simulation time is about 3600 CPU hours. The reference depletion history of k-effective and burnups is shown in Figure 6.1. At the end of cycle (EOC), the average fuel burnup is 21 MWD/kgU.

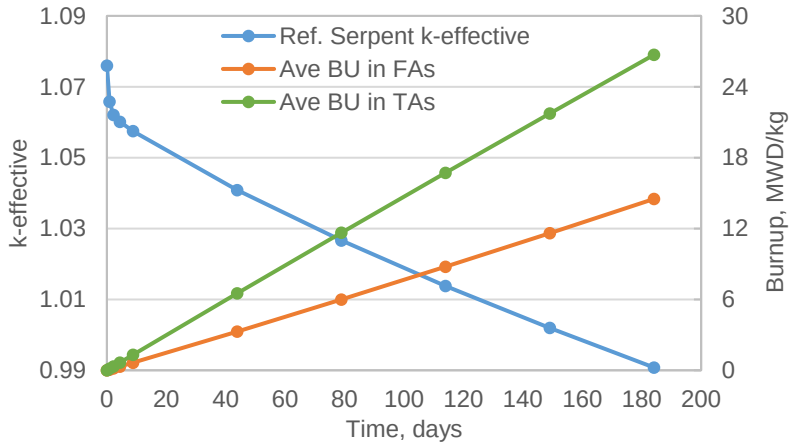

Figure 6.1 History of K-effective and Average Burnups in Fast and Thermal Zones of CFTR-2D

6.2 Generation of Multigroup XSs and PCDFs

From the reference depletion calculation, the burnup dependence of multigroup XSs for nonfuel assemblies were first checked. As shown in Figure 6.2, the macroscopic XSs for the buffer control and reflector assembly are practically constant during fuel depletion. Hence, the homogenized broad-group XSs for nonfuel assemblies generated at the beginning of cycle (BOC) were used for depletion calculations.

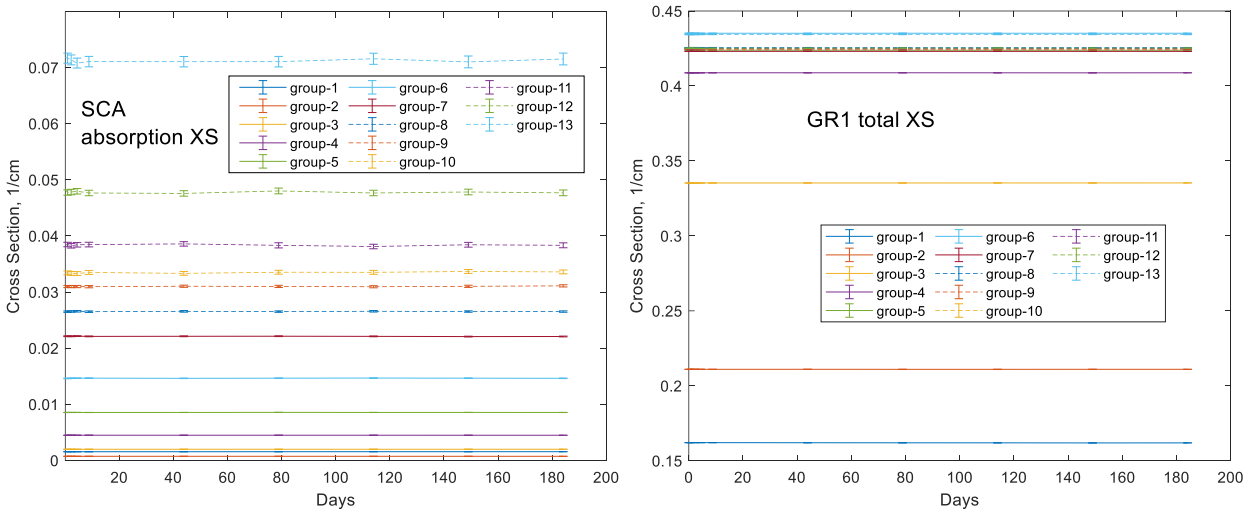

Figure 6.2 Burnup Dependence of Macroscopic XSs for Nonfuel Assemblies

For fuel assemblies, a series of Serpent depletion calculations were performed using the supercell models defined in Chapter 5. At each burnup step, the depleted fuel compositions were fed into the equivalent OpenMC models for isotopic XS generation. The tallied isotopic XSs were tabulated with burnup and written into the VARIXS (Variable Isotopic Cross Sections) dataset. Meanwhile, the nodal average fluxes and surface partial currents tallied at each burnup step with Serpent were used in one-node or multi-node calculations for burnup dependent PCDF generation. To keep consistency, both Serpent and OpenMC simulations were performed with the ENDF/B-VII.1 base library as the official cross section library for OpenMC starts from version VII.1.

The burnup dependent PCDFs for the thermal assembly TAC (see Figure 5.2) are shown in Figure 6.3 for the left and right surfaces and Figure 6.4 for the interface between TAC and TAS. Generally, the variation of PCDFs with burnup is not significant, especially in high-energy groups. The PCDFs at the right surface are more sensitive to burnup than those at the left surface. Especially for the thermal group (group 13), both PCDFs for the incoming and outgoing partial currents through the right surface noticeably decrease with burnup. This is because the 3.0 at.% enriched fuel loaded next to the reflector are depleted faster than the interior high-enriched fuel, which led to a larger change in the local heterogeneity condition. At the interface between TAC and TAS assemblies, all the PCDFs remain almost constant in that the difference in fuel depletion rate among different pin positions were not considered within the same depletion zone.

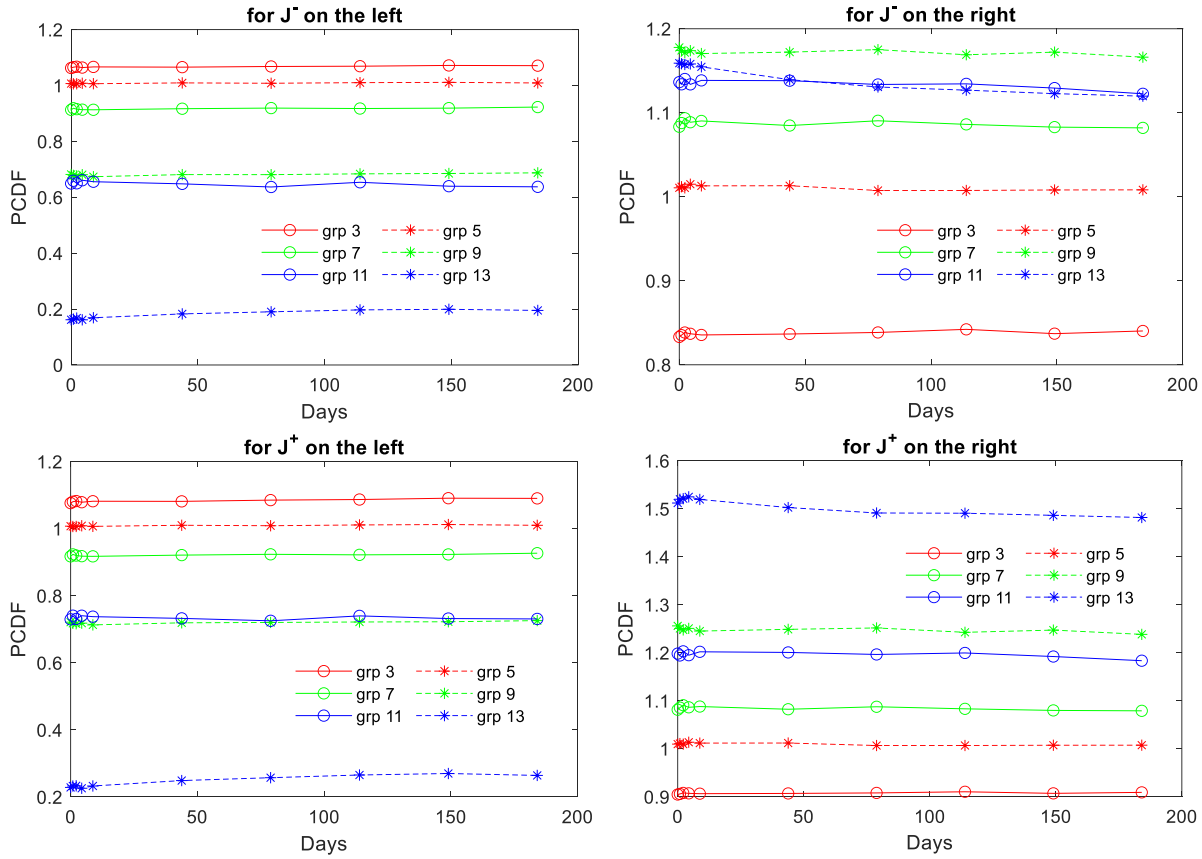

Figure 6.3 Burnup Dependent PCDFs of TAC for Incoming (J^-) and Outgoing (J^+) Partial Currents through Left (Next to SCA) and Right (Next to GR1) Surfaces

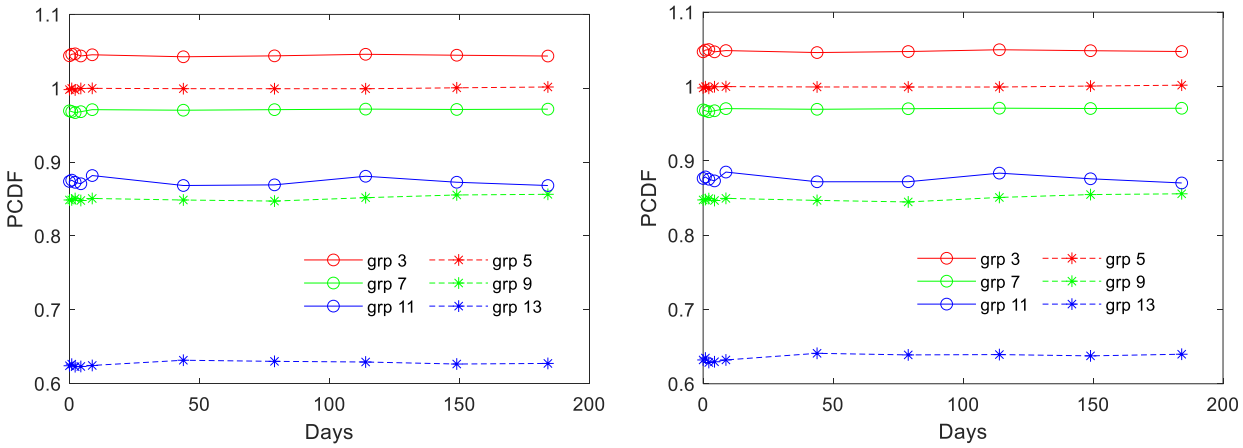

Figure 6.4 Burnup Dependent PCDFs of TAC for Incoming (Left) and Outgoing (Right) Partial Currents through Interface between TAC and TAS

6.3 REBUS-3 Depletion Calculation

For REBUS-3 calculation, a simplified depletion chain including 183 active isotopes as defined in Table 3.13 of Section 3.3.2 was used. According to the steady-state calculation results in Chapter 5, the VARIANT P_5 transport option was used for flux calculation. To make consistent power normalization of reaction rates, the isotopic constant fission Q-values available in the Serpent library were extracted and stored in the VARIXS dataset for REBUS-3 use. In REBUS-3, each fuel assembly is treated as a depletion zone.

We first look at the impact of using different combinations of multigroup cross sections and PCDFs in REBUS-3. Figure 6.5 compares the k-effective results obtained with different options, where "boc DF" means using PCDFs generated at BOC, "burnup" denotes use of burnup dependent PCDFs, and "corrected" denotes the use of imbedded PCDF correction in core calculation. Without use of PCDFs, the REBUS-3 prediction of k-effective evolution largely deviated from the reference solution from the very beginning. This is expected because the homogenization error caused distorted distribution of assembly powers and the error is accumulated through the depletion cycle. It is noted that the use of constant (BOC) PCDFs still

leads to large errors after fuel depletion, although the burnup dependence of PCDFs is not significant as shown in Figure 6.3 and Figure 6.4.

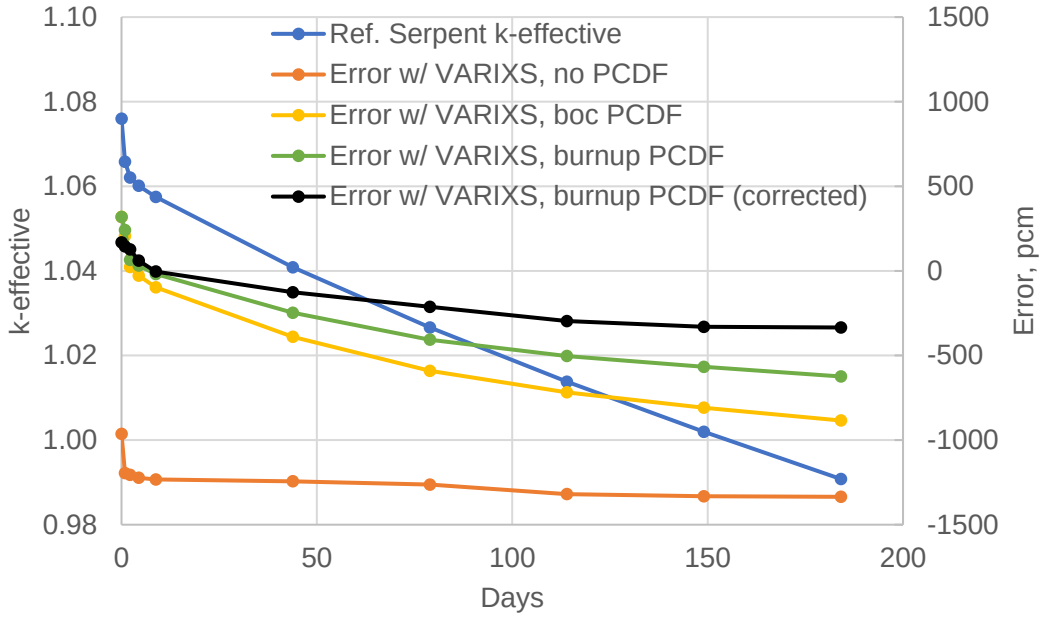

Figure 6.5 Comparison of K-effective Results of REBUS-3 Depletion Calculations

With burnup dependent PCDFs, the eigenvalue error was reduced but not as much as for BOC. The reason is partially in the supercell depletion model for XS and PCDF generation, where the background source zone is not depleted. In the core condition, the global power distribution shift as shown in Figure 6.6 changes the background source distribution for specific supercell. With the imbedded PCDF correction, the REBUS-3 calculation predicted the k-effective history more accurately. Although a non-negligible error remains, the error seems not to drastically increase with depletion.

Figure 6.7 shows the variation of root mean square (rms) and maximum relative errors in fuel assembly powers during the depletion cycle. It is seen that the rms error was slightly increased with the imbedded PCDF correction while the maximum error is considerably reduced. Overall, the assembly powers were predicted rather accurately, with a maximum error less than 1%.

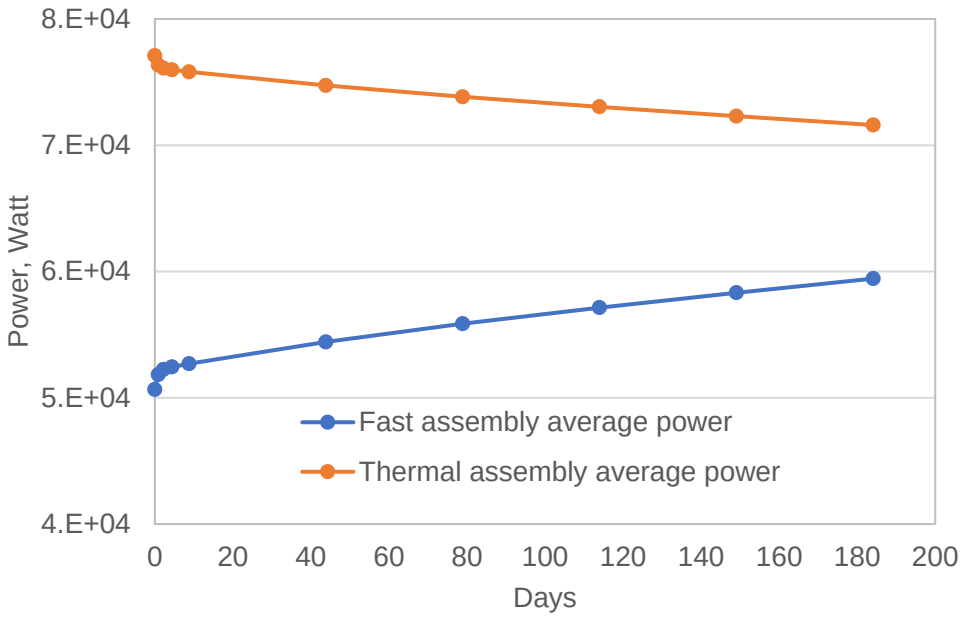

Figure 6.6 Shift of Global Power Distribution

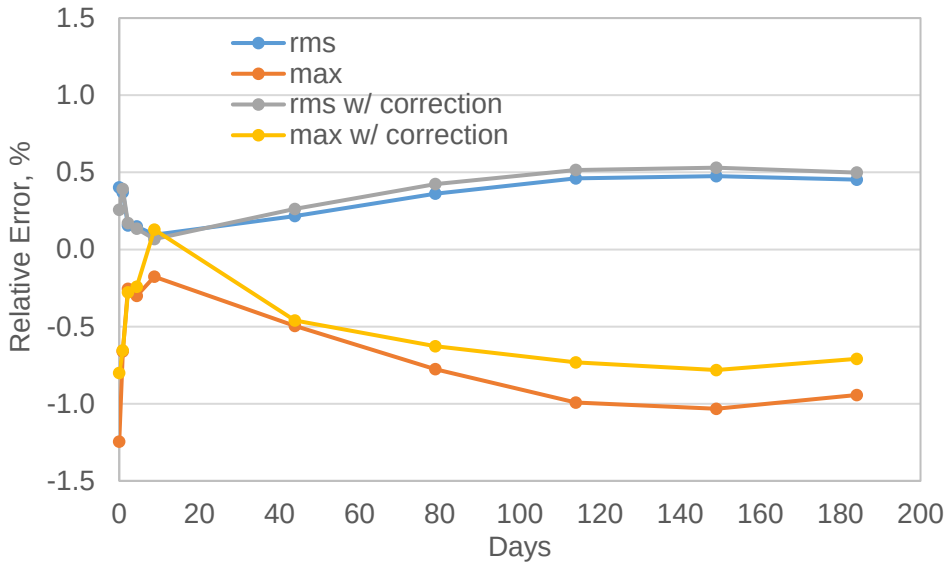

Figure 6.7 Root Mean Square (rms) and Maximum Assembly Power Errors of REBUS-3 Calculations with VARIXS and Burnup Dependent PCDFs

By default, the above calculations were performed with energy dependent fission yields. One more test was conducted to quantify the impact of using constant fission yields determined at the average fission energy (AFE). Figure 6.8 shows the k-effective differences caused by using constant fission yields for all assemblies in the REBUS-3 calculation. Since all the fuel assemblies

in the CFTR-2D core yield hard neutron spectra, the difference in AFE is not large. The AFE is ~ 0.65 MeV in fast assemblies and is ~ 0.35 MeV in thermal assemblies. During the depletion cycle, the change in AFE is negligible.

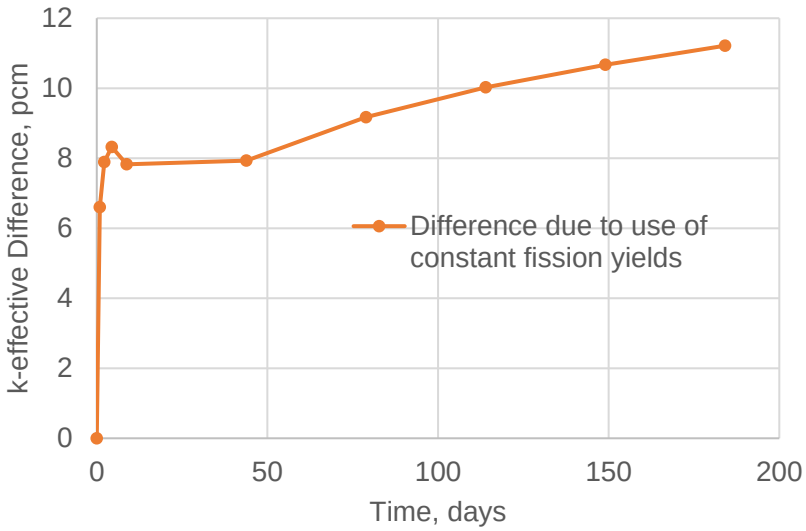

Figure 6.8 K-effective Difference Caused by Using Constant Fission Yields for All Assemblies

Chapter 7

Summary, Conclusions and Future Work

The primary objective of this thesis work is to develop an efficient two-step method for coupled fast-thermal spectrum reactor (CFTR) core analysis. For this purpose, three aspects of the legacy fast reactor analysis method were examined, and several improvements were made to the VARIANT nodal transport and REBUS-3 depletion calculation methods. Eventually, a systematic computational procedure was developed by utilizing Serpent, OpenMC, and MC^2-3 codes for multigroup cross section generation, using VARIANT for nodal core calculation, and using REBUS-3 for depletion analysis. The proposed method was verified using multiple CFTR core problems. Compared to the reference transport and depletion calculation results obtained with Serpent, the proposed methods accurately predicted the eigenvalue and assembly powers in both steady-state transport and fuel depletion calculations.

7.1 MC-based Multigroup Cross Section Generation

Generation of effective multigroup cross section remains the most challenging difficulty in multigroup deterministic neutron transport calculation. For CFTR analysis, the complication is exacerbated because the conventional simplifications adopted in fast or thermal reactor cross section generation methods are not valid anymore. Therefore, a new cross section generation scheme was developed by combining MC simulation and MC^2-3 calculation using assembly supercell models. Supercell models are preferred because of the significant spectral interference in CFTR environments. While rigorous physics are modeled with little approximations in MC

neutron transport and nuclide depletion simulations, the long-range environmental effects must be considered in the supercell model with a reduced problem domain. The conventional leakage correction models such as critical buckling search with homogeneous B_1 calculation or critical albedo search in MC framework cannot catch the complex spectrum interference in CFTRs. To overcome this limitation, it is proposed to apply approximate source boundary conditions or to include background source zones in the supercell model. This method was verified using two CFTR problems.

7.2 Nodal Equivalence Model for VARIANT

To reduce assembly homogenization errors in VARIANT nodal transport calculations for CFTR analyses, a nodal equivalence theory was developed by introducing partial current discontinuity factors (PCDFs). The PCDF is consistently derived for arbitrary angular expansion orders and is fully compatible with the efficient red-black iteration scheme of VARIANT to solve response matrix equations. When used in low-order transport models, PCDF acts as a lumped correction factor to correct homogenization errors as well as the errors due to low-order transport approximations and inaccurate cross sections. It is found that PCDFs generated with increased transport approximation orders tend to converge to asymptotic values, which represent the corrections needed only for nodal homogenization errors. Because of this, it is recommended to apply PCDFs to higher-order transport calculations such that different physics are treated separately and PCDFs are less sensitive to the environment in which they are generated.

Using MC simulation to solve the reference heterogeneous problem, two approaches were developed to generate PCDFs by preserving surface average partial currents in one-node and multi-node VARIANT calculations. Even though only the average partial currents are preserved, PCDFs can be generated in one-node calculations with flat leakage approximation or in multi-node

calculations to reproduce the heterogeneous solution. For practical applications, two strategies were developed to treat long-range environmental effects on the PCDFs generated from supercell models. The first approach performs supercell fixed source calculation with approximate boundary conditions obtained in a homogenized core calculation. The other strategy directly uses the perturbation in the boundary conditions of a homogenized node to estimate the perturbation for the corresponding heterogeneous node. While both strategies showed promising performance in test calculations, the latter is preferred as it leaves out the need of homogenized core calculation.

7.3 REBUS-3 Enhancement for General Depletion Problem

The REBUS-3 code was assessed for non-fast spectrum depletion problems. Test results showed no major deficiencies in the current implementation of REBUS-3. Enhancements of REBUS-3 were made in the depletion chain construction and utilization of burnup dependent cross sections and energy dependent fission yields in a general manner. The modified REBUS-3 with these improvements and the improved VARIANT nodal transport method was verified using a 2D CFTR whole-core depletion problem. Compared to the original REBUS-3 depletion with constant isotopic XSs and VARIANT transport calculation without PCDFs, the new two-step method reduced the k-effective error by ~1000 pcm. It also predicted fuel assembly powers accurately within 1% deviation from the reference MC depletion results

7.4 Discussion of Research Merit

The work presented in this thesis was initiated during the Versatile Test Reactor (VTR) program period. The original VTR design featured a reconfigurable test reactor for which a coupled fast-thermal spectrum core configuration was anticipated. At that time, the focus was to provide reliable tools for daily calculations for coupled-spectrum core design and analysis. At the same time, the Idaho National Laboratory (INL) analyzed the original coupled core design using

finite element methods and SPH factors generated with the full-core MC reference solutions. The proposed core calculation method based on the variational nodal transport method and PCDFs was thought to be more efficient and much cheaper for design calculations. In this sense, a MC based XS and PCDF generation method is more desirable if it does not require full-core simulations.

Now that VTR is not under active development, the interests in coupled-spectrum reactors are receding. But some of the difficulties faced by CFTR core analysis are also encountered in the Very High Temperature Reactor (VHTR) and the Resource Renewable Boiling Water Reactor (RBWR) [129], mainly because of their longer neutron mean free path than LWRs. It is not to say that VHTR or RBWR produces both fast and thermal spectra in the core but rather the enhanced global spectral transition effects make the conventional thermal reactor lattice calculation methods less applicable. For VHTR analysis, a scalar flux discontinuity factor was introduced to VARIANT P_1 calculations [70]. As we showed in Section 4.2.4, the combination of VARIANT transport calculation and PCDFs would eliminate the burden of generating PCDFs for near-homogenized graphite blocks in VHTR. Ref. [54] derived discontinuity factors for high-order P_N calculations in 1D case to treat the significant axial heterogeneity in RBWR. The study performed here seems directly applicable to that situation.

7.5 Future Work

The studies performed in this work have been limited to simple 1D and 2D cases. Although there are no theoretical differences when applying the proposed methods to general three-dimensional (3D) problems, test of the proposed methods in 3D cases appears an immediate need. In the case of pronounced axial heterogeneity as mentioned above for RBWR, 3D Monte Carlo models will be used for XS and PCDF generations. Meanwhile, the possibility of using reduced 2D models for axially homogeneous core will be investigated.

The biggest challenge encountered in this study was to find the way to model long-range environmental effects on PCDFs. The developed fixed source calculation approach turns too cumbersome, especially when burnup dependent PCDFs are to be prepared. The performance of the imbedded PCDF correction strategy is promising but the tested cases are very limited, and hence further investigations are required to validate its applicability to general problems. It is also recommended to reconsider the basic approximation and implementation details. For example, other than to renormalize partial currents with total volumetric source, what would be a better renormalization criterion? More fundamentally, what would be a physical model to consider the boundary perturbation between local and global calculations?

In the depletion calculation test with the CFTR-2D problem, the reference MC simulation was performed without considering pin wise depletion. Investigations are needed to validate supercell models for considering the impact of the local burnup distribution due to global flux gradient on the homogenized XSs and PCDFs. Although not demonstrated in this dissertation, the capability of reconstructing pin power distributions from VARIANT solution was established and verified in Ref. [118]. The current implementation does not support pin power reconstruction in a burned fuel assembly, where the nuclide densities in fuel pins depends on pin positions. The future development will include the treatment of varied nuclide densities in fuel pins due to different burnup states.

At last, PCDFs for higher moments were not generated in this study. Even though the preservation of average flux and surface currents preserves the eigenvalue and power distribution, it is worthwhile to investigate the impacts of high-order discontinuity factors in nodal calculations. The PCDFs for higher-order moments will be generated with an appropriate deterministic method to solve the heterogeneous transport problem.

Appendices

Appendix A

Model Descriptions

A.1 CFTR-1D Model

The heterogeneous configuration of one-dimensional coupled fast-thermal reactor core (CFTR-1D) is shown in Figure A.1. Table A.1 lists geometric design parameters of individual assemblies. Table A.2 gives the nuclides densities of each material used in CFTR-1D.

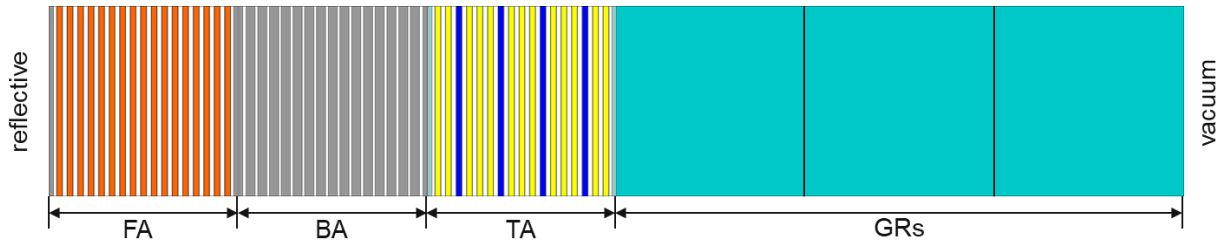

Figure A.1 CFTR-1D Core Configuration

Table A.1 Geometric Design Parameters of CFTR-1D

	FA	BA	TA	GR
Assembly pitch, cm	12.245	12.245	12.245	12.245
Duct material	HT9	HT9	Zr	Zr
Duct thickness, cm	0.28	0.28	0.28	0.28
Outer flat-to-flat, cm	12.205	12.205	12.205	12.205
Number of plates	17	15	12 fuel / 4 mod.	-
Plate thickness, cm	0.408	0.60	0.408	-
Plate pitch, cm	0.68	0.76	0.68	-
Plate / block material	U-6Zr	HT9	U-10Zr / B_4C	graphite
Clad. material	HT9	HT9	Zr	Zr
Clad. thickness, cm	0.0356	-	0.0356	-

Table A.2 Nuclide Densities of CFTR-1D Compositions

Material	Nuclide Densities	Material	Nuclide Densities	Material	Nuclide Densities
HT9	Fe54 4.14754E-03 Fe56 6.51075E-02 Fe57 1.50361E-03 Fe58 2.00104E-04 Ni58 2.97841E-04 Ni60 1.14728E-04 Ni61 4.98757E-06 Ni62 1.58990E-05 Ni64 4.05130E-06 Cr50 4.58427E-04 Cr52 8.84031E-03 Cr53 1.00242E-03 Cr54 2.49524E-04 Mn55 4.67412E-04 Mo92 7.40233E-05 Mo94 4.61399E-05 Mo95 7.94105E-05 Mo96 8.32015E-05 Mo97 4.76363E-05 Mo98 1.20363E-04 Mo100 4.80353E-05	U-6Zr	U234 8.74435E-06 U235 5.81394E-03 U238 2.33175E-02 Zr90 2.48785E-03 Zr91 5.42539E-04 Zr92 8.29282E-04 Zr94 8.40404E-04 Zr96 1.35393E-04	$ZrH_{1.6}$	Zr90 1.89232E-02 Zr91 4.12670E-03 Zr92 6.30775E-03 Zr94 6.39233E-03 Zr96 1.02983E-03 H1 5.88477E-02
		U-10Zr	U234 8.02013e-06 U235 1.87087e-03 U238 2.48478e-02 Zr90 3.97852e-03 Zr91 8.67619e-04 Zr92 1.32617e-03 Zr94 1.34396e-03 Zr96 2.16518e-04	Zr	Zr90 2.20768E-02 Zr91 4.81441E-03 Zr92 7.35891E-03 Zr94 7.45761E-03 Zr96 1.20145E-03
				Sodium	Na23 2.24106E-02
				graphite	C 9.27545E-02

A.2 CFTR-2D Model

The geometric design parameters for various assembly types in CFTR-2D are summarized in Table A.3. The nuclide densities of smeared fuels are given in Table A.4. The other structure, coolant, and moderator materials are same as those given in Table A.2. For the modified CFTR-2D problem, i.e., the CFTR-2DM model, all the setup is same as CFTR-1D except that all fuel pins in thermal assemblies are loaded with 7.0 at.% enriched U-10Zr fuel.

Table A.3 Design Parameters of Different Types of Assemblies in CFTR-2D

	Fast fuel	Thermal fuel		Fast control	Buffer control	Steel reflector	Graphite reflector
		Side	Corner				
Assembly pitch, cm	12.245	12.245	12.245	12.245	12.245	12.245	12.245
Duct material	HT9	Zr	Zr	HT9	HT9	HT9	Zr
Duct thickness, cm	0.3	0.3	0.3	0.3	0.3	0.3	0.3
Outer flat-to-flat, cm	12.205	12.205	12.205	12.205	12.205	12.205	12.205

Table A.3 Design Parameters of Different Types of Assemblies in CFTR-2D (continued)

	Fast fuel	Thermal fuel		Fast control	Buffer control	Steel reflector	Graphite reflector
		Side	Corner				
Number of pins	271	210 fuel 61 mod.	210 fuel 61 mod.	19 B_4C 198 HT9	37 B_4C 180 HT9	217	-
# 19.95 at. % pins	271	147	117	-	-	-	-
# 7.0 at. % pins	-	37	51	-	-	-	-
# 3.0 at. % pins	-	26	42	-	-	-	-
Pin diameter, cm	0.6112	0.6112	0.6112	0.68	0.68	0.68	-
Pin pitch, cm	0.7015	0.7015	0.7015	0.76	0.76	0.76	-
Slug material	U-6Zr	U-10Zr/ $ZrH_{1.6}$	U-10Zr/ $ZrH_{1.6}$	B_4C	B_4C	-	-
Slug density, g/cc	16.3	15.64/5.67	15.64/5.67	2.52	2.52	-	-
Slug smeared density	75%	75%/100%	75%/100%	85%	85%	-	-
Clad. material	HT9	Zr	Zr	HT9	HT9	-	-
Clad. thickness, cm	0.0356	0.0356	0.0356	0.02	0.02	-	-

Table A.4 Fuel Nuclide Densities ($\times 10^{24}/cm^3$) of CFTR-2D

Material	Nuclide Densities	Material	Nuclide Densities
U-6Zr	Zr90 2.48785E-03 Zr91 5.42539E-04 Zr92 8.29282E-04 Zr94 8.40404E-04 Zr96 1.35393E-04 U234 8.74435E-06 U235 5.81394E-03 U238 2.33175E-02	U-10Zr (19.95% enriched)	Zr90 3.97852E-03 Zr91 8.67619E-04 Zr92 1.32617E-03 Zr94 1.34396E-03 Zr96 2.16518E-04 U234 8.03325E-06 U235 5.34115E-03 U238 2.14213E-02
U-10Zr (7.0% enriched)	Zr90 3.97852E-03 Zr91 8.67619E-04 Zr92 1.32617E-03 Zr94 1.34396E-03 Zr96 2.16518E-04 U234 8.02013E-06 U235 1.87087E-03 U238 2.48478E-02	U-10Zr (3.0% enriched)	Zr90 3.97852E-03 Zr91 8.67619E-04 Zr92 1.32617E-03 Zr94 1.34396E-03 Zr96 2.16518E-04 U234 8.01608E-06 U235 8.01397E-04 U238 2.59038E-02

Appendix B

Group Structures

Two broad-group and two fine-group structures were used in this study. The common lower energy boundary is 10^{-5} eV. The 32-group (32G) structure is based on the built-in ANL33 group structure of MC^2-3 but contains single thermal group below 0.6 eV. The 13-group (13G) structure is derived from the ANL9 group structure of MC^2-3 by dividing the last two groups into finer ones. Table B.1 shows the group boundaries of these two group structures.

Table B.1 Broad-group structures for nodal core calculations

	Group	Upper Energy, eV	Group	Upper Energy, eV	Group	Upper Energy, eV
32G	1	1.41907E+07	12	6.73794E+04	23	2.75364E+02
	2	1.00000E+07	13	4.08677E+04	24	1.67017E+02
	3	6.06531E+06	14	2.47875E+04	25	1.01301E+02
	4	3.67879E+06	15	1.50344E+04	26	6.14421E+01
	5	2.23130E+06	16	9.11881E+03	27	3.72665E+01
	6	1.35335E+06	17	5.53084E+03	28	2.26033E+01
	7	8.20850E+05	18	3.35462E+03	29	1.37096E+01
	8	4.97871E+05	19	2.03468E+03	30	8.31528E+00
	9	3.01974E+05	20	1.23410E+03	31	5.00162E+00
	10	1.83156E+05	21	7.48518E+02	32	6.24249E-01
	11	1.11090E+05	22	4.53999E+02	$E_{\min}$	1.00000E-05
13G	1	1.41907E+07	6	9.11881E+03	11	5.00162E+00
	2	2.23130E+06	7	2.03468E+03	12	1.85897E+00
	3	8.20850E+05	8	4.53999E+02	13	6.24249E-01
	4	1.83156E+05	9	1.01301E+02	$E_{\min}$	1.00000E-05
	5	4.08677E+04	10	1.76034E+01		

In addition to the broad-group structures, a finer 86-group (86G) structure as shown in Table B.2 is deduced by combining the ANL70 structure of MC^2-3 for fast reactor calculations

and SCALE 56-group structure for thermal spectrum calculations. The 86G structure is used in fine-group supercell lattice calculations for leakage correction. The last one is a 989-group structure for ultrafine-group calculations. It contains 892 groups above 5.0 eV of the MC^2-3 1041-group structure and 97 groups below 5.0 eV of the SCALE 252-group structure.

Table B.2 86G structure for fine-group lattice calculations

Group	Upper Energy, eV	Group	Upper Energy, eV	Group	Upper Energy, eV
1	1.41907E+07	30	9.11881E+03	59	6.47595E+00
2	1.00000E+07	31	7.10174E+03	60	5.04347E+00
3	7.78801E+06	32	5.53084E+03	61	5.00162E+00
4	6.06531E+06	33	4.30742E+03	62	4.69961E+00
5	4.72367E+06	34	3.35462E+03	63	3.72759E+00
6	3.67879E+06	35	2.61258E+03	64	2.46927E+00
7	2.86505E+06	36	2.03468E+03	65	1.85897E+00
8	2.23130E+06	37	1.58461E+03	66	1.44844E+00
9	1.73774E+06	38	1.23410E+03	67	1.24885E+00
10	1.35335E+06	39	9.61116E+02	68	1.17448E+00
11	1.05399E+06	40	7.48518E+02	69	1.12936E+00
12	8.20850E+05	41	5.82946E+02	70	1.07909E+00
13	6.39279E+05	42	4.53999E+02	71	1.00925E+00
14	4.97871E+05	43	3.53575E+02	72	9.69727E-01
15	3.87742E+05	44	2.75364E+02	73	9.22891E-01
16	3.01974E+05	45	2.14454E+02	74	7.48574E-01
17	2.35177E+05	46	1.67017E+02	75	6.24249E-01
18	1.83156E+05	47	1.30073E+02	76	4.98484E-01
19	1.42642E+05	48	1.01301E+02	77	3.49410E-01
20	1.11090E+05	49	7.88932E+01	78	2.74993E-01
21	8.65169E+04	50	6.14421E+01	79	1.98234E-01
22	6.73794E+04	51	4.78512E+01	80	1.49705E-01
23	5.24751E+04	52	3.72665E+01	81	9.94222E-02
24	4.08677E+04	53	2.90232E+01	82	7.96875E-02
25	3.18278E+04	54	2.26033E+01	83	5.62500E-02
26	2.47875E+04	55	1.76034E+01	84	3.87113E-02
27	1.93045E+04	56	1.37096E+01	85	2.78568E-02
28	1.50344E+04	57	1.06770E+01	86	9.37500E-03
29	1.17088E+04	58	8.31528E+00	$E_{\min}$	1.00000E-05

Appendix C
Description of VARIXS Dataset

The VARIXS dataset contains three file header records that specifies the interface information and general data structure, and a series of nested data records of isotopic cross sections. The general data structure of VARIXS is depicted in Table C.1. The file header records (0D ~ 2D) contain the necessary information for file I/O such as energy group structure, list of isotope names, and involved state parameters. These parameters are used only for interface purpose such that the stored cross section data can be correctly interpreted in core calculation. The isotope header records specify the cross section dependencies and interpolation rules with state parameters.

Table C.1 General data structure of VARIXS

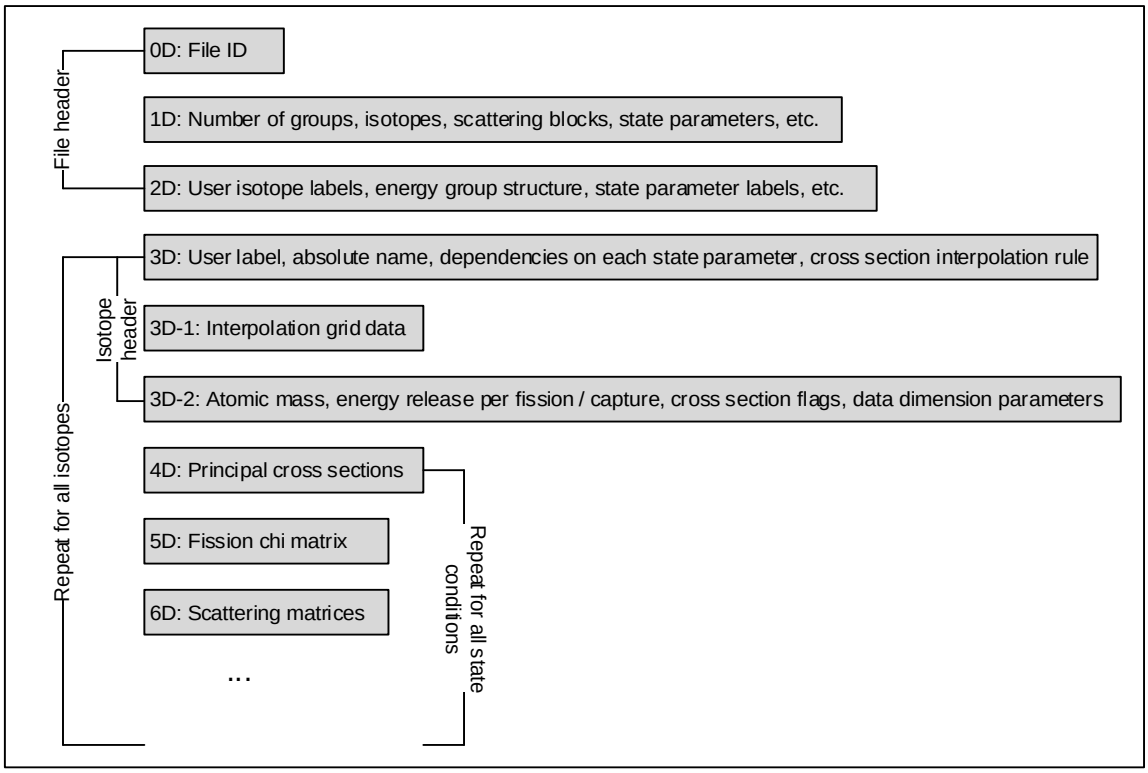

The 4D to 6D records contain the cross sections of an isotope at single state condition. The nesting structure is determined by the dependencies on individual state parameters and the grid points where the cross sections are generated. In total, the nested records form a multi-dimensional table to be interpolated for the cross section at given state condition. Even if the microscopic cross sections of all nuclides in a composition are generated at the same group of state conditions, the same cross section interpolation rule and grid information (3D and 3D-1) are stored for every nuclide such that VARIXS can be conveniently split or merged.

A utility code GenVARIXS was developed to post-process a series of OpenMC tally outputs or a series of ISOTXS datasets that are generated at a wide range of state conditions and to write the state dependent cross sections in the VARIXS format.

Bibliography

1. R. Avery, "Coupled Fast-Thermal Power Breeder," *Nucl. Sci. Eng.*, **3**, 129-144 (1958).
2. R. Avery, "Theory of coupled reactors," *Proceedings of Second United Nations International Conference on the Peaceful Uses of Atomic Energy*, 1958.
3. B.J. Toppel, "The Coupled Aspect of a Fast-Thermal Critical: ZPR-V," ANL-5775, Argonne National Laboratory, 1957.
4. H. Meister, et al., "The Karlsruhe Fast-Thermal Argonaut Reactor Concept," KFK-217, Kernforschungs-zentrum Karlsruhe, 1964.
5. M. Bustraan, et al., "STEK, the Fast-Thermal Coupled Facility of RCN at Petten," Petten Report, RCN-122, Reactor Centrum Nederland, 1970.
6. M. Pesic, "A study on criticality of coupled fast-thermal core HERBE at RB reactor," *Ann. Nucl. Energy*, **18** (7), 413–420 (1991).
7. G. Newman, et al., "GCFR-PROTEUS Experimental Program Core 11: Homogeneous MOX Fuel Test Region," *International Handbook of Evaluated Reactor Physics Benchmark Experiments*, PROTEUS-GCFR-EXP-00, 2006.
8. O.F. Kukharchuk, et al., "Coupled fast-thermal system: theory and experiments," *Proc. PHYSOR 2000 Conf.*, Pittsburgh, Pennsylvania, USA, May 7-12, 2000.
9. P. Ros, et al., "Fast-thermal coupled cores in zero power reactors: A demonstration of feasibility and pertinence for the ZEPHYR project," *Ann. Nucl. Energy*, **110**, 290-305 (2017).
10. G. Palmiotti, M. Salvatores, "Impact of nuclear data uncertainties on innovative fast reactors and required target accuracies," *J. Nucl. Sci. Technol*. **48** (4), 612–619 (2011).
11. G. Youinou, et al., "VCTR: A Versatile Coupled Test Reactor Concept," INL/EXT-16-38852 Rev1, Idaho National Laboratory, May 2016.
12. T. Park, C.S. Lin, and W. S. Yang, "A moderated target design for minor actinide transmutation in sodium-cooled fast reactor," *Ann. Nucl. Energy*, **98**, 178 (2016).
13. P. Deng, et al., "A Hybrid Subcritical Testbed for Fast Neutron Irradiation of Novel Fuels and Claddings in Fast Reactors,"*Trans. Am. Nucl. Soc*., **118**, 869-872 (2018).
14. F.Y. Odeh, et al., "A testing Facility for Advanced Reactor Development and Demonstration," *Trans. Am. Nucl. Soc*., **118**, 717-720 (2018).
15. G. C. Baldwin, "Kinetics of a reactor composed of two loosely coupled cores," *Nucl. Sci. Eng*., **6**, 320-327 (1959). https://doi.org/10.13182/NSE59-A28851.
16. M. Komata, "On the derivation of Avery's coupled reactor kinetics equations," *Nucl. Sci. Eng.*, **38**, 193-204 (1969). https://doi.org/10.13182/NSE69-A21154.
17. B. D. Abramov, "Modifications to the theory of coupled reactors," *At. Energy*, **90** (5), 348-356 (2001).
18. M. Aufiero, et al., "Coupled reactors analysis: New needs and advances using Monte Carlo methodology," *Ann. Nucl. Energy*, **98**, 218-225 (2016).
19. S. Sen, et al., "A Versatile Innovative Coupled Thermal-Fast Test Reactor," *Proc. PHYSOR 2016 Conf.*, Sun Valley, Idaho, 2016.
20. J.J. Duderstadt and L.J. Hamilton, *Nuclear Reactor Analysis*, John Wiley and Sons (1976).

21. R.D. Richtmyer and J. Von Neumann, "Statistical Methods in Neutron Diffusion," Los Alamos (LAMS-551), April 9, 1947.
22. T. Haigh, "Los Alamos Bets on ENIAC: Nuclear Monte Carlo Simulations, 1947–1948," *IEEE Annals of the History of Computing*, **36**, 42-63 (2014).
23. A.K. Prinja and E.W. Larsen, "General Principles of Neutron Transport," In: D.G. Cacuci, *Handbook of Nuclear Engineering*., pp. 430–540. Springer Science+Business Media LLC 2010.
24. S.A. Turner and E.W. Larsen, "Automatic variance reduction for 3-D Monte Carlo simulations by the local importance function transform – Part I: Analysis," *Nucl. Sci. Eng*., **127**, 22 (1997).
25. H.P. Smith and J.C. Wagner, "A case study in manual and automated Monte Carlo variance reduction with a deep penetration reactor shielding problem," *Nucl. Sci. Eng.*, **149**, 23 (2005).
26. J.C. Wagner, E.D. Blakeman, and D.E. Peplow, "Forward-weighted CADIS method for global variance reduction," *Trans. Am. Nucl. Soc*., **97**, 630 (2007).
27. J. Leppänen and M. Jokipii, "Global Variance Reduction Scheme with Self-Adaptive Weight-Window Mesh in the Serpent 2 Monte Carlo Code," *Proc. M&C 2019 Conf.*, Portland, OR, Aug. 25-29, 2019.
28. T. Goorley, et al., "Initial MCNP6 Release Overview," *Nuclear Technology*, **180**, 298-315 (2012).
29. J. Leppänen, et al., "The Serpent Monte Carlo code: Status, development and applications in 2013," *Ann. Nucl. Energy*, **82**, 142-150 (2015).
30. P.K. Romano, et al., "OpenMC: A state-of-the-art Monte Carlo code for research and development," *Ann. Nucl. Energy*, **82**, 90-97 (2015).
31. H.J. Shim, et al., "McCARD: Monte Carlo code for advanced reactor design and analysis," *Nucl. Eng. Technol.*, **44**, 161 (2012).
32. D.P.Griesheimer, et al., "MC21 v.6.0 – A continuous-energy Monte Carlo particle transport code with integrated reactor feedback capabilities," *Ann. Nucl. Energy*, **82**, 29-40 (2015).
33. V. Sanchez, A. Al-Hamry, "Development of a coupling scheme between MCNP and COBRA-TF for the prediction of the pin power of a PWR fuel assembly," *Proc. M&C 2009 Conf.*, Saratoga Springs, New York, USA, 2009.
34. B. Sjenitzer, et al., "Coupling of dynamic Monte Carlo with thermal-hydraulic feedback," *Ann. Nucl. Energy*, **76**, 27–39 (2015).
35. A. Novak, et al., "Preliminary Coupling of OpenMC and Nek5000 Within the MOOSE Framework," *Proc. PHYSOR 2018 Conf.*, Cancun, Mexico, Apr. 22-26, 2018.
36. E.E. Lewis and W.F. Miller, Jr., *Computational Methods of Neutron Transport*, American Nuclear Society, Inc., 1993.
37. D. Knott and A. Yamamoto, "Lattice Physics Computations," In: D.G. Cacuci, *Handbook of Nuclear Engineering*., pp. 914-1232. Springer Science+Business Media LLC, 2010.
38. W.S. Yang, "Fast Reactor Physics and Computational Methods," *Nucl. Eng. Technol.*, **44**, 177-198 (2012).
39. B.A. Lindley, et al., "Current status of the reactor physics code WIMS and recent developments," *Ann. Nucl. Energy*, **102**, 148-157 (2017).
40. J. Rhodes, K. Smith, and D. Lee, "CASMO-5 Development and Applications," *Proc. PHYSOR 2006 Conf.*, Vancouver, BC, Canada, Sept. 10-14, 2006.
41. G. Marleau, A. Hébert, and R. Roy, "A user Guide for DRAGON Version4," Report IGE-294, Institut de génie nucléaire, École Polytechnique de Montréal, December 10, 2013.

42. C.A. Wemple, et al., "Recent Advances in the HELIOS-2 Lattice Physics Code," *Proc. PHYSOR 2008 Conf.*, Interlaken, Interlaken, Switzerland, Sept. 14-19, 2008
43. C.R. Weisbin, et al., "MINX: A Multigroup Interpretation of Nuclear X-Sections from ENDF/B," LA-6486-MS, Los Alamos Scientific Laboratory, 1976.
44. W.J. Davis, M.B. Yarbrough, and A.B. Bortz, "SPHINX, A One-Dimensional Diffusion and Transport Nuclear Cross Section Processing Code," WAPD-XS-3045-17, Westinghouse (1977).
45. B.J. Toppel, H. Henryson II, and C.G. Stenberg, "ETOE-2/MC2-2/SDX Multi-group Cross-Section Processing," Conf-780334-5, Proc. of RSIC Seminar-Workshop on Multi-group Cross Sections, Oak Ridge, TN, March 1978.
46. G. Rimpault, "Algorithmic Features of the ECCO Cell Code for Treating Heterogeneous Fast Reactor Subassemblies," Intl. Conf. on Mathematics and Computations, Reactor Physics, and Environmental Analyses, Portland, Oregon, April 30-May 4, 1990.
47. C.H. Lee, W.S. Yang, "MC^2-3: Multigroup Cross Section Generation Code for Fast Reactor Analysis," *Nucl. Sci. Eng.*,**127**, 341-350 (2017).
48. Y.S. Jung, C.H. Lee, and W.S. Yang, "Verification of Multidimensional Transport Calculation Capability of MC2-3 for Fast Reactor Analysis," *Trans. Am. Nucl. Soc.*, **119**, 1127 (2018).
49. B.K. Jeon, et al., "Extension of MC^2-3 for Generation of Multigroup Cross Sections in Thermal Energy Range," *Proc. M&C 2017*, Jeju, Korea, Apr. 16-20, 2017.
50. K. Koebke, "A new approach to homogenization and group condensation," *Proc. IAEA Technical Committee Mtg. Homogenization Methods in Reactor Physics*, Lugano, Switzerland, Nov. 13-15, 1978.
51. K.S. Smith, "Assembly homogenization techniques for light water reactor analysis," *Prog. Nucl. Energy*, **17**, 303-335 (1986).
52. A. Hebert, "A consistent technique for the pin-by-pin homogenization of a pressurized water reactor assembly," *Nucl. Sci. Eng.*, **113**, 227 (1993).
53. R. Sanchez, "Assembly Homogenization Techniques for Core Calculations," *Prog. Nucl. Energy*, **51**, 14-31 (2009).
54. A.C. Hall, "Homogenization Methods for Full Core Solution of the Pn Transport Equations with 3-D Cross Sections," PhD dissertation, University of Michigan, 2015.
55. A. Yamamoto, T. Endo, and Y. A. Chao, "A derivation of discontinuity factor for angular flux in integral-differential transport equation," *Trans. Am. Nucl. Soc.*, **104**, 815–817 (2011).
56. L. Yu and Y.A. Chao, "A unified generic theory on discontinuity factors in diffusion, SP3 and transport calculations," *Ann. Nucl. Energy*, **75**, 239-248 (2015).
57. A. Yamamoto, "Utilization of Discontinuity Factor in Integrodiffential Type of Boltzmann Transport Equation," *Nucl. Sci. Eng.*, **172**, 259-267 (2012).
58. T. Sakamoto, T. Endo, and A. Yamamoto, "Applicability of angular flux discontinuity factor preserving region-wise leakage for integro-differential transport equation," *J. Nucl. Sci. Technol.*, **51**, 1264-1273 (2014).
59. G. Giudicelli, K. Smith, and B. Forget, "Generalized equivalence methods for 3D multi-group neutron transport," *Ann. Nucl. Energy*, **112**, 9-16 (2018).
60. R.D. Lawrence, "Progress in Nodal Methods for the Solution of the Neutron Diffusion and Transport Equations," *Prog. Nucl. Energy*, **17** (3), 271-301 (1986).
61. Y.S. Liu, et al., "ANC-A Westinghouse Advanced Nodal Computer Code," WCAP-10966, Westinghouse Electric Corp., 1985.

62. T. J. Downar, et al., "PARCS: Purdue Advanced Reactor Simulator," *Proc. PHYSOR 2002 Conf.*, Seoul, Korea, October 7-10, 2002.
63. T. Bahadir, S. Lindahl, and S.P. Palmtag, "SIMULATE-4 Multigroup Nodal Code with Microscopic Depletion Model," *Proc. M&C 2005 Conf.*, Avignon, France, Sept. 12-15, 2005.
64. Y. Bilodid, et al., "Hybrid microscopic depletion model in nodal code DYN3D," *Ann. Nucl. Energy*, **92**, 397-406 (2016).
65. R.D. Lawrence, "The DIF3D Nodal Neutronics Option for Two- and Three-Dimensional Diffusion Theory Calculations in Hexagonal Geometry," ANL-83-1, Argonne National Laboratory, 1983.
66. G. Palmiotti, E.E. Lewis, and C.B. Carrico, "VARIANT: VARIational Anisotropic Nodal Transport for Multidimensional Cartesian and Hexagonal Geometry Calculation," ANL-95/40, Argonne National Laboratory, 1995.
67. M.A. Smith, E.E. Lewis, and E.R. Shemon, "DIF3D-VARIANT 11.0: A Decade of Updates," ANL/NE-14/1, Argonne National Laboratory, 2014.
68. C.B. Carrico, E.E. Lewis, and G. Palmiotti, "Three Dimensional Variational Nodal Transport Methods for Cartesian, Triangular and Hexagonal Criticality Calculations," *Nucl. Sci. Eng.* **111**, 168-179 (1992).
69. P. Deng, et al., "Coupled Neutron and Gamma Heating Calculation Based on VARIANT Transport Solutions," *Nucl. Sci. Eng.*, **193**, 1310-1338 (2019).
70. C.H. Lee, et al., "Application of Nodal Equivalence Parameters to Prismatic VHTR Core Analysis," *Proceedings of Joint International Topical Meeting on Mathematics & Computation and Supercomputing in Nuclear Applications*, Monterey, California, USA, 2007.
71. Y. Li, et al., "Heterogeneous discontinuity factor treatment in Variational Nodal Method," *Ann. Nucl. Energy*, **96**, 126-136 (2019).
72. B.J. Toppel, "A User's Guide to the REBUS-3 Fuel Cycle Analysis Capability," ANL-83-2, Argonne National Laboratory, 1983.
73. W.S. Yang and M.A. Smith, "Theory Manual for the Fuel Cycle Analysis Code REBUS," ANL/NE-19/21, Argonne National Laboratory, 2020.
74. K.L. Derstine, "DIF3D: A Code to Solve One-, Two-, and Three-Dimensional Finite-Difference Diffusion Theory Problems," ANL-82-64, Argonne National Laboratory, 1984.
75. R.E. Alcouffe, et al., "User's Guide for TWODANT: A Code Package for Two-Dimensional, Diffusion-Accelerated Neutral Particle Transport," LA-10049-M, Los Alamos National Laboratory, 1984.
76. Y.S. Jung, et al., "Practical numerical reactor employing direct whole core neutron transport and subchannel thermal/hydraulic solvers," *Ann. Nucl. Energy*, **62**, 357-374 (2013).
77. B. Kochunas, et al., "MPACT: Michigan Parallel Advanced Characteristics Transport," *Proc. M&C 2013 Conf.*, Sun Valley, ID, 2013.
78. E.R. Shemon, M.A. Smith, and C.H. Lee, "PROTEUS-SN Methodology Manual," ANL/NE-14/5, Argonne National Laboratory, June 30, 2014.
79. A. Marin-Laflech, M.A. Smith, and C.H. Lee, "PROTEUS-MOC: A 3-D Deterministic Solver Incorporating 2-D Method OF Characteristics," *Proc. M&C 2013 Conf.*, Sun Valley, ID, May 5-9, 2013.
80. C.H. Lee and Y.S. Jung, "Generation of the Cross Section Library for PROTEUS," ANL/NE-18/2, Argonne National Laboratory, January 2018.

81. S.J. Chucas and M.J. Grimstone, "The accelerated techniques used in the Monte Carlo code MCBEND," *Proceedings of the eighth international conference on radiation shielding*, Arlington, April 24-28, 1994.
82. H.P. Smith and J.C. Wagner, "A case study in manual and automated Monte Carlo variance reduction with a deep penetration reactor shielding problem," *Nucl. Sci. Eng.*, **149**, 23-37 (2005).
83. J. Leppänen, "Response Matrix Method–Based Importance Solver and Variance Reduction Scheme in the Serpent 2 Monte Carlo Code," *Nucl. Technol.*, **205**, 1416-1432 (2019).
84. M.J. Lee, et al., "Multigroup Monte Carlo Reactor Calculation with Coarse Mesh Finite Difference Formulation for Real Variance Reduction," *Proc. 2010 Joint International Conference on Supercomputing in Nuclear Applications and Monte Carlo*, Tokyo, Japan, October 17-21, 2010.
85. I. Kim and Y. Kim, "Whole Core Transport Analysis with the DTMC Method in a Small Modular Reactor," *Trans. Am. Nucl. Soc.*, **119**, 612-615 (2018).
86. E.W. Larsen and J. Yang, "A Functional Monte Carlo Method for k-Eigenvalue Problems," Nucl. Sci. Eng., 159, 107-126 (2008).
87. D. Zhang and F. Rahnema, "An efficient hybrid stochastic/deterministic coarse mesh neutron transport method," *Ann. Nucl. Energy*, **41**, 1-11 (2012).
88. J. Leppänen, M. Pusa, and E. Fridman, "Overview of methodology for spatial homogenization in the Serpent 2 Monte Carlo code,"*Ann. Nucl. Energy*, **96**, 126-136 (2016).
89. H.J. Park, et al., "Generation of Few-Group Diffusion Theory Constants by Monte Carlo Code McCARD," *Nucl. Sci. Eng.*, **172**, 66-77 (2012).
90. W. Boyd, et al., "Multigroup Cross-Section Generation with the OpenMC Monte Carlo Particle Transport Code," *Nucl. Technol.*, **205**, 928-944 (2019).
91. X. Du, et al., "A hybrid method to generate few-group cross sections for fast reactor analysis," *J. Nucl. Sci. Technol.*, **55**, 931-944 (2018).
92. C.S. Lin and W.S. Yang, "An Assessment of the Applicability of Multigroup Cross Sections Generated with Monte Carlo Method for Fast Reactor Analysis," *Nucl. Eng. Technol.*, **52**, 2733-2742 (2020).
93. E. Dorval, "Directional diffusion coefficients and leakage-corrected discontinuity factors: Implementation in Serpent and tests," *Ann. Nucl. Energy*, **87**, 101-112 (2016).
94. Z. Liu, et al., "Cumulative migration method for computing rigorous diffusion coefficients and transport cross sections from Monte Carlo," *Ann. Nucl. Energy*, **112**, 507-516 (2018).
95. D.R. Gaston, et al., "Physics-based multiscale coupling for full core nuclear reactor simulation,"*Ann. Nucl. Energy*, **84**, 45-54 (2015).
96. J. Ortensi, et al., "A Newton solution for the Superhomogenization method: The PJFNK-SPH," *Ann. Nucl. Energy*, **111**, 579-594 (2018).
97. R. Douglas O'Dell, "Standard Interface Files and Procedures for Reactor Physics Code, Version IV," LA-6941-MS, Los Alamos Scientific Laboratory, September 1977.
98. A.E. Isotalo and P.A. Aarnio, "Higher order methods for burnup calculations with Bateman solutions," *Ann. Nucl. Energy*, **38**, 1987-1995 (2011).
99. A.E. Isotalo and P.A. Aarnio, "Substep methods for burnup calculations with Bateman solutions," *Ann. Nucl. Energy*, **38**, 2509–2514 (2011).
100. A. Isotalo and V. Sahlberg, "Comparison of Neutronics-Depletion Coupling Schemes for Burnup calculations," *Nucl. Sci. Eng.*, **179**, 434-459 (2015).

101. C. Moler and C. Van Loan, "Nineteen Dubious Ways to Compute the Exponential of a Matrix, Twenty-Five Years Later," *SIAM Review*, **45**, 3-49 (2003).
102. G.H. Golub and C.F. Van Loan, *Matrix Computations*, Johns Hopkins University Press, Baltimore, Maryland (1989).
103. H. Oh and W.S. Yang, "Comparison of Matrix Exponential Methods for Fuel Burnup Calculations," *Journal of the Korean Nuclear Society*, **31**, 172-181 (1999).
104. A. Yamamoto, M. Tatsumi, and N. Sugimura, "Numerical Solution of Stiff Burnup Equation with Short Half Lived Nuclides by the Krylov Subspace Method," *J. Nucl. Sci. Technol.*, **44**, 147-154 (2007).
105. M. Pusa and J. Leppänen, "Computing the Matrix Exponential in Burnup Calculations," *Nucl. Sci. Eng*., **164**, 140-150 (2010).
106. I.C. Gauld, et al., "Isotopic Depletion and Decay Methods and Analysis Capabilities in SCALE," *Nuclear Technology*, 174, 169-195 (2011).
107. A.E. Isotalo and P.A. Aarnio, "Comparison of depletion algorithms for large systems of nuclides," *Ann. Nucl. Energy*, **38**, 261-268 (2011).
108. J. Cetnar, "General solution of Bateman equations for nuclear transmutations," *Ann. Nucl. Energy*, **33**, 640-645 (2006).
109. A.H. Al-mohy and N.J. Higham, "A New Scaling and Squaring Algorithm for the Matrix Exponential," *SIAM J. Matrix Anal. Appl.*, **31**, 970-989 (2009).
110. R.B. Sidje, "EXPOKIT: Software package for computing matrix exponentials,'' *ACM Trans. Math. Software*, **24**, 130-156 (1998).
111. Wolfram Research, Inc., Mathematica, Version 13.0.0, Champain, IL (2021).
112. E.J. Putzer, "Avoiding the Jordan Canonical Form in the Discussion of Linear Systems with Constant Coefficients," *The American Mathematical Monthly*, **73**, 2-7 (1966).
113. A. Gandini, "Time-dependent Generalized Perturbation Theory for Burn-up Analysis," RT/FI (75) 4, Comitato Nazionale per l'Energia Nucleare, Roma (1975).
114. G. Chiba, et al., "Important fission product nuclides identification method for simplified burnup chain construction," *J. Nucl. Sci. Technol.*, **52**, 953-960 (2015).
115. K.H. N. Nguyen, et al., "Depletion chain optimization of lattice code STREAM for LWR fuel assembly burnup analysis," *Ann. Nucl. Energy*, **123**, 18-45 (2019).
116. Kang Seog Kim, "Specification for the VERA Depletion Benchmark Suite," CASL-U-2015-1014-000, Rev. 0, ORNL/TM-2016/53, 2016.
117. OpenMC website, SFR Spectrum Capture Branching Ratios. https://openmc.org/sfr-spectrum-capture-branching-ratios/
118. P. Deng and W.S. Yang, "A nodal transport method for coupled fast-thermal reactor analysis," *Ann. Nucl. Energy*, **157**, 108229 (2021).
119. Scott P. Palmtag, "Advanced Nodal Methods for MOX Fuel Analysis," PhD Thesis, Massachusetts Institute of Technology, 1997.
120. G. Aliberti, et al., "Methodologies for Treatment of Spectral Effects at Core-Reflector Interfaces in Fast Neutron Systems," *Proc. PHYSOR 2004 Conf.*, Chicago, Illinois, 2004.
121. S. Yun and N.Z. Cho, "Monte Carlo depletion under leakage corrected critical spectrum via albedo search," *Nucl. Sci. Technol.*, **42**, 271 (2010).
122. E. Dorval, "A comparison of Monte Carlo methods for neutron leakage at assembly level," *Ann. Nucl. Energy*, **87**, 591-600 (2016).
123. E.E. Lewis and G. Palmiotti, "Red-Black Response Matrix Acceleration by Transformation of Interface Variables," *Nucl. Sci. Eng.*, **130**, 181-193 (1998).

124. P. Deng, et al., “Implementation of Partial Current Discontinuity Factors in VARIANT Nodal Transport Analysis,” *Trans. Am. Nucl. Soc.*, **123**, 1337-1340 (2020).
125. Kord S. Smith, “Nodal diffusion methods and lattice physics data in LWR analyses: Understanding numerous subtle details,” *Progress in Nuclear Energy*, **101**, 360-369 (2017).
126. Kevin T. Clarno and Marvin L. Adams, “Capturing the Effects of Unlike Neighbors in Single-Assembly Calculations,” *Nucl. Sci. Eng.*, **149**, 182-196 (2005).
127. W. Kim, K. Lee, and Y. Kim, “Functionalization of the Discontinuity Factor in the Albedo-Corrected Parameterized Equivalence Constants (APEC) Method,” *Nucl. Sci. Eng.*, **192**, 1-20 (2018).
128. Hwanyeal Yu, Woosong Kim, and Yonghee Kim, “A leakage correction with SPH factors for two-group constants in GET-based pin-by-pin reactor analyses,” *Ann. Nucl. Energy*, **129**, 30-55 (2019).
129. R. Takeda, J. Miwa, and K. Moriya, “BWRs for long-term energy supply and for fissioning almost all transuranium,” in: *Proceedings of the 2007 Advanced Nuclear Fuel Cycles and Systems (Global) Conference*, 2007.